Author(s): Boguslavski, K.; Kurkela, A.; Lappi, T.; Lindenbauer, F.; Peuron, J.

Title: Jet quenching parameter in QCD kinetic theory

Year: 2024

Version: Published version

Please cite the original version:

Jet quenching parameter in QCD kinetic theory

K. Boguslavski,[1] A. Kurkela,[2] T. Lappi,[3,4] F. Lindenbauer,[1,*] and J. Peuron[3,4,5]

[1]*Institute for Theoretical Physics, TU Wien, Wiedner Hauptstrasse 8-10, 1040 Vienna, Austria*
[2]*Faculty of Science and Technology, University of Stavanger, 4036 Stavanger, Norway*
[3]*Department of Physics, University of Jyväskylä, P.O. Box 35, 40014 University of Jyväskylä, Finland*
[4]*Helsinki Institute of Physics, P.O. Box 64, 00014 University of Helsinki, Finland*
[5]*Department of Astronomy and Theoretical Physics, Lund university, Sölvegatan 14A, S-223 62 Lund, Sweden*

We study the jet quenching parameter $\hat{q}$ in a nonequilibrium plasma using the QCD effective kinetic theory. We discuss subleading terms at large jet momentum p, show that our expression for $\hat{q}$ reproduces thermal results at small and large transverse momentum cutoffs for infinite p, and construct an interpolation between these limits to be used in phenomenological applications. Using simple nonequilibrium distributions that model pertinent features of the bottom-up thermalization scenario, we analytically assess how anisotropy, underoccupation, or overoccupation affect the jet quenching parameter. Our work provides more details on the $\hat{q}$ formula used in our preceding work [Phys. Lett. B **850**, 138525 (2024)] and sets the stage for further numerical studies of jet momentum broadening in the initial stages of heavy-ion collisions from QCD kinetic theory.

I. INTRODUCTION

The goal of relativistic heavy-ion collisions performed at the Relativistic Heavy Ion Collider (RHIC) and the LHC is to achieve a better understanding of the quark-gluon plasma (QGP) that is created in the collisions. In particular, much attention has been directed to the non-equilibrium initial stages of this state of matter. While in general the theoretical description of the early stages requires a solution to nonperturbative nonequilibrium quantum field theory, a description based on weak-coupling methods becomes appropriate in the limit of (asymptotically) high collision energies. In this limit, the initial stages of central heavy-ion collisions follow the bottom-up scenario of [1]. The time evolution of the bottom-up scenario can be described through a set of different effective descriptions that capture the important aspects of the preequilibrium dynamics after the collision. After a so-called glasma phase that can be described using a classical field description [2], the system can be described using quasiparticle degrees of freedom [3–6] within the QCD effective kinetic theory framework [1,7],

in which all leading-order scattering processes are properly taken into account. It smoothly connects to relativistic hydrodynamics [8,9], which is naturally encompassed in kinetic theory [10–12] and is the standard paradigm to describe the later spacetime evolution of the QGP.

The medium modification of jets during the non-equilibrium evolution has recently attracted much attention [13–21]. The jet quenching parameter

$$\hat{q} = \frac{\mathrm{d}\langle q_\perp^2 \rangle}{\mathrm{d}L} \tag{1}$$

is an important quantity that determines the rate of change of transverse momentum of a hard parton traveling through a medium. This parameter $\hat{q}$ is used in many models to quantify medium effects on jet energy loss to compare with experimental data [22–29]. In kinetic theory, the jet quenching parameter is determined by the elastic scattering collision kernel

$$C(\mathbf{q}_\perp) = (2\pi)^2 \frac{\mathrm{d}\Gamma_{\mathrm{el}}}{\mathrm{d}^2 \mathbf{q}_\perp}, \tag{2}$$

where Γ_{el}, the rate of elastic collisions, encodes the probability of the leading jet parton to receive a transverse momentum kick with $\mathbf{q}_\perp$ per unit time [30,31]. It is related to $\hat{q}$ via

$$\hat{q} = \int \frac{\mathrm{d}^2 \mathbf{q}_\perp}{(2\pi)^2} q_\perp^2 C(\mathbf{q}_\perp). \tag{3}$$

The purpose of this paper—and a closely related paper [20]—is to study the jet quenching parameter $\hat{q}$ far from equilibrium within QCD effective kinetic theory.

The jet quenching parameter has been analytically calculated before for a weakly coupled plasma in thermal equilibrium at leading [30,32] and next-to-leading order [31] in weak coupling perturbative QCD (pQCD). At strong couplings using AdS/CFT [33,34], calculations have been performed at leading [35] and next-to-leading order [36] in the inverse coupling. Computations also exist in lattice QCD [37], dimensionally reduced Electrostatic QCD (EQCD) [38], quasiparticle models in thermal equilibrium [39,40], QCD effective kinetic theory with an equilibrium background [41–43]. There are also extractions from experimental data by, e.g., JET [44] and JETSCAPE [45] collaborations. While these calculations have been done assuming (at least local) thermal equilibrium, which is only reached at later stages, recent studies include modifications of the jet evolution due to inhomogeneous, anisotropic, and flowing systems [46–54], and the extraction of the jet quenching parameter $\hat{q}$ during the glasma stage at the earliest times of heavy-ion collisions [14–18]. The impact of preequilibrium dynamics on the related case of heavy-quark diffusion has also sparked interest in the field [17,18,55–60].

In Ref. [20] we have very recently extracted $\hat{q}$ during the anisotropic initial stages of the kinetic bottom-up scenario [1] using QCD effective kinetic theory (EKT) [7,8]. We found that it smoothly connects the large values in the early glasma phase with the smaller values of the hydrodynamical evolution, is consistent with experimentally extracted values of $\hat{q}$ at late times, and leads to anisotropic jet quenching at early times. Our quantitative study of $\hat{q}$ goes beyond the parametric estimates of [1,61–64].

In this paper, we provide the explicit derivation of the leading-order formula for the jet quenching parameter $\hat{q}$ for an on-shell parton that we have used in our EKT simulations [20], and that encodes the anisotropy of the system. Our calculations, however, still neglect the effect of plasma instabilities by employing an isotropic approximation to the medium propagator. It is valid for an arbitrary jet momentum and direction and for anisotropic particle distributions with azimuthal symmetry around the beam axis. Since $\hat{q}$ in the eikonal limit (infinite jet energy) is logarithmically ultraviolet divergent due to its Coulomb logarithm, our results are therefore often functions of an ultraviolet (UV) transverse momentum cutoff $\Lambda_\perp$. We discuss the behavior of our formula of $\hat{q}$ for large jet momentum and large UV cutoff, and explicitly show that it reproduces the known analytic limits for small and large cutoffs in thermal equilibrium. We also assess different (screening) approximations of the matrix elements that are also typically employed in EKT simulations of the time evolution and provide a new approximate form for $\hat{q}$ in thermal gluonic systems that interpolates between the

analytic expressions. We also discuss toy models of bottom-up thermalization [1]. Different stages of this scenario for passage from the initial state towards hydrodynamical evolution are characterized by either over- or underoccupation of gluonic modes, and by an anisotropy of the sytem related to the longitudinal expansion. Thus, to shed light on the effects of the preequilibrium stage on jets, we calculate $\hat{q}$ for an effectively two-dimensional and a scaled thermal distribution, respectively. Although we restrict ourselves to on-shell partons, our formula can also be used as an input for jet evolution models that include an initial large virtuality phase [65,66].

The paper is organized as follows. In Sec. II, we review the parts of the effective kinetic theory description of on-shell (massless) partons that we will need. In Sec. III we arrive at a formula of $\hat{q}$ that is useful for EKT simulations. We then apply it in Sec. IV to a thermal distribution and to toy models for bottom-up thermalization. Finally, we conclude in Sec. V. The Appendices contain details on the $\hat{q}$ formula, its derivation, properties, and evaluation (Appendices A–D) and on the calculation of $\hat{q}$ in toy models (Appendix E).

II. THEORETICAL BACKGROUND AND KINETIC THEORY

We use natural units $c = k_B = \hbar = 1$, the mostly plus metric convention, $\eta_{\mu\nu} = \text{diag}(-1, 1, 1, 1)$, and denote 4-vectors with upper case letters, $Q^\mu = (\omega, \mathbf{q})$, 3-vectors with bold upright symbols, e.g., $\mathbf{q}$, and similarly 2-vectors for transverse momenta $\mathbf{q}_\perp$. A nonbold quantity denotes the length of the corresponding 3-vector, i.e., $q = |\mathbf{q}|$. For the analytic results, we leave the number of colors N_C and the number of quark flavors n_f arbitrary; for the numerical results, we specialize to $N_C = 3$ for QCD and $n_f = 0$, i.e., numerically, we consider a purely gluonic system. For the axis of our coordinate system, we use the letters x, y, and z.

We perform our calculation within the leading-order QCD effective kinetic theory formulated in Ref. [7] that describes the quark-gluon plasma in terms of phase-space densities or quasiparticle distribution functions $f_s(\mathbf{p})$ for the particle species s. In general, $f_s(\mathbf{p})$ depend on time and their time evolution is governed by the Boltzmann equation

$$-\frac{\partial f_s(\mathbf{p})}{\partial \tau} = \mathcal{C}_s^{1 \leftrightarrow 2}[f_s(\mathbf{p})] + \mathcal{C}_s^{2 \leftrightarrow 2}[f_s(\mathbf{p})] + \mathcal{C}^{\text{exp}}[f_s(\mathbf{p})], \quad (4)$$

where $\mathcal{C}^{2 \leftrightarrow 2}$ includes elastic collisions, $\mathcal{C}^{1 \leftrightarrow 2}$ summarizes inelastic interactions, and $\mathcal{C}^{\text{exp}} = -\frac{p_z}{\tau}\frac{\partial f_{\mathbf{p}}}{\partial p_z}$ accounts for the longitudinal expansion of the plasma along the beam direction z [67]. Here, we assume that the medium is homogeneous in the transverse plane and we are interested in the midrapidity region, where we assume boost invariance in the longitudinal direction. Then, our quantities do

not depend on the spatial coordinate $\mathbf{x}$.[1] Additionally, since the particle production is isotropic, and the longitudinal expansion singles out only one preferred direction, the distribution function is independent of the azimuthal angle, and we often write $f(p, \cos\theta_p) := f(\mathbf{p})$, with θ_p the angle between the z axis and $\mathbf{p}$.

To calculate the jet quenching parameter $\hat{q}$, we only need the elastic collision term $\mathcal{C}^{2\leftrightarrow2}$. It consists of a loss term and a gain term and reads

$$
\begin{aligned}
\mathcal{C}_a^{2\leftrightarrow2}[f_s(\mathbf{p})] = \frac{1}{4|\mathbf{p}|\nu_a} \sum_{bcd} \int_{\mathbf{k}\mathbf{p}'\mathbf{k}'} &|\mathcal{M}_{cd}^{ab}(\mathbf{p},\mathbf{k};\mathbf{p}'\mathbf{k}')|^2 \\
&\times (2\pi)^4\delta^4(P+K-P'-K') \\
&\times \{f_a(\mathbf{p})f_b(\mathbf{k})[1\pm f_c(\mathbf{p}')][1\pm f_d(\mathbf{k}')] \\
&- f_c(\mathbf{p}')f_d(\mathbf{k}')[1\pm f_a(\mathbf{p})][1\pm f_b(\mathbf{k})]\}.
\end{aligned} \quad (5)
$$

The number of spin times color states for a given particle species a is denoted by $\nu_a = 2d_a$, where d_a is the dimension of its representation. The external particles in the $2 \leftrightarrow 2$ scattering are ultrarelativistic and on shell, i.e., $P^2 = 0$ or $P^0 = |\mathbf{p}| = p$, and the integral measure is defined as

$$
\int_{\mathbf{k}} := \int \frac{\mathrm{d}^3\mathbf{k}}{(2\pi)^3 2k}. \quad (6)
$$

The matrix elements $|\mathcal{M}_{cd}^{ab}|^2$ correspond to elastic two-particle scattering processes summed over spins and colors of all incoming and outgoing particles. They are calculated in pQCD and can be found in [7]. However, due to medium effects, for soft gluon or fermion exchange these have to be modified by including the hard thermal loop (HTL) self-energy. In practice, one often uses an isotropic screening approximation [8,71–74]. Screening is also important for $\hat{q}$, and we will discuss this approximation and the HTL-screened matrix elements in more detail in Sec. III F.

We will need several observables that can also be computed in a kinetic theory. The energy density ϵ can be calculated by weighing the distribution function for a specific species with its energy,

$$
\epsilon = \sum_s \nu_s \int \frac{\mathrm{d}^3\mathbf{p}}{(2\pi)^3} p f_s(\mathbf{p}). \quad (7)
$$

We will frequently encounter the Debye mass m_D, which is an effective gluonic screening mass given by

$$
m_D^2 = \sum_s 8d_s g^2 \frac{C_s}{d_A} \int_{\mathbf{p}} f_s(\mathbf{p}). \quad (8)
$$

---

[1]However, we note that the EKT approach [7] is more general and allows for spatially inhomogeneous systems [68–70].

In thermal equilibrium with n_f quark flavors these definitions reduce to

$$
\epsilon(T) = \frac{\pi^2 T^4}{60}(4d_A + 7n_\mathrm{f} d_\mathrm{F}), \quad (9a)
$$

$$
m_D^2(T) = \frac{g^2 T^2}{3}\left(N_\mathrm{C} + \frac{n_\mathrm{f}}{2}\right). \quad (9b)
$$

The indices F and A that we used in these expressions denote the fundamental and adjoint representation of fermions and gluons, respectively. In particular, their dimensions are $d_\mathrm{F} = N_\mathrm{C}$ and $d_\mathrm{A} = N_\mathrm{C}^2 - 1$ with the number of colors $N_\mathrm{C} = 3$. Similarly, the quadratic Casimir reads $C_\mathrm{F} = d_\mathrm{A}/(2N_\mathrm{C})$ and $C_\mathrm{A} = N_\mathrm{C}$.

III. KINETIC THEORY FORMULA FOR $\hat{q}$

In this section, we give a derivation of $\hat{q}$ in the quark-gluon plasma with fermionic and gluonic degrees of freedom. Our final formula is given by Eq. (26) with the details described in Sec. III C for a finite jet momentum, and those in Sec. III H for infinite momentum $p \to \infty$. The corresponding matrix elements and their screening prescriptions are discussed in detail in Secs. III E–III H.

The geometry of the problem we consider here is motivated by its application to bottom-up thermalization and illustrated in Fig. 1, but is more generally applicable to any system with azimuthal symmetry in momentum space. We take z to be the anisotropy direction (e.g., the beam axis) and the momentum of the jet to be within the x–z plane. We denote its polar angle θ_p, which is usually set to $\theta_p = \pi/2$ for jet propagation perpendicular to the beam axis. We emphasize that we are not actually following the trajectory of a jet and letting it be deflected by the medium. Rather we
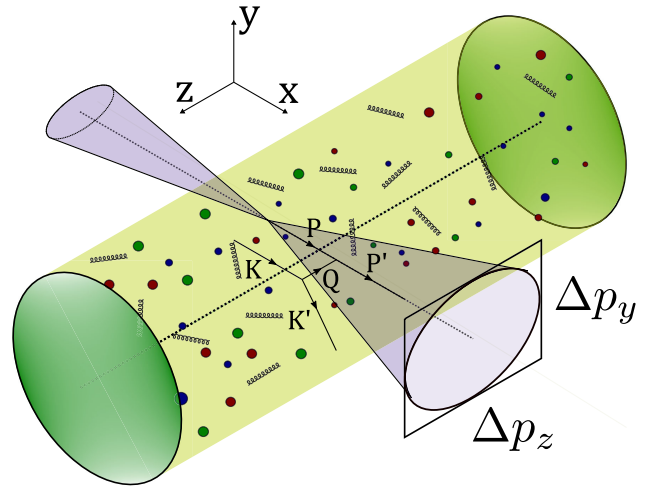

FIG. 1. Geometry of jet quenching. The beam axis is the z direction and the jet parton moves perpendicularly to the y axis in this graphic along the x direction.

measure the momentum transfer rate that such a jet would receive were it allowed to interact, performing the calculation for a jet momentum that is constant in magnitude and angle during the time evolution of the system.

A. Derivation of $\hat{q}(p)$ from the scattering rate

We first consider the leading hard parton of a jet with a large but finite momentum $\mathbf{p}$, which should be much larger than all momentum scales of the plasma such that $f(\mathbf{p}) \approx 0$. We start with the definition (3) and extend it to account for anisotropies

$$\hat{q}^{ij}(p) = \int d^2\mathbf{q}_\perp q_\perp^i q_\perp^j \frac{d\Gamma_{\text{el}}}{d^2 q_\perp}, \qquad (10)$$

where Γ_{el} is the rate of elastic collisions of a highly energetic jet parton with plasma particles and $q_\perp$ is the transferred transverse momentum in such a single collision. For total transverse momentum broadening $\hat{q}$ we need to sum over the directions perpendicular to the jet direction,

$$\hat{q} = \hat{q}^{11} + \hat{q}^{22}. \qquad (11)$$

It measures the average transverse momentum transfer squared to the jet particle per unit time (or length, as we are using units in which $c = 1$). Here, 1 and 2 denote the directions perpendicular to the jet.

We can also think of the elastic scattering rate Γ_{el} as the decay rate of a particle with a fixed momentum $\mathbf{p}$. It can be obtained [75] by identifying it with the loss term in the elastic collision kernel (5) that describes scatterings out of the state $\mathbf{p}$, leading to

$$\Gamma_{\text{el}} = \frac{1}{4p\nu_a} \sum_{bcd} \int_{\mathbf{k p' k'}} (2\pi)^4 \delta^4(P + K - P' - K')$$
$$\times |\mathcal{M}_{cd}^{ab}(\mathbf{p}, \mathbf{k}; \mathbf{p}', \mathbf{k}')|^2 f_b(\mathbf{k})[1 \pm f_d(\mathbf{k}')][1 \pm f_c(\mathbf{p}')]. \qquad (12)$$

This formula is also valid out of equilibrium, provided that the spectral function, which describes the relevant excitations, is very narrow. In particular, the duration of the scattering process should be much smaller than the typical time between collisions. In fact, the same conditions as for QCD kinetic theory [7,76] are required, which we shall briefly summarize here for the reader's benefit: A large separation of scales between the medium-dependent effective screening masses [such as the Debye mass m_D from Eq. (8)] and the momenta of the relevant excitations p_{hard} is required, $p_{\text{hard}} \gg m_D$. Additionally, the effective masses should be large compared to the quark masses and Λ_{QCD}, as well as to the small-angle scattering rate τ_{soft}^{-1}. Although Eq. (12) does not yet specify the concrete form of the matrix element, we assume that no other contributions need to be taken into account. For instance, the presence of

plasma instabilities might lead to additional contributions to the scattering rate, which we neglect. Additionally, the distribution functions $f(\mathbf{p})$ should not vary significantly with $\mathcal{O}(m_D)$ changes in momentum, and they should not be nonperturbatively large for the typical momenta, $f(p_{\text{hard}}) \ll 1/\lambda$.

Equation (12) is symmetric under the exchange of the outgoing particles $\mathbf{p}' \leftrightarrow \mathbf{k}'$ and $c \leftrightarrow d$, but the inclusion of $q_\perp^i q_\perp^j$ as in Eq. (10) breaks this symmetry. We choose to define the harder outgoing particle to be the jet particle and label it c with momentum p', which is also done in previous studies, as, e.g., in [30,31,77] as well. In Ref. [41] this arises naturally if one only considers soft momentum exchange processes. This choice implies that $p' > k'$ is always valid. With this we can rewrite Eq. (12) with a step function $\theta(p' - k')$ and an additional factor of 2 using the identity

$$\int_{\mathbf{k'p'}} g(k', p') = 2 \int_{\mathbf{k'p'}} g(k', p')\theta(p' - k') \qquad (13)$$

for symmetric functions $g(p', k') = g(k', p')$. We note that this leads to more matrix elements than in Ref. [7] because we now treat processes like $qg \leftrightarrow gq$ differently than $qg \leftrightarrow qg$. We will discuss this new complication in more detail and list the required matrix elements explicitly in Sec. III E.

Due to the large jet momentum, we have $f(\mathbf{p}') = 0$, and with $p' > k'$ we obtain

$$\hat{q}^{ij} = \frac{1}{2p\nu_a} \sum_{bcd} \int_{\substack{\mathbf{k p' k'} \\ p' > k'}} q_\perp^i q_\perp^j (2\pi)^4 \delta^4(P + K - P' - K')$$
$$\times |\mathcal{M}_{cd}^{ab}(\mathbf{p}, \mathbf{k}; \mathbf{p}', \mathbf{k}')|^2 f^b(\mathbf{k})[1 \pm f^d(\mathbf{k}')]. \qquad (14)$$

In Appendix A, we show that kinematically one obtains the following restrictions of the integration variables

$$|\omega| < q, \qquad p > \frac{q - \omega}{2}, \qquad k > \frac{q + \omega}{2}, \qquad (15)$$

where $\mathbf{q}$ is the transferred momentum and ω the transferred energy,

$$\mathbf{q} = \mathbf{p}' - \mathbf{p} = \mathbf{k} - \mathbf{k}', \qquad (16a)$$

$$\omega = p' - p = k - k'. \qquad (16b)$$

Using these restrictions from energy-momentum conservation, we will reduce the phase-space integration in Eq. (4) to five integrals in Sec. III C, where we choose $k, q = |\mathbf{q}|, \omega$ and two angles as integration variables. But before that, we describe the coordinate frames necessary for the angular part of the integral in the next section.
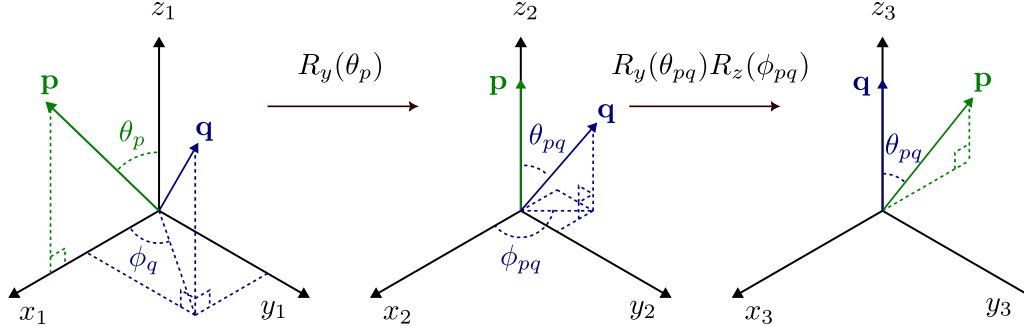
FIG. 2. The integration frames. Left: "lab frame." The jet momentum **p** lies in the x–z plane. Center: "p frame," obtained by rotating the "lab frame" around the y axis, such that **p** points in the z direction. Right: "q-frame." Here, **q** points in the z direction and **p** lies in the x–z plane.

B. Coordinate systems

For the angular integrals, it is convenient to choose specific coordinate systems whose z-axis coincides with either **p** or **q**. This is due to our choice of the integration variables k, q, and ω, which kinematically fixes the angles between **p** and **q**, and between **q** and **k** by energy conservation; see Appendix A. However, since the phase-space density f in our kinetic program is stored in the "lab frame" where z is the beam direction, we need to work out the precise rotations to connect it to the other integration frames. We denote the vectors in this "lab frame" by a lower subscript 1,[2]

$$\mathbf{p}_1 = p(\sin\theta_p, 0, \cos\theta_p), \tag{17a}$$

$$\mathbf{q}_1 = q(\sin\theta_q \cos\phi_q, \sin\theta_q \sin\phi_q, \cos\theta_q), \tag{17b}$$

$$\mathbf{k}_1 = k(\sin\theta_k \cos\phi_k, \sin\theta_k \sin\phi_k, \cos\theta_k). \tag{17c}$$

Because of our azimuthal symmetry around the z axis, we can always rotate this frame such that **p** lies in the x–z plane. For the angular integrals in Eq. (14) we need to choose appropriate coordinate systems, or frames, in which we perform them.[3] Here, the jet momentum defines a distinct direction. Therefore, we define a second frame, denoted by a subscript 2, in which **p** points in the z direction and that is obtained via a rotation of the "lab frame" around the y axis (see Fig. 2). We refer to this frame as "p frame,"

---

[2]Although we do not need the expressions for **p**, **q**, and **k** in this frame and in the following discussions, we list them here for completeness and convenience, since this illustrates the naming convention of the angles, out of which we will only later need ϕ_p, ϕ_{kq}, and ϕ_{pq}.

[3]In typical EKT implementations [8,72–74,78], the **q** integral is evaluated in the "lab frame" and all other integrals in a frame in which **q** points in the z direction. In this case, because of the "wedge" function discretization [71], also an integral over **p** (in our case the jet momentum) is performed. Here, similarly to Ref. [79], we choose to proceed differently.

$$\mathbf{p}_2 = p(0, 0, 1), \tag{18a}$$

$$\mathbf{q}_2 = q(\sin\theta_{pq} \cos\phi_{pq}, \sin\theta_{pq} \sin\phi_{pq}, \cos\theta_{pq}), \tag{18b}$$

$$\mathbf{k}_2 = k(\sin\theta_{pk} \cos\phi_{pk}, \sin\theta_{pk} \sin\phi_{pk}, \cos\theta_{pk}). \tag{18c}$$

In this "p frame" we perform the integral over **q**.

The **k** integral is performed in a third frame, in which **q** points in the z direction and **p** lies in the x–z plane. We call this the "q frame" and denote it by a subscript 3:

$$\mathbf{p}_3 = p(\sin\theta_{pq}, 0, \cos\theta_{pq}), \tag{19a}$$

$$\mathbf{q}_3 = q(0, 0, 1), \tag{19b}$$

$$\mathbf{k}_3 = k(\sin\theta_{kq} \cos\phi_{kq}, \sin\theta_{kq} \sin\phi_{kq}, \cos\theta_{kq}). \tag{19c}$$

The components of the vectors transform between the frames according to the matrix relations

$$\mathbf{v}_2 = A\mathbf{v}_1, \qquad A = R_y(\theta_p), \tag{20a}$$

$$\mathbf{v}_3 = B\mathbf{v}_2, \qquad B = R_y(\theta_{pq})R_z(\phi_{pq}), \tag{20b}$$

where $R_y(\alpha)$ and $R_z(\alpha)$ denote the matrices corresponding to a rotation with angle α around the y- and z-axis, respectively. The transformation matrices read

$$A = \begin{pmatrix} \cos\theta_p & 0 & -\sin\theta_p \\ 0 & 1 & 0 \\ \sin\theta_p & 0 & \cos\theta_p \end{pmatrix}, \tag{21a}$$

$$B = \begin{pmatrix} \cos\theta_{pq}\cos\phi_{pq} & \cos\theta_{pq}\sin\phi_{pq} & -\sin\theta_{pq} \\ -\sin\phi_{pq} & \cos\phi_{pq} & 0 \\ \cos\phi_{pq}\sin\theta_{pq} & \sin\theta_{pq}\sin\phi_{pq} & \cos\theta_{pq} \end{pmatrix}. \tag{21b}$$

For the calculation of $\hat{q}^{ij}$ we use the components $q_\perp^i$ of **q** in the p-frame,

$$q^1 = (\mathbf{q}_2)^1 = q \sin\theta_{pq} \cos\phi_{pq} \qquad (22a)$$

$$q^2 = (\mathbf{q}_2)^2 = q \sin\theta_{pq} \sin\phi_{pq} \qquad (22b)$$

$$q^3 = (\mathbf{q}_2)^3 = q \cos\theta_{pq}. \qquad (22c)$$

In this way the components of $\hat{q}$ are defined relative to $\mathbf{p}$. Thus the components 1 and 2 are perpendicular to $\mathbf{p}$ and quantify the momentum broadening transverse to the jet.

Having taken the Dirac delta functions in Eq. (14) into account, we choose ϕ_{pq}, ϕ_{kq}, k, ω, and q as independent integration variables. Therefore, we need to express all other quantities in terms of them. The value of $\cos\theta_{pq}$, for example, is actually set by kinematic constraints (or the delta function in Appendix A), as can be seen easily via $|\mathbf{k}'|^2 = |\mathbf{k} - \mathbf{q}|^2 = (k - \omega)^2$. Similarly, together with $|\mathbf{k}' + \mathbf{q}|^2 = (k' + \omega)^2$, we find

$$\cos\theta_{kq} = \frac{\omega}{q} - \frac{\omega^2 - q^2}{2kq}, \qquad (23a)$$

$$\cos\theta_{pq} = \frac{\omega}{q} + \frac{\omega^2 - q^2}{2pq}, \qquad (23b)$$

$$\cos\theta_{k'q} = \frac{\omega}{q} + \frac{\omega^2 - q^2}{2k'q}. \qquad (23c)$$

The distribution functions $f(\mathbf{k})$ and $f(\mathbf{k}')$ in (14) are numerically stored in the "lab-frame." Thus we need a way to express their polar angles θ_k and $\theta_{k'}$ in terms of the integration variables. The azimuthal angles ϕ_k and $\phi_{k'}$ are not needed due to azimuthal symmetry. Because we perform the $\mathbf{k}$-integral in the "q-frame" and need $\cos\theta_k$ in the "lab-frame," we need to work out their relation via (20a) and (20b), thus $\mathbf{k}_1 = A^T B^T \mathbf{k}_3$. From $(\mathbf{k}_1)_z$ we can read off

$$\cos\theta_k = \sin\phi_{kq} \sin\phi_{pq} \sin\theta_{kq} \sin\theta_p - \cos\phi_{kq} \sin\theta_{kq}$$
$$\times (\cos\phi_{pq} \cos\theta_{pq} \sin\theta_p + \cos\theta_p \sin\theta_{pq})$$
$$+ \cos\theta_{kq} (\cos\theta_p \cos\theta_{pq} - \cos\phi_{pq} \sin\theta_p \sin\theta_{pq}), \qquad (24)$$

and a similar expression holds for $\cos\theta_{k'}$,

$$\cos\theta_{k'} = \sin\phi_{kq} \sin\phi_{pq} \sin\theta_{k'q} \sin\theta_p - \cos\phi_{kq} \sin\theta_{k'q}$$
$$\times (\cos\phi_{pq} \cos\theta_{pq} \sin\theta_p + \cos\theta_p \sin\theta_{pq})$$
$$+ \cos\theta_{k'q} (\cos\theta_p \cos\theta_{pq} - \cos\phi_{pq} \sin\theta_p \sin\theta_{pq}). \qquad (25)$$

The azimuthal angle is $\phi_{k'q} = \phi_{kq}$ because $\mathbf{k}' = \mathbf{k} - \mathbf{q}$ and $\mathbf{q}$ points in the z direction in the "q-frame."

C. Formula for $\hat{q}(p)$

We are now ready to give the formula for the components of $\hat{q}$:

$$\hat{q}^{ij} = \frac{1}{2^9 \pi^5 \nu_a} \sum_{bcd} \int d\Gamma q^i q^j \frac{|\mathcal{M}^{ab}_{cd}|^2}{p^2} f_b(k, v_k)(1 \pm f_d(k', v_{k'})), \qquad (26)$$

where we use the abbreviation of $v_{...} = \cos\theta_{...}$. The phase-space integration measure can be written as a product of two angular integrals and three additional integrals that are different depending on the order of integration and integration variables,

$$\int d\Gamma = \int_0^{2\pi} d\phi_{pq} \int_0^{2\pi} d\phi_{kq} \int d\Gamma_3, \qquad (27)$$

with the three equivalent versions (Appendix A)

$$\int d\Gamma_3 = \int_0^\infty dk \int_{-\frac{p-k}{2}}^k d\omega \int_{|\omega|}^{\min(2p+\omega, 2k-\omega)} dq, \qquad (28a)$$

$$\int d\Gamma_3 = \int_0^\infty dk \int_0^{\frac{k+p}{2}} dk' \int_{|k-k'|}^{\min(p+p', k+k')} dq, \qquad (28b)$$

$$\int d\Gamma_3 = \int_0^\infty dq \int_{\max(-q, q-2p, \frac{q-2p}{3})}^q d\omega \int_{\frac{q+\omega}{2}}^{p+2\omega} dk. \qquad (28c)$$

The components q^i of Eq. (26) in the "p-frame" read

$$q^1 = q\sqrt{1 - v_{pq}^2} \cos\phi_{pq}, \qquad (29a)$$

$$q^2 = q\sqrt{1 - v_{pq}^2} \sin\phi_{pq}, \qquad (29b)$$

$$q^3 = q v_{pq}. \qquad (29c)$$

The angles between $\mathbf{p}$, $\mathbf{q}$, $\mathbf{k}$, and $\mathbf{k}'$ are then given by

$$v_{pq} = \frac{\omega}{q} + \frac{t}{2pq}, \qquad (30a)$$

$$v_{kq} = \frac{\omega}{q} - \frac{t}{2kq}, \qquad (30b)$$

$$v_{k'q} = \frac{\omega}{q} + \frac{t}{2k'q}, \qquad (30c)$$

and the polar angles of $\mathbf{k}$ and $\mathbf{k}'$ in the "lab-frame" by

$$v_k = \sin\phi_{kq}\sin\phi_{pq}\sqrt{1-v_{kq}^2}\sqrt{1-v_p^2} - \cos\phi_{kq}\sqrt{1-v_{kq}^2}$$
$$\times\left(\cos\phi_{pq}v_{pq}\sqrt{1-v_p^2} + v_p\sqrt{1-v_{pq}^2}\right)$$
$$+ v_{kq}\left(v_pv_{pq} - \cos\phi_{pq}\sqrt{1-v_p^2}\sqrt{1-v_{pq}^2}\right), \quad (30d)$$

$$v_{k'} = \sin\phi_{kq}\sin\phi_{pq}\sqrt{1-v_{k'q}^2}\sqrt{1-v_p^2} - \cos\phi_{kq}\sqrt{1-v_{k'q}^2}$$
$$\times\left(\cos\phi_{pq}v_{pq}\sqrt{1-v_p^2} + v_p\sqrt{1-v_{pq}^2}\right)$$
$$+ v_{k'q}\left(v_pv_{pq} - \cos\phi_{pq}\sqrt{1-v_p^2}\sqrt{1-v_{pq}^2}\right), \quad (30e)$$

and

$$k' = k - \omega, \quad (30f)$$

$$t = \omega^2 - q^2, \quad (30g)$$

$$s = -\frac{t}{2q^2}\left((p+p')(k+k') + q^2\right.$$
$$\left. - \sqrt{(4pp'+t)(4k'k+t)}\cos\phi_{kq}\right), \quad (30h)$$

$$u = \frac{t}{2q^2}\left((p+p')(k+k') - q^2\right.$$
$$\left. - \sqrt{(4pp'+t)(4k'k+t)}\cos\phi_{kq}\right), \quad (30i)$$

$$p' = p + \omega. \quad (30j)$$

Recall that $\nu_a = 2d_R$, where d_R is the dimension of the representation of the jet particle. The upper sign in Eq. (26) is to be used when the d particle is a boson (gluon), and the lower sign if it is a fermion (quark). Here the Mandelstam variables s, t, and u are defined as in Ref. [7] with respect to the momenta corresponding to the particles with labels a, b, c, d,

$$s = -(P+K)^2, \quad t = -(P'-P)^2, \quad u = -(K'-P)^2. \quad (31)$$

The expressions for s, u as in Eqs. (30h) and (30i) can also be found in [79]. Note that we defined the components $\hat{q}^{ij}$ with respect to the jet direction. If the jet moves perpendicular to the beam-axis z in the x-direction as in Fig. 1, then $v_p = \cos\theta_p = 0$ and $\hat{q}^{yy} = \hat{q}^{22}$ is the momentum broadening in the y direction and $\hat{q}^{zz} = \hat{q}^{11}$ is the momentum broadening in the beam direction, which sum to the usual $\hat{q} = \hat{q}^{11} + \hat{q}^{22}$. We can also express momentum broadening along the jet direction, i.e., longitudinal momentum broadening, by $\hat{q}_L = \hat{q}^{33}$. If we replace $\hat{q}^i\hat{q}^j$ by ω in (26), we obtain collisional energy loss.

D. Symmetries of $\hat{q}^{ij}$

Obtaining the symmetries of the matrix $\hat{q}^{ij}$ is complicated by the fact that the angle ϕ_{kq} appears both in the matrix element (via s and u), and in the distribution functions $f(\mathbf{k})$ and $f(\mathbf{k}-\mathbf{q})$ through v_k and $v_{k'}$. They also depend on ϕ_{pq}, which enters q^i. Nevertheless, in the case of a *spherically* symmetric phase-space density $f(k)$ it is easy to see that

$$\hat{q}^{12} = \hat{q}^{13} = \hat{q}^{23} = 0, \quad \hat{q}^{11} = \hat{q}^{22}, \quad (32)$$

due to (29a) and (29b).

For a phase-space density that is *azimuthally* symmetric around the z-axis (beam direction), i.e., the most general case we are considering here with $f(k, v_k)$, we also find that

$$\hat{q}^{12} = \hat{q}^{23} = 0. \quad (33)$$

If the jet is additionally moving in the x direction, i.e., $v_p = 0$, we also obtain $\hat{q}^{13} = 0$. For a jet moving in the beam direction, $v_p = 1$, the quantity v_k does not depend on ϕ_{pq} any longer and one has $\hat{q}^{13} = 0$ as well. In summary, we have

$$\hat{q}^{13} = 0, \quad \text{if } v_p = 0 \quad \text{or} \quad v_p = 1. \quad (34)$$

The fact that $\hat{q}^{12} = \hat{q}^{23} = 0$ can be seen by rewriting the angular integrals $\int_0^{2\pi}d\phi_{pq}\int_0^{2\pi}d\phi_{kq}g(\phi_{pq},\phi_{kq}) = \int_{-\pi}^{\pi}d\phi_{pq}\int_{-\pi}^{\pi}d\phi_{kq}g(\phi_{pq},\phi_{kq})$ and then splitting the ϕ_{pq} integral into the integral from $(-\pi, 0)$ and $(0, \pi)$ to arrive at

$$\int_0^{2\pi}d\phi_{pq}\int_0^{2\pi}d\phi_{kq}g(\phi_{pq},\phi_{kq})$$
$$= \int_0^{\pi}d\phi_{pq}\int_{-\pi}^{\pi}d\phi_{kq}[g(-\phi_{pq},-\phi_{kq}) + g(\phi_{pq},\phi_{kq})].$$

The angles ϕ_{kq} and ϕ_{pq} appear in v_k and $v_{k'}$, which are not changed by simultaneously replacing $\phi_{kq} \to -\phi_{kq}$ and $\phi_{pq} \to -\phi_{pq}$. In the matrix element, ϕ_{kq} appears in s and u in the cosine argument, which is an even function. The only change happens in $q_2^2 \to -q_2^2$, which results in $\hat{q}^{12} = \hat{q}^{23} = 0$.

To see that $\hat{q}^{13} = 0$ for $v_p = 0$, we can look at $\phi_{pq} \to \phi_{pq} + \pi$, which, for $v_p = 0$ changes $v_k \to -v_k$, but $f(k, -v_k) = f(k, v_k)$ and thus this only results in $q^1 \to -q^1$. Thus we obtain $\hat{q}^{13} = 0$.

E. Matrix elements

We started our derivation of $\hat{q}$ with the collision term $C^{2\leftrightarrow2}$ of Ref. [7] and thus started with the same matrix elements. They are symmetric under the exchanges $(abcd) \to (cdab)$, $(abcd) \to (bacd)$, and $(abcd) \to (abdc)$. Thus, the matrix element labeled there "$q_1g \leftrightarrow q_1g$" also

TABLE I. Matrix elements for $\hat{q}$, obtained from the matrix elements from Ref. [7] by breaking the symmetry of exchanging outgoing particles. They are obtained by replacing $c \leftrightarrow d$ and $t \leftrightarrow u$. Singly-underlined denominators indicate infrared-sensitive contributions from soft-gluon exchange and double-underlined denominators from soft-fermion exchange. The group constants are given by $d_F = C_A = N_C$, $d_A = N_C^2 - 1$, and $C_F = d_A/(2N_C)$.

$ab \leftrightarrow cd$	$|\mathcal{M}_{cd}^{ab}|^2/g^4$
$q_1 q_2 \leftrightarrow q_1 q_2$ $q_1 \bar{q}_2 \leftrightarrow q_1 \bar{q}_2$ $\bar{q}_1 q_2 \leftrightarrow \bar{q}_1 q_2$ $\bar{q}_1 \bar{q}_2 \leftrightarrow \bar{q}_1 \bar{q}_2$	$8 \frac{d_F^2 C_F^2}{d_A} \left(\frac{s^2+u^2}{\underline{t^2}} \right)$
$q_1 q_2 \leftrightarrow q_2 q_1$ $q_1 \bar{q}_2 \leftrightarrow \bar{q}_2 q_1$ $\bar{q}_1 q_2 \leftrightarrow q_2 \bar{q}_1$ $\bar{q}_1 \bar{q}_2 \leftrightarrow \bar{q}_2 \bar{q}_1$	$8 \frac{d_F^2 C_F^2}{d_A} \left(\frac{s^2+t^2}{u^2} \right)$
$q_1 q_1 \leftrightarrow q_1 q_1$ $\bar{q}_1 \bar{q}_1 \leftrightarrow \bar{q}_1 \bar{q}_1$	$8 \frac{d_F^2 C_F^2}{d_A} \left(\frac{s^2+u^2}{\underline{t^2}} + \frac{s^2+t^2}{u^2} \right) + 16 d_F C_F \left(C_F - \frac{C_A}{2} \right) \frac{s^2}{tu}$
$q_1 \bar{q}_1 \leftrightarrow q_1 \bar{q}_1$	$8 \frac{d_F^2 C_F^2}{d_A} \left(\frac{s^2+u^2}{\underline{t^2}} + \frac{t^2+u^2}{s^2} \right) + 16 d_F C_F \left(C_F - \frac{C_A}{2} \right) \frac{u^2}{st}$
$q_1 \bar{q}_1 \leftrightarrow \bar{q}_1 q_1$	$8 \frac{d_F^2 C_F^2}{d_A} \left(\frac{s^2+t^2}{u^2} + \frac{u^2+t^2}{s^2} \right) + 16 d_F C_F \left(C_F - \frac{C_A}{2} \right) \frac{t^2}{su}$
$q_1 \bar{q}_1 \leftrightarrow q_2 \bar{q}_2$ $q_1 \bar{q}_1 \leftrightarrow \bar{q}_2 q_2$	$8 \frac{d_F^2 C_F^2}{d_A} \left(\frac{t^2+u^2}{s^2} \right)$
$q_1 \bar{q}_1 \leftrightarrow gg$	$8 d_F C_F^2 \left(\frac{u}{\underline{t}} + \frac{t}{\underline{u}} \right) - 8 d_F C_F C_A \left(\frac{t^2+u^2}{s^2} \right)$
$q_1 g \leftrightarrow q_1 g$ $\bar{q}_1 g \leftrightarrow \bar{q}_1 g$	$-8 d_F C_F^2 \left(\frac{u}{s} + \frac{s}{\underline{u}} \right) + 8 d_F C_F C_A \left(\frac{s^2+u^2}{\underline{t^2}} \right)$
$q_1 g \leftrightarrow g q_1$ $\bar{q}_1 g \leftrightarrow g \bar{q}_1$	$-8 d_F C_F^2 \left(\frac{t}{s} + \frac{s}{\underline{t}} \right) + 8 d_F C_F C_A \left(\frac{s^2+t^2}{u^2} \right)$
$gg \leftrightarrow gg$	$16 d_A C_A^2 \left(3 - \frac{su}{\underline{t^2}} - \frac{st}{u^2} - \frac{tu}{s^2} \right)$

describes the processes "$q_1 g \leftrightarrow g q_1$," "$g q_1 \leftrightarrow q_1 g$," and "$g q_1 \leftrightarrow g q_1$."

Due to our choice $p' > k'$, we break the symmetry of exchanging the outgoing particles, $(abcd) \to (abdc)$, which means that we now have to distinguish between "$q_1 g \leftrightarrow q_1 g$" and "$q_1 g \leftrightarrow g q_1$." This enlarges the number of matrix elements. We obtain them from [7] by relabeling $p' \leftrightarrow k'$ and $c \leftrightarrow d$, which effectively means [see (31)]

$$s \to s, \qquad t \to u, \qquad u \to t. \qquad (35)$$

The resulting matrix elements are still symmetric under $(abcd) \to (badc)$ and are listed in Table I.

F. Screening using HTL

Screening becomes important when the Mandelstam variable t becomes small $s \gg t \sim \mathcal{O}(m_D^2)$. This concerns the underlined terms with inverse powers of t in the matrix elements listed in Table I, which need to be modified to

account for medium screening [7]. Due to our requirement $p' > k'$ we could only have $|u| \ll s$ when $k \gg p$, which is highly suppressed by the fact that we are choosing p to be hard and k to be a medium particle. This we have also checked numerically. Thus, unlike in Ref. [7], we only need to consider for screening the terms with t in the denominator.

We follow the prescription of Ref. [7] to include medium modifications by replacing[4] the singly underlined terms in the matrix elements in Table I by

$$M_0 = \frac{(s-u)^2}{t^2}$$
$$\to |G_R(P-P')_{\mu\nu}(P+P')^\mu(K+K')^\nu|^2 \equiv M_{\text{screen}}, \quad (36)$$

where G_R denotes the retarded gluon propagator in the HTL approximation. It should be noted that, as also discussed in [7], for anisotropic systems, this prescription in general leads to instabilities [47,49,80,81]. It is currently unknown how to properly treat these instabilities in kinetic theory. Note however that there is numerical evidence that suggests that the quantitative effect of the instabilities on the plasma evolution is less dramatic [63,64] than expected from power counting arguments [62]. Here, we will use two different approximations, such that these instabilities are not present: First, we will use the isotropic gluon propagator, which includes the isotropic HTL expressions for the self-energy. Second, we will use a simple screening prescription that is also commonly used in EKT simulations [71].

All the singly underlined terms in Table I can be rewritten in terms of the same unscreened gluon propagator M_0,

$$\frac{s^2+u^2}{t^2} = \frac{1}{2} + \frac{1}{2}M_0, \qquad \frac{su}{t^2} = \frac{1}{4} - \frac{1}{4}M_0. \qquad (37)$$

In the following, we will use different screening approximations for the retarded HTL propagator M_{screen}. First, we use the full isotropic HTL propagators, which can be expressed as (see Appendix B for details)

$$M_{\text{HTL}} = \frac{c_1^2}{A^2+B^2} + \frac{c_2^2}{C^2+D^2} - \frac{2c_1 c_2 (AC+BD)}{(A^2+B^2)(C^2+D^2)}, \qquad (38)$$

where A, B, C, D are obtained from the real and imaginary parts of the retarded HTL self-energies and are explicitly given by

$$A = q^2 + m_D^2 \left(1 + \frac{\omega}{2q} \ln \frac{q-\omega}{q+\omega} \right), \qquad (39a)$$

---

[4]It is easy to see that inserting the free propagator $G_0(Q)_{\mu\nu} = \frac{\eta_{\mu\nu}}{Q^2}$ yields $(s-u)^2/t^2$. As argued in Ref. [7], due to the spin independence of the matrix elements at leading order, one can use a theory with fictitious scalar quarks for the infrared screening of the matrix elements. Then this prescription arises naturally.

$$B = -\frac{m_D^2 \omega}{2q} \pi, \tag{39b}$$

$$C = q^2 - \omega^2 + \frac{m_D^2}{2}\left(\frac{\omega^2}{q^2} + \left(\frac{\omega^2}{q^2} - 1\right)\frac{\omega}{2q}\ln\frac{q-\omega}{q+\omega}\right), \tag{39c}$$

$$D = \frac{\pi m_D^2 \omega}{4q}\left(1 - \frac{\omega^2}{q^2}\right), \tag{39d}$$

and

$$c_1 = (2p + \omega)(2k - \omega), \tag{40a}$$

$$c_2 = 4pk\sin\theta_{pq}\sin\theta_{kq}\cos\phi_{kq}. \tag{40b}$$

Note that, for isotropic distributions, the last term in Eq. (38) can be dropped, since it is proportional to $\cos\phi_{kq}$ and will thus vanish in the angular integration of $\hat{q}$.

The doubly-underlined terms in Table I correspond to soft fermionic exchange. We do not consider them here explicitly because, as we will discuss in Sec. III H, they are subleading in $1/p$.

There is an approximation to the isotropic HTL matrix element M_{HTL} that is commonly used in numerical simulations of the time evolution in EKT [8,71–74,78] and that is also computationally more efficient. This approximation, which we will refer to as the ξ-screening prescription, amounts to the replacement [71]

$$M_{\text{HTL}} \to M_\xi = \frac{(s-u)^2}{t^2}\frac{q^4}{(q^2 + \xi^2 m_D^2)^2}. \tag{41}$$

This replacement can be justified when we are not directly interested in the matrix element but in the (weighted) integral over it, as in computations of $\hat{q}$ or $\mathcal{C}^{2\leftrightarrow2}$. The approximate matrix element M_ξ agrees with M_{HTL} at large q, but behaves differently in the small q region. It includes a constant ξ that is fixed such that the integral over the approximated matrix element matches the result of the full isotropic HTL matrix element. For transverse momentum broadening, this integral needs to be taken in the high-energy limit $p \to \infty$, be weighted with $q_\perp^2$, and integrated over $d^2\mathbf{q}_\perp$ to obtain $\hat{q}$. Thus we fix ξ by requiring such that

$$\int_0^\infty dq_\perp q_\perp^3 \int_{-\infty}^\infty \frac{d\omega}{\sqrt{q_\perp^2 + \omega^2}}\int_0^{2\pi} d\phi_{kq}(M_{\text{HTL}} - M_\xi) = 0. \tag{42}$$

In [71] one is matching the longitudinal momentum transfer rather than the transverse one, which leads to a different value for ξ.

To evaluate these integrals we take both matrix elements in the limit $p \to \infty$, and additionally consider the soft limit $\omega \ll k, q_\perp \ll k$. We then first integrate over ω. For M_{HTL}
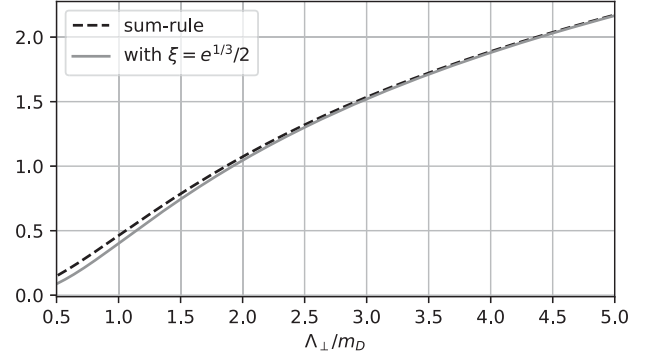

FIG. 3. Shown are the HTL sum rule results on the left-hand side of Eq. (43) as a dashed curve and the values from the approximated expression on its right-hand side with the parameter ξ given by (44) as a continuous line. The plot shows that for $\Lambda_\perp \gtrsim 4m_D$ the screening approximation of the full HTL matrix element provides accurate results.

this can, in the soft limit, be done analytically using a sum rule [32], which we discuss in more detail in Appendix B 1. Then we perform the $q_\perp$ integral up to a cutoff $\Lambda_\perp$ and obtain the following condition:

$$\frac{2}{3}\ln\left(1 + \frac{\Lambda_\perp^2}{m_D^2}\right)$$
$$= 4\ln\frac{\Lambda_\perp}{2\xi m_D} - \frac{\Lambda_\perp^2}{(\xi m_D)^2}$$
$$- \frac{(\Lambda_\perp^4 + 2\Lambda_\perp^2(\xi m_D)^2 + 4(\xi m_D)^4)\ln\frac{\Lambda_\perp}{\xi m_D + \sqrt{\Lambda_\perp^2 + (\xi m_D)^2}}}{(\xi m_D)^3\sqrt{\Lambda_\perp^2 + m_D^2}} \tag{43}$$

where the left-hand side comes from M_{HTL}. Expanding both sides of the equation for large cutoff $\Lambda_\perp \gg \xi m_D$ leads to

$$\xi = \frac{e^{1/3}}{2} \approx 0.6978. \tag{44}$$

We show in Fig. 3 that both sides of Eq. (43) are indeed in very good agreement for $\Lambda_\perp \gtrsim 4m_D$, justifying the validity of the approximation for sufficiently large momentum cutoffs. We note that the value for ξ in Eq. (44) entering the matrix element in $\hat{q}$ is slightly different from the one typically used in the elastic collision kernel $\mathcal{C}^{2\leftrightarrow2}$ in kinetic theory simulations of the thermalization dynamics of the quark-gluon plasma [8,71–74,78]. While the matrix element is approximated in a similar manner as here, for the thermalization dynamics ξ is fixed by demanding that longitudinal momentum broadening agrees with the one from HTL matrix elements entering $\mathcal{C}^{2\leftrightarrow2}$. In contrast, $\hat{q}$ requires that the transverse momentum broadening agrees instead.

With the ξ-screening prescription, the gluonic matrix element in Table I becomes[5]

$$\frac{|\mathcal{M}_{gg}^{gg}|^2}{16 d_A C_A^2 g^4} \to \frac{11}{4} - \frac{(s-u)^2}{4t^2}\frac{q^4}{(q^2+\xi^2 m_D^2)^2} - \frac{st}{u^2} - \frac{tu}{s^2}. \quad (45)$$

We will investigate this approximation in Sec. IV numerically by comparing it to the HTL screened results. For instance, we find that the largest differences occur for a small cutoff $\Lambda_\perp$ or a large coupling λ. For the physically motivated values $\lambda = 10$ and $\Lambda_\perp = T$ we obtain a 30% deviation, showing that the choice of the screening prescription can be important for the evaluation of $\hat{q}$. To be safe from this effect, we have used the full HTL screening prescription for $\hat{q}$ in our study of the jet quenching parameter during bottom-up thermalization in Ref. [20].

G. Towards the limit $p \to \infty$: NLO terms in $1/p$

In the derivation of $\hat{q}$, we have considered the jet momentum p to be much larger than all other momentum scales of the plasma. However, in the strict limit $p \to \infty$ the momentum diffusion coefficient $\hat{q}$ has a logarithmic divergence, unless the exchanged momentum is limited by a cutoff. We will first, in this subsection, discuss the limit of p being large, but not infinite. Then, in Sec. III H, we will introduce a cutoff on $q_\perp$ and take $p \to \infty$. In the limit of large p, only the terms su/t^2 and $(s^2+u^2)/t^2$ in the matrix elements (Table I) are $\sim p^2$ and thus contribute.

For example, let us consider the screened gluonic matrix element (45)

$$\frac{|\mathcal{M}_{gg}^{gg}|^2}{p^2} = 16 d_A C_A^2 \frac{\left(2k - \omega - \sqrt{(2k-\omega)^2 - q^2}\cos\phi_{kq}\right)^2}{(q^2+\xi^2 m_D^2)^2}$$
$$\times \left(1 + \frac{\omega}{p} + \mathcal{O}\left(\frac{1}{p^2}\right)\right). \quad (46)$$

Here k is a medium momentum scale (the collision integral is proportional to $f(\mathbf{k})$) and we can thus assume that $k \ll p$ even if formally k is integrated over up to infinity. Naïvely, we could assume that $\frac{\omega}{p} \sim \mathcal{O}(\frac{1}{p})$. However, p appears also in the lower integration limit of ω [see Eq. (28a)], and we therefore consider the term proportional to ω/p more carefully. For positive ω one has $\omega < k \ll p$, such that it becomes indeed negligible. For negative ω, however, one has

$$\left|\frac{\omega}{p}\right| = \frac{-\omega}{p} < \frac{p-k}{2p} = \frac{1}{2} - \frac{k}{2p}, \quad (47)$$

---

[5]The unusual value of the constant $11/4$ stems from rewriting su/t^2 according to Eq. (37).

which does not vanish for $p \to \infty$. However, a more careful calculation (carried out explicitly in Appendix C) shows that the leading large p contribution in Eq. (46) diverges logarithmically $\sim \ln p$, whereas the $\mathcal{O}(\omega/p)$ contribution becomes constant in p. Thus indeed the leading behavior is obtained by assuming $p \gg \omega$ term in the matrix element.

In summary, we now know, that for large jet energies $E_{\text{jet}} = p$, the jet quenching parameter is given by

$$\hat{q}(p \gg T_\varepsilon) \simeq a_p \ln p + b_p. \quad (48)$$

Here, T_ε is the characteristic momentum scale of plasma particles, e.g., the temperature in thermal equilibrium. For nonequilibrium systems, such a scale can be obtained, for example, as the temperature of an equilibrium system with the same energy density. The coefficient a_p for isotropic distributions is derived explicitly in Appendix C as

$$a_p/C_R = \frac{C_A g^4}{4\pi^3} \int_0^\infty dk\, k^2 f_g(k)$$
$$+ \sum_f \frac{d_F C_F g^4}{4\pi^3 d_A} \int_0^\infty dk\, k^2 f_f(k), \quad (49)$$

where f_g is the gluon distribution function and the subscript f in f_f labels different quark species. $q_\perp < \Lambda_\perp$, then for $p \to \infty$ it becomes indeed sufficient to only consider the leading order contribution in Eq. (46) since the other terms are then suppressed.

H. Limit $p \to \infty$ with a momentum cutoff

Let us now introduce a cutoff for the transverse component of the momentum exchange in the scattering

$$q_\perp^2 = q^2 - \omega^2 < \Lambda_\perp^2. \quad (50)$$

Compared to the case without the cutoff, $q_\perp$ is now not restricted by the large p but by $\Lambda_\perp$ and we do not need to worry about the $\omega \sim p$ region as in Sec. III G. The behavior of the phase-space integral with a cutoff $q_\perp < \Lambda_\perp$ is also analyzed in more detail in Appendix C.

We now directly take the limit $p \to \infty$ in the matrix element, which considerably simplifies the calculation. The required matrix elements are written down in Table II. Now only t-channel gluon exchanges contribute, as depicted in Fig. 4. Apart from that, few changes need to be made to the formula of $\hat{q}$ presented in Sec. III C. Equation (26) remains valid, i.e.,

$$\hat{q}^{ij} = \frac{1}{2^9 \pi^5 \nu_a} \sum_{bcd} \int d\Gamma\, q^i q^j \frac{|\mathcal{M}_{cd}^{ab}|^2}{p^2} f_b(k,v_k)(1 \pm f_d(k',v_{k'})), \quad (51)$$

TABLE II. The matrix elements for $\hat{q}$ as in Table I in the limit $p \to \infty$. Here $\tilde{M}_{\text{screen}} = \lim_{p \to \infty} M_{\text{screen}}/p^2$ denotes the appropriate screening terms $\tilde{M}_{\text{HTL}}$ or $\tilde{M}_{\xi}$ as explained in Sec. III F and Appendix B, and quark flavors are labeled by the index i.

$ab \leftrightarrow cd$	$\lim_{p \to \infty} \lvert \mathcal{M}_{cd}^{ab} \rvert^2 / (p^2 g^4)$
$q_1 q_i \leftrightarrow q_1 q_i$	$4 \frac{d_{\text{F}}^2 C_{\text{F}}^2}{d_{\text{A}}} \tilde{M}_{\text{screen}}$
$\bar{q}_1 q_i \leftrightarrow \bar{q}_1 q_i$ $q_1 \bar{q}_i \leftrightarrow q_1 \bar{q}_i$ $\bar{q}_1 \bar{q}_i \leftrightarrow \bar{q}_1 \bar{q}_i$	
$q_1 g \leftrightarrow q_1 g$ $\bar{q}_1 g \leftrightarrow \bar{q}_1 g$	$4 d_{\text{F}} C_{\text{F}} C_{\text{A}} \tilde{M}_{\text{screen}}$
$gg \leftrightarrow gg$	$4 d_{\text{A}} C_{\text{A}}^2 \tilde{M}_{\text{screen}}$

with the integration measure $\int d\Gamma$ in (27). However, the term $\int d\Gamma_3$ of the measure given by Eq. (28) and the kinematic variables need adjustments. As before, the upper and lower signs in the term $(1 \pm f_d)$ denote bosonic particles (gluons) and fermionic particles (quarks), respectively.

In particular, in (28a) and (28b) we just need to adjust the upper integration limit of the q integral. For (28c) we implement the condition (50) in the ω integral, $\omega^2 > q^2 - \Lambda_\perp^2$, which only changes the integral boundaries for $q > \Lambda_\perp$. We can thus write the integration measures as

$$\int d\Gamma_3 = \int_0^\infty dk \int_{-\infty}^k d\omega \int_{|\omega|}^{\min(2k-\omega, \sqrt{\omega^2+\Lambda_\perp^2})} dq \quad (52a)$$

$$= \int_0^\infty dk \int_0^\infty dk' \int_{|k-k'|}^{\min(k+k', \sqrt{(k-k')^2+\Lambda_\perp^2})} dq \quad (52b)$$

$$= \left(\int_{\Lambda_\perp}^\infty dq \left[\int_{-q}^{-\sqrt{q^2-\Lambda_\perp^2}} d\omega + \int_{\sqrt{q^2-\Lambda_\perp^2}}^q d\omega \right] \right. \left. + \int_0^{\Lambda_\perp} dq \int_{-q}^q d\omega \right) \times \int_{\frac{q+\omega}{2}}^\infty dk. \quad (52c)$$

Plasma particle
(quark, gluon)

K   K-Q

Leading jet parton   Outgoing jet parton
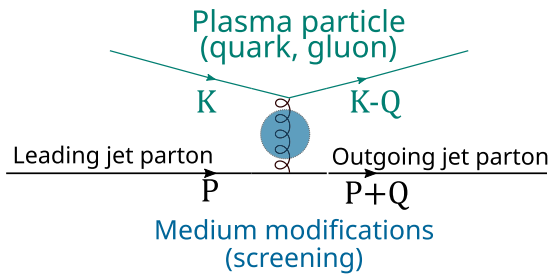P   P+Q

Medium modifications
(screening)

FIG. 4. Feynman diagram for the t-channel gluon exchange processes that dominate the matrix element for $\hat{q}$ in the high-energy limit $p \to \infty$. In the internal gluon propagator, medium effects should be included as explained in Sec. III F.

In this limit, one needs to replace (30a) by $v_{pq} = \omega/q$ (see Appendix C) and the few nonvanishing matrix elements for $\lim_{p \to \infty} \frac{\lvert \mathcal{M} \rvert^2}{p^2}$ that are given in Table II are expressed in terms of the same screening matrix element. Thus we do not need the explicit expressions (30h) and (30i) for s, u in terms of our phase space integration variables. From the matrix elements in Table II and (26), one finds Casimir scaling

$$\frac{\hat{q}^{\text{gluon}}}{C_{\text{A}}} = \frac{\hat{q}^{\text{quark}}}{C_{\text{F}}}. \quad (53)$$

The screening in $\tilde{M}_{\text{screen}}$ in the matrix elements in Table II is implemented as detailed in Sec. III F. In the $p \to \infty$ limit, the isotropic HTL matrix element from Eq. (38) becomes

$$\tilde{M}_{\text{HTL}} = \frac{\tilde{c}_1^2}{A^2+B^2} - \frac{\tilde{c}_2^2}{C^2+D^2} + \frac{2\tilde{c}_1\tilde{c}_2(AC+BD)}{(A^2+B^2)(C^2+D^2)}, \quad (54)$$

with the parameters A, B, C, and D given by (39) and

$$\tilde{c}_1 = \lim_{p \to \infty} \frac{c_1}{p} = 2(2k-\omega), \quad (55a)$$

$$\tilde{c}_2 = \lim_{p \to \infty} \frac{c_2}{p} = 4k \sin\theta_{pq} \sin\theta_{kq} \cos\phi_{kq}. \quad (55b)$$

Again, for isotropic systems, we do not need to include the last term in (54), since it vanishes in the angular integral when calculating $\hat{q}^{ij}$. We refer to Appendix B for details of the derivation.

For the ξ-screening approximation, we obtain [cf., (41)]

$$\tilde{M}_\xi = 4 \frac{\left(2k - \omega - \sqrt{(2k-\omega)^2 - q^2} \cos\phi_{kq} \right)^2}{(q^2 + \xi^2 m_D^2)^2}, \quad (56)$$

with $\xi = e^{1/3}/2$ as before.

I. Limiting behavior for large cutoff

The jet quenching parameter $\hat{q}$ exhibits a logarithmic behavior when the cutoff $\Lambda_\perp$ exceeds the typical hard momenta T_ε of the plasma constituents.

$$\hat{q}(\Lambda_\perp \gg T_\varepsilon) \simeq a_{\Lambda_\perp} \ln \Lambda_\perp + b_{\Lambda_\perp}, \quad (57)$$

where for isotropic distributions

$$a_{\Lambda_\perp}/C_{\text{R}} \simeq \frac{C_{\text{A}} g^4}{2\pi^3} \int_0^\infty dk \, k^2 f_g(k)$$
$$+ \sum_f \frac{d_{\text{F}} C_{\text{F}} g^4}{2\pi^3 d_{\text{A}}} \int_0^\infty dk \, k^2 f_f(k). \quad (58)$$

This is the same logarithmic behavior as in Eq. (49), keeping in mind that now the phase space is limited by $\Lambda_\perp^2$ rather than p, and thus $\ln p$ gets replaced by $2 \ln \Lambda_\perp$.

For thermal equilibrium, this yields

$$\hat{q}^{\text{therm}}(\Lambda_\perp \gg T) \simeq \frac{C_{\text{R}}}{\pi^3} g^4 \zeta(3) T^3 \left(N_{\text{C}} + \frac{3}{4} n_{\text{f}} \right) \ln \Lambda_\perp + \text{const}, \tag{59}$$

which is Eq. (C35) in Appendix C 5 and agrees with [30], as we will later discuss around Eq. (81a).

As discussed further in Appendix C 5, for anisotropic systems Eq. (58) only gives a rough estimate for the coefficient $a_{\Lambda_\perp}$. For anisotropic distributions one still expects a logarithmic behavior $\hat{q}^{ii}(\Lambda_\perp \gg Q) \simeq (a_{\Lambda_\perp})_i \times \ln \Lambda_\perp + (b_{\Lambda_\perp})_i$, but with different coefficients depending on the direction.

J. Interpreting the momentum cutoff

A peculiar feature of the jet quenching parameter $\hat{q}$ is its dependence on a transverse momentum cutoff $\Lambda_\perp$. Let us discuss here briefly how to interpret this cutoff in physical terms and how its value could be chosen. In our kinetic picture, the cutoff stems from employing the eikonal limit, which means taking the jet momentum $p \to \infty$. In this case the jet particle can inject an unrestricted amount of transverse momentum in the collision, leading to a logarithmic divergence that has to be regulated by introducing a cutoff $\Lambda_\perp$, which restricts transverse momentum transfer $q_\perp < \Lambda_\perp$. Practically all analytic calculations that rely on quasiparticles or hard-thermal loop frameworks, but even with different interaction potentials, need to employ this cutoff (as, e.g., in [30,31,44,45,53,77,82]).

A simple way of setting the cutoff is to use the relation between the coefficient $a_{\Lambda_\perp}$ for large cutoff $\Lambda_\perp$ and the coefficient a_p for large (finite) jet energy p [see Eqs. (49) and (58)]. Requiring that the dynamics of jet quenching calculated with a cutoff in the $p \to \infty$ approximation would have the same leading logarithmic behavior as a kinematically more accurate one with a finite p, we should choose the cutoff such that

$$\Lambda_\perp^{\text{kin}} \sim \sqrt{pT}, \tag{60}$$

where p is the energy of the jet parton and T is an additional dimensionful scale (e.g., the temperature in equilibrium). This kinematic cutoff $\Lambda_\perp^{\text{kin}}$ is widely used in the literature [43–45,65,77,83–85].

While this is a straightforward result of our definition for $\hat{q}$ in Eq. (1), it encodes only the momentum diffusion due to elastic $2 \leftrightarrow 2$ scattering processes, and competing inelastic effects like splittings or gluon emissions are neglected. Which effects one needs to include, and thus, which cutoff to use, depends in fact on the type of process where the

value of $\hat{q}$ is used. For radiative energy loss calculations, one can restrict the cutoff by considering the rate of momentum exchange processes and comparing it with the "lifetime" of the leading parton under consideration. During an LPM splitting process this corresponds to the "formation time" t^{form}. We are therefore interested in the accumulated transverse momentum until a splitting occurs. To calculate radiative energy loss of the leading parton, typical calculations (e.g., within the BDMPS-Z formalism [22–24] or related approaches [25]) use the so-called harmonic oscillator approximation, in which the jet quenching parameter $\hat{q}$ naturally appears in the expansion of the interaction potential in position space, $v(\mathbf{b}) \simeq \frac{1}{4} \hat{q} \mathbf{b}^2$. In the leading-log approximation, it is sufficient to use a momentum cutoff $\Lambda_\perp$ of the order of the typical total momentum transfer $Q_\perp$ during the formation time [25]. By definition, it is given by $Q_\perp^2 \sim \hat{q} t^{\text{form}}$, where for a small medium with length $L < t^{\text{form}}$ one should replace t^{form} by L. The formation time of the splitting $p \to p_1 + p_2$ can be estimated as $(t^{\text{form}})^2 \sim E_i/\hat{q}$, with E_i being the energy of the emitted gluon. It has been argued [30,86] that energy loss is dominated by processes in which both daughters share a similar energy fraction $p_1 \sim p_2 \sim p$, which enables us to use the leading-parton energy in the formation time estimate. With the parametric relation $\hat{q} \sim g^4 T^3$, we obtain for a large medium $L > t^{\text{form}}$ the expression

$$\Lambda_\perp^{\text{LPM}} \sim g(pT^3)^{1/4}. \tag{61}$$

In order to present our results in a form that can be applied in different pictures of energy loss, we give our results as functions of $\Lambda_\perp$. In our companion paper [20] we study the values of $\hat{q}$ with a time-dependent cutoff during bottom-up thermalization, and present results using both scaling choices (60) and (61).

K. Numerical implementation

Numerically, we obtain $\hat{q}$ in the limit $p \to \infty$ with a momentum cutoff $\Lambda_\perp$ according to (51) with the integration measure[6] (52c) using Monte Carlo integration with importance sampling. For more details we refer to Appendix D. The error bars in the figures correspond to the statistical uncertainty of the Monte Carlo integration.

All our numerical results are obtained for a purely gluonic plasma, i.e., $n_{\text{f}} = 0$. Although we extract the jet quenching parameter for a gluonic jet, its value for a quark jet is related via Casimir scaling, i.e., $\hat{q}^{\text{quark}} = \frac{C_{\text{F}}}{C_{\text{A}}} \hat{q}^{\text{gluon}}$, as can be seen easily from Table II. Note that the number of colors N_{C} enters the gluonic jet quenching parameter $\hat{q}^{\text{gluon}}$ only via the coupling λ, but for $\hat{q}^{\text{quark}}$ we need to specify it to $N_{\text{C}} = 3$

---

[6]We have checked that also (52b) gives the same result, but in our implementation (52c) showed a faster convergence in the Monte Carlo evaluation.

for QCD. In the following, for numerical results we only show $\hat{q}^{\text{quark}} =: \hat{q}$; for analytical results we keep the Casimir factor C_R explicitly.

Our datasets and analysis scripts can be found in Ref. [87].

IV. EVALUATION OF $\hat{q}$ IN SPECIAL CASES

In our paper [20] we have evaluated $\hat{q}$ during the bottom-up thermalization process in heavy-ion collisions. Here, in order to shed more light on the qualitative features of the jet quenching parameter in different equilibrium and off-equilibrium situations, we study $\hat{q}$ in some special cases. In Sec. IV A, we first review the derivation of $\hat{q}$ for thermal systems [30,32], and compare the results with numerical evaluations of Eq. (51). We also provide an interpolation formula that reproduces the numerically obtained values of the quenching parameter in thermal equilibrium $\hat{q}^{\text{therm}}$ for different couplings and momentum cutoffs.

In Sec. IV B, we then consider toy models for the bottom-up thermalization process in heavy-ion collisions [1]. We first study an effectively two-dimensional distribution to model the large momentum-space anisotropy encountered in the initial stages in heavy-ion collisions, and then generalize the thermal results of Sec. IV A to a scaled thermal distribution to model over- and underoccupied systems that are typically encountered in the preequilibrium evolution of the quark-gluon plasma.

We also study the different contributions to $\hat{q}$ that are linear or quadratic in the distribution function, by splitting it into its individual components,

$$\hat{q} = \hat{q}_{\text{f}} + \hat{q}_{\text{ff}}. \tag{62}$$

Similarly as in Ref. [70], we can refer to $\hat{q}_{\text{f}}$ as the *classical* and $\hat{q}_{\text{ff}}$ as the *Bose-enhanced* part of $\hat{q}$.[7]

A. Thermal distribution

The equilibrium form of the particle distributions is given by

$$f_{\pm}(k;T) = \frac{1}{\exp(k/T) \mp 1}, \tag{63}$$

where T is the temperature. The upper signs f_+ denote the Bose–Einstein distribution and f_- is the Fermi–Dirac distribution.

In thermal equilibrium, $\hat{q}$ has already been calculated for the limiting cases of small and large cutoffs $\Lambda_\perp$ in [30,31],

---

[7]This Bose-enhanced term can also be considered to be a *classical field* contribution because it is dominant in highly-occupied systems $f \gg 1$ that can be studied numerically using classical-statistical simulations. This can be seen in the limit of $\lambda \to 0$ with λf held constant, in which only $\hat{q}_{\text{ff}}$ survives.

which we briefly summarize here. In Sec. IV B 2, we will generalize this derivation to the case of a scaled thermal distribution, which is obtained by rescaling a thermal distribution.

For the evaluation of $\hat{q}$, we work in the $p \to \infty$ limit with a transverse momentum cutoff $\Lambda_\perp$, as discussed in Sec. III H. Since the phase-space density is spherically symmetric, one has $\hat{q}^{11} = \hat{q}^{22}$ and we can restrict to $\hat{q} = \hat{q}^{11} + \hat{q}^{22}$. Our starting point is Eq. (52c), where we integrate over the modulus of $\mathbf{q} = (\mathbf{q}_\perp, q^3)$. For $p \to \infty$ we obtain $q^3 = \omega$ and thus

$$q^2 = q_\perp^2 + \omega^2. \tag{64}$$

It will be useful to change the integration variables from (q, ϕ_{pq}, ω) to (q^1, q^2, ω). This yields a factor q from the Jacobian

$$\int_0^{2\pi} d\phi_{pq} \int_0^\infty dq \int_{-q}^q d\omega \, \theta(\Lambda_\perp^2 + \omega^2 - q^2)$$
$$= \int_{q_\perp < \Lambda_\perp} d^2\mathbf{q}_\perp \int_{-\infty}^\infty \frac{d}{\sqrt{q_\perp^2 + \omega^2}}. \tag{65}$$

The matrix elements in Table II do not allow for identity-changing processes, which means that the leading parton a and the outgoing parton c are of the same type, $a = c$, and similarly $b = d$. Therefore, we can scale out the Casimir of the jet C_R, and the prefactors in front of $\tilde{M}_{\text{screen}}$ in Table II neatly combine with $1/\nu_a$ for the degrees of freedom of the jet particle to

$$\Xi_+ = 2N_C \tag{66a}$$

$$\Xi_- = 4n_f \frac{d_F C_F}{d_A} = 2n_f \tag{66b}$$

for scattering off a gluon and off a quark/antiquark, respectively, which leads to Casimir scaling [cf., Eq. (53)].

There are two limiting cases in which the result for $\hat{q}$ can be found analytically, for small and large momentum cutoffs, which we will study in the following.

1. Small momentum cutoff

For small $q_\perp < \Lambda_\perp \ll T$, the expression for $\hat{q}$ in Eq. (26) with the integration measure (52c), the integrals (65), and the prefactors (66) becomes

$$\hat{q}(\Lambda_\perp) = C_R \sum_{\pm} \Xi_\pm \frac{g^4}{2^9 \pi^5} \int_0^\infty dk \, f_\pm(k)(1 \pm f_\pm(k))$$
$$\times \int_0^{\Lambda_\perp} d^2\mathbf{q}_\perp q_\perp^2 \int_0^{2\pi} d\phi_{kq} \int_{-\infty}^\infty \frac{d\omega \tilde{M}_{\text{HTL}}}{\sqrt{q_\perp^2 + \omega^2}}. \tag{67}$$

We have extended the lower boundary[8] of the k-integral to 0 and approximated $f(k - \omega) \approx f(k)$. This is appropriate because large values of ω are suppressed by the matrix element $\tilde{M}_{\mathrm{HTL}}$, as can be seen from Eq. (46).

The last two integrals can be evaluated analytically using a sum rule [32] as discussed in Appendix B 1,

$$
\hat{q}(\Lambda_\perp) = \frac{C_R g^4}{(2\pi)^3} 2 \int_{q_\perp < \Lambda_\perp} \frac{\mathrm{d}^2 \mathbf{q}_\perp}{2\pi} q_\perp^2 \frac{1}{q_\perp^2 (q_\perp^2 + m_D^2)}
$$
$$
\times \sum_\pm \Xi_\pm \int_0^\infty \mathrm{d}k\, k^2 f_\pm(k)(1 \pm f_\pm(k)). \quad (68)
$$

Note that until now we have not used a specific form for the distribution function $f(k)$ and assumed only spherical symmetry. The thermal form of $\hat{q}$ for a small cutoff is then obtained by performing the integrals over the distribution function,

$$
\int_0^\infty \mathrm{d}k\, k^2 f_\pm(k) = 2T^3 \zeta_\pm(3), \quad (69a)
$$

$$
\int_0^\infty \mathrm{d}k\, k^2 (f_\pm(k))^2 = \pm 2T^3(\zeta_\pm(2) - \zeta_\pm(3)), \quad (69b)
$$

where $\zeta_+(s) = \zeta(s)$ is the Riemann Zeta function and $\zeta_-(s) = (1 - 2^{1-s})\zeta(s)$ denotes its fermionic counterpart as in Ref. [30]. Using $\zeta(2) = \pi^2/6$, we obtain

$$
\hat{q} = \int_{q_\perp < \Lambda_\perp} \mathrm{d}^2 \mathbf{q}_\perp q_\perp^2 \times \frac{g^2 C_R T}{(2\pi)^2} \frac{m_D^2}{q_\perp^2 (q_\perp^2 + m_D^2)}, \quad (70)
$$

from which we can read off the elastic scattering rate $\frac{\mathrm{d}\Gamma_{\mathrm{el}}}{\mathrm{d}^2 q_\perp}$ as in (3). This leads us to the thermal form of $\hat{q}$ for a small cutoff,[9]

$$
\hat{q}^{\mathrm{therm}}(\Lambda_\perp \ll T) = \frac{g^2}{4\pi} C_R T m_D^2 \ln\left(1 + \frac{\Lambda_\perp^2}{m_D^2}\right). \quad (71)
$$

For a thermal system, the terms containing $\zeta_\pm(3)$ cancel if we consider the total $\hat{q}$, but are important if one considers the *Bose-enhanced* part separately, as in (62). Splitting off

---

[8]The largest error of this approximation comes from the f_+^2 term. It can by estimated by $\int_0^{\frac{q+\omega}{2}} k^2 f_+^2 < \frac{q+\omega}{2} \lim_{k \to 0}(k^2 f_+^2)$, where the k^2 factor stems from $\tilde{M}_{\mathrm{HTL}}$ and we approximated the integral by the maximum value of the integrand at $k = 0$. This yields the error estimate $\frac{T^2(q+\omega)}{2}$, which for $q_\perp < \Lambda_\perp \ll T$ is much smaller than the leading-order contribution $\int_0^\infty k^2 f_+^2 = 2T^3(\zeta(2) - \zeta(3))$ [see Eq. (69)] for $q, \omega \ll T$.

[9]This form is actually valid in general for any isotropic distribution $f(k)$ with the replacement of $T \to T_* = \frac{\sum_s \nu_s C_s \int \mathrm{d}^3 \mathbf{p} f_s(\mathbf{p})[1 \pm f_s(\mathbf{p})]}{2 \sum_s \nu_s C_s \int \mathrm{d}^3 \mathbf{p} f_s(\mathbf{p})/p}$ and the more generally evaluated Debye mass m_D as in Eq. (8).

---

the *Bose-enhanced* term as in (62), we obtain

$$
\hat{q}_{\mathrm{f}}^{\mathrm{therm}}(\Lambda_\perp \ll T) = \zeta(3)(12N_{\mathrm{C}} + 9n_{\mathrm{f}})C_L \quad (72a)
$$

$$
\hat{q}_{\mathrm{ff}}^{\mathrm{therm}}(\Lambda_\perp \ll T) = [2N_{\mathrm{C}}(\pi^2 - 6\zeta(3))
$$
$$
+ n_{\mathrm{f}}(\pi^2 - 9\zeta(3))]C_L, \quad (72b)
$$

with $C_L = \frac{g^4 T^3 C_R}{24\pi^3} \ln\left(1 + \frac{\Lambda_\perp^2}{m_D^2}\right)$ and the thermal Debye mass given by Eq. (9b).

2. Large momentum cutoff

The jet quenching parameter in thermal equilibrium has been calculated for large cutoffs in Ref. [30]. In order to generalize this later to a scaled thermal distribution, we briefly review the derivation here. It relies on constructing an interpolating formula for the elastic scattering rate,

$$
\frac{\mathrm{d}\Gamma_{\mathrm{el}}}{\mathrm{d}^2 q_\perp} \simeq \frac{C_R}{(2\pi)^2} \times \frac{g^4 T^3 F(q_\perp/T)}{q_\perp^2 (q_\perp^2 + m_D^2)}, \quad (73)
$$

where the function $F(q_\perp/T)$ interpolates between the known limits of this quantity [for small $q_\perp/T$ see Eq. (70)] and can be calculated in the approximation $q \gg m_D$. It is then split into gluonic (I_+) and fermionic (I_-) contributions,[10]

$$
F(q_\perp/T) = \frac{1}{\pi^2}(\Xi_+ I_+(q_\perp/T) + \Xi_- I_-(q_\perp/T)). \quad (74)
$$

Following the notation in Ref. [30], we write these contributions to the elastic scattering rate in the limit $p \to \infty$ and $q_\perp \gg m_D$ as

$$
I_\pm\left(\frac{q_\perp}{T}\right) = \frac{\pi^2}{T^3} \int \frac{\mathrm{d}q_z}{2\pi} \int \frac{\mathrm{d}^3 \mathbf{k}}{(2\pi)^3} 2\pi\delta(q_z + |\mathbf{k} - \mathbf{q}| - k)
$$
$$
\times \frac{(k - k_z)^2}{k|\mathbf{k} - \mathbf{q}|} f_\pm(\mathbf{k})[1 \pm f_\pm(\mathbf{k} - \mathbf{q})]. \quad (75)
$$

This formula follows directly from the t-channel matrix element in Table I, i.e., su/t^2, with $t^2 = q_\perp^4$ being scaled out in (73) and $s = -u = 2p(k - k_z)$.

As in (62) we can identify the contributions coming from the f and f^2 parts via

$$
I_\pm(q_\perp/T) = I_\pm^{\mathrm{f}} + I_\pm^{\mathrm{ff}}(q_\perp/T), \quad (76)
$$

---

[10]In principle, we could take Eq. (67) instead and relax the assumption of small momentum transfer, i.e., keep $f_\pm(k)(1 \pm f_\pm(k - \omega))$. However, the strategy employed in Ref. [30] [scaling out this factor $F(q_\perp/T)$ in (73)] allows us to evaluate the expression analytically in the large $q_\perp$ limit, where the matrix element does not need to be screened, and we can use the simpler form su/t^2 instead.

where $I_{\pm}^{\mathrm{f}}$ will turn out to be a constant. To evaluate them, the thermal functions are written as

$$f_{\pm}(p) = \sum_{m=1}^{\infty} (\pm 1)^{m-1} e^{-mp/T}. \qquad (77)$$

This can then be inserted into Eq. (75) to rewrite the equation as a double sum,

$$I_{\pm}^{\mathrm{f}}\left(\frac{q_{\perp}}{T}\right) = \sum_{m=1}^{\infty} (\pm 1)^{m-1} I_{m0}(q_{\perp}/T) \qquad (78)$$

$$I_{\pm}^{\mathrm{ff}}\left(\frac{q_{\perp}}{T}\right) = \sum_{m=1}^{\infty} \sum_{n=1}^{\infty} (\pm 1)^{m+n-1} I_{mn}(q_{\perp}/T) \qquad (79)$$

with

$$I_{mn}\left(\frac{q_{\perp}}{T}\right) = \frac{\pi^2}{T^3} \int \frac{\mathrm{d}q_z}{2\pi} \int \frac{\mathrm{d}^3\mathbf{k}}{(2\pi)^3} 2\pi\delta(q_z + |\mathbf{k} - \mathbf{q}| - k)$$
$$\times \frac{(k - k_z)^2}{k|\mathbf{k} - \mathbf{q}|} e^{-mk/T} e^{-n|\mathbf{k}-\mathbf{q}|/T}. \qquad (80)$$

In [30] $I_{\pm}$ was split in a similar way isolating the $n = 0$ term $I_{\pm}(\infty)$, which is exactly the constant $I_{\pm}^{\mathrm{f}} = I_{\pm}(\infty) = \zeta_{\pm}(3)$. This is a consequence of the fact that for large momentum transfer only the f part contributes, as discussed in Sec. III I.

Performing the remaining integrals over $\mathbf{q}_{\perp}$ as in [30] leads to a $\hat{q}$ formula for large cutoffs $\Lambda_{\perp} \gg T$,

$$\hat{q}^{\mathrm{therm}}(\Lambda_{\perp} \gg T) = C_{\mathrm{R}} \frac{g^4 T^3}{\pi^2} \sum_{\pm} \Xi_{\pm} \mathcal{I}_{\pm}(\Lambda_{\perp}) \qquad (81a)$$

$$\mathcal{I}_{\pm}(\Lambda_{\perp}) = \frac{\zeta_{\pm}(3)}{2\pi} \ln\left(\frac{\Lambda_{\perp}}{m_D}\right) + \Delta\mathcal{I}_{\pm}, \qquad (81b)$$

$$\Delta\mathcal{I}_{\pm} = \frac{\zeta_{\pm}(2) - \zeta_{\pm}(3)}{2\pi} \qquad (81c)$$
$$\times \left[\ln\left(\frac{T}{m_D}\right) + \frac{1}{2} - \gamma_E + \ln 2\right] - \frac{\sigma_{\pm}}{2\pi}$$

$$\sigma_{+} = 0.386043817389949 \qquad (81d)$$

$$\sigma_{-} = 0.011216764589789 \qquad (81e)$$

where γ_E is the Euler–Mascheroni constant.

This formula (81), as opposed to the one for small cutoffs (71), has the (unphysical) feature that the logarithm $\ln T/m_D$ becomes negative for $T \leq m_D$.[11] Normally in perturbation theory one has $T \gg m_D$ so that in the large

—————
[11]In the literature, the small cutoff form (71) is also often written just as logarithm $\ln \Lambda_{\perp}/m_D$ instead of the form we obtain.

cutoff regime $\Lambda_{\perp} \gg T$ the form $\ln \Lambda_{\perp}/m_D$ is not a problem. However, to get an analytical expression that is well-behaved also for larger couplings, we propose to add a constant to the argument of the logarithm, which still preserves the leading-order accuracy at weak coupling. To be explicit, we replace $2\ln x \to \ln(1 + x^2)$ in both logarithms, and we will denote the resulting "improved" analytic expressions for $\hat{q}$ by $\hat{q}_{\mathrm{im}}$. Although the replacement does not change the result at leading order, we find that this choice of regularization significantly improves the agreement with numerical evaluations of (26), as we will discuss in Sec. IV A 3. Moreover, the Bose-enhanced part $\hat{q}_{\mathrm{ff}}$ of (62) comes solely from $\Delta\mathcal{I}_{\pm}$ in (81b). With these replacements in the logarithm, the contribution $\hat{q}_{\mathrm{f}}$ has the same form as for small momentum cutoffs (72a), $\hat{q}_{\mathrm{f}}(\Lambda_{\perp} \ll T) = \hat{q}_{\mathrm{f}}(\Lambda_{\perp} \gg T)$.

With this procedure, the improved version of Eq. (81a) becomes

$$\hat{q}_{\mathrm{im}}^{\mathrm{therm}}(\Lambda_{\perp} \gg T) = \hat{q}_{\mathrm{f}}^{\mathrm{therm}}(\Lambda_{\perp} \ll T) + \hat{q}_{\mathrm{ff,im}}^{\mathrm{therm}} \qquad (82a)$$

with

$$\hat{q}_{\mathrm{ff,im}}^{\mathrm{therm}} = C_{\mathrm{R}} g^4 T^3 \sum_{\pm} \Xi_{\pm} \left\{ \frac{\zeta_{\pm}(2) - \zeta_{\pm}(3)}{4\pi^3} \right.$$
$$\left. \times \left[\ln\left(1 + \frac{T^2}{m_D^2}\right) + 1 - 2\gamma_E + 2\ln 2 \right] - \frac{\sigma_{\pm}}{2\pi^3} \right\}. \qquad (82b)$$

3. Comparison with numerical results

Let us now compare the analytical small and large cutoff limits of $\hat{q}$ given by (71) and (81a) or the improved version (82a) to a numerical evaluation of $\hat{q}$ using (51). For simplicity we consider a purely gluonic plasma, i.e., $n_{\mathrm{f}} = 0$. In particular, we want to study how well these analytic formulae describe the full numerical evaluation of the $\hat{q}$ integral, although being only valid for asymptotic regions of the cutoff $\Lambda_{\perp}$. We also want to compare the expressions using the isotropic HTL matrix element (54) with the simpler screened matrix element (56) and study the impact of the approximation, which is also widely used in studies of the thermalization dynamics [8,72–74,78].

In Fig. 5 we show $\hat{q}$ for various momentum cutoffs $\Lambda_{\perp}$ and different 't Hooft couplings $\lambda = g^2 N_{\mathrm{C}}$. The prefactor $\lambda^2 T^3$ is scaled out in the plots, leaving a nontrivial coupling dependence that enters via the Debye mass m_D in the logarithms originating from the matrix element. The curves show the analytical expressions for small cutoffs [dotted, Eq. (71)], large cutoffs [dash-dotted, Eq. (81a)], and the improved large cutoff version [dashed, (82a)], while the numerical evaluation of $\hat{q}$ is depicted by crosses for the HTL matrix elements (54) and plus signs for the approximated screened ones (56). In the left panel of Fig. 5, we observe that the small cutoff form of $\hat{q}$ accurately agrees with our
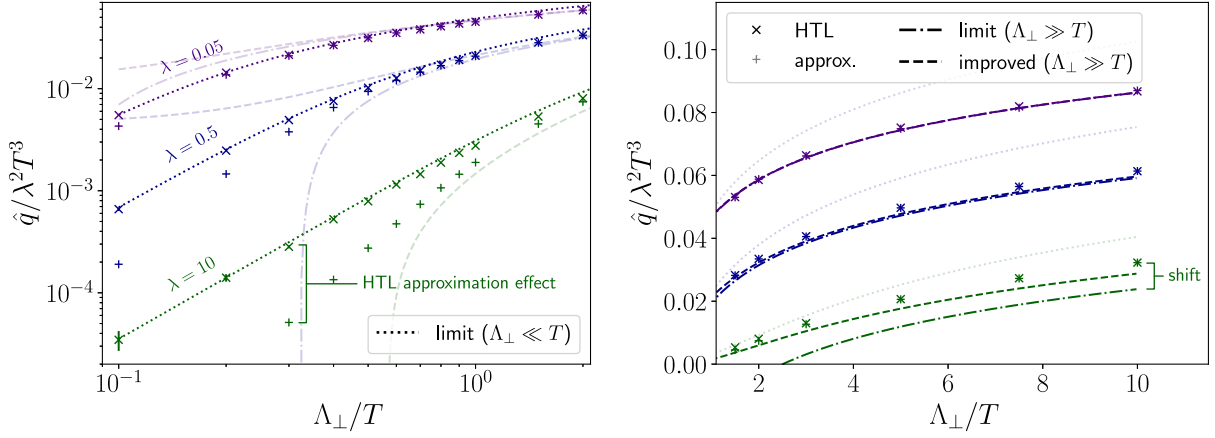
FIG. 5.   The coefficient $\hat{q}$ for a quark jet in thermal equilibrium for different 't Hooft couplings $\lambda = g^2 N_C$ and transverse momentum cutoffs $\Lambda_\perp$, with (left:) small $\Lambda_\perp \lesssim T$ (logarithmically scaled axis), and (right:) large $\Lambda_\perp \gtrsim T$. The dotted curve, labeled "limit ($\Lambda_\perp \ll T$)" shows the analytical limiting expression of (71), the dash-dotted curve "limit ($\Lambda_\perp \gg T$)" illustrates (81a), and "improved ($\Lambda_\perp \gg T$)" denotes (82a). The small +-symbols show our numerical results with the approximated matrix element (56), whereas the ×-symbols show our results with the full HTL matrix element (54). The curves that are not valid in the respective limit are displayed with lighter color but still shown, because (71) is often also used at large $\Lambda_\perp$ as an approximation.

numerical evaluation using the full HTL matrix element in the corresponding region $\Lambda_\perp \ll T$, even for $\Lambda_\perp \to 0$. We note in passing that the frequently employed form of $\hat{q}$ in this limit with the approximation $\ln(1 + \frac{\Lambda_\perp^2}{m_D^2}) \to 2\ln\frac{\Lambda_\perp}{m_D}$ (not shown in the figure) would become negative at too-small cutoffs $\Lambda_\perp \sim m_D$.

In the region $\Lambda_\perp \gg T$ (right panel of Fig. 5), we observe that for small couplings $\lambda \sim 0.05$ both analytical large cutoff expressions agree very well with the numerical values. However, they start to differ when increasing the coupling $\lambda \gtrsim 0.5$. This is denoted as "shift" in Fig. 5. We find that the values from our improved formula (82a) are closer to the numerical values than from the original formula (81a). However, for large couplings $\lambda \sim 10$, our improved analytical expression still seems to underestimate $\hat{q}$, with the difference being a constant.

Turning now to a comparison of the matrix elements, we observe in Fig. 5 that for small values of the coupling $\lambda \sim 0.05$ (left panel) as well as for large cutoffs $\Lambda_\perp \gg T$ (right panel), the results with the screening approximation (56) agree well with the full HTL matrix element (54). However, they start deviating with growing coupling at small cutoffs $\Lambda_\perp \lesssim T$ (left panel). To guide the eye, for $\Lambda_\perp = 0.3T$ we explicitly denote this difference as "HTL approximation effect." For $\Lambda_\perp = T$ and $\lambda = 10$ the deviation between the approximated and the HTL matrix elements is of the order of 30%.

4. Interpolation formula for $\hat{q}$ in thermal equilibrium

We have now observed that the analytical expressions (71) and (81a) describe $\hat{q}$ only in certain limits and Eq. (81a) only holds for small couplings $\lambda \lesssim 0.5$. For phenomenological calculations, a general formula for $\hat{q}$ in thermal

equilibrium may be useful without the need of performing the high-dimensional integral (26) numerically for the required value of the coupling λ and transverse momentum cutoff $\Lambda_\perp$. We thus look for an interpolation formula that reproduces the analytical results in the limits $\Lambda_\perp \ll T$ and for $\Lambda_\perp \gg T$ and agrees with our numerical evaluation.

From (71) and (81a) we know the behavior of $\hat{q}$ for small $\Lambda_\perp \ll T$ and large cutoffs $\Lambda_\perp \gg T$. As discussed before, (81a) differs from the numerical evaluation of $\hat{q}$ by a constant shift for larger values of the coupling $\lambda \gtrsim 0.5$. Our strategy is to find an empirical fit function that smoothly interpolates in between

$$\frac{\hat{q}^{\text{emp}}}{C_R T^3} = \begin{cases} \tilde{c} \ln(1 + \Lambda_\perp^2/m_D^2), & \text{for } \Lambda_\perp \ll T \\ \tilde{a} \ln(\Lambda_\perp/m_D) + \tilde{b}, & \text{for } \Lambda_\perp \gg T. \end{cases} \quad (83)$$

The switching between those two cases will be done using a hyperbole tangent that smears out a step function with width parameter $\tilde{d}$,

$$\theta_{\tilde{d}}(x) = \frac{1 + \tanh(\tilde{d}x)}{2}, \quad (84)$$

which approaches the usual step function for $\tilde{d} \to \infty$.

This leads to the following form for the fit formula

$$\frac{\hat{q}^{\text{emp}}}{C_R T^3} = \tilde{c} \ln\left(1 + \frac{\Lambda_\perp^2}{m_D^2}\right) \theta_{\tilde{d}}\left(\tilde{e} - \ln\frac{\Lambda_\perp}{T}\right)$$

$$+ \left(\tilde{a} \ln\frac{\Lambda_\perp}{m_D} + \tilde{b}\right) \theta_{\tilde{d}}\left(\ln\frac{\Lambda_\perp}{T} - \tilde{e}\right). \quad (85)$$

For the coefficients $\tilde{c}$ and $\tilde{a}$, we use the prefactors of (71) and (81a), which read for a gluonic plasma

TABLE III. Fitted coefficients for the interpolation formula for $\hat{q}$ in Eq. (85). The values were obtained by numerically integrating (51) with measure (52c) and the HTL-screened matrix element (54), then numerically fitting the coefficient $\tilde{b}$ in the region $\Lambda_\perp \gg T$, and finally fitting $\tilde{d}$ and $\tilde{e}$ in the range $0.1T < \Lambda_\perp < 15T$ using SciPy [88].

λ	$\tilde{b}$	$\tilde{d}$	$\tilde{e}$
0.5	0.0011944 ± 0.0000020	4.114 ± 0.013	-0.76919 ± 0.00058
1.0	0.0037772 ± 0.0000062	2.4910 ± 0.0029	-0.24707 ± 0.00041
1.5	0.007379 ± 0.000013	2.0956 ± 0.0018	0.03349 ± 0.00032
2.0	0.011905 ± 0.000021	1.9636 ± 0.0014	0.20498 ± 0.00029
2.5	0.017295 ± 0.000031	1.8987 ± 0.0012	0.32796 ± 0.00028
3.0	0.023563 ± 0.000042	1.8653 ± 0.0010	0.42226 ± 0.00026
3.5	0.030716 ± 0.000054	1.84570 ± 0.00096	0.49864 ± 0.00025
4.0	0.038770 ± 0.000067	1.83331 ± 0.00088	0.56271 ± 0.00024
4.5	0.047761 ± 0.000082	1.82484 ± 0.00080	0.61789 ± 0.00023
5.0	0.057714 ± 0.000099	1.81902 ± 0.00075	0.66626 ± 0.00022
5.5	0.06864 ± 0.00012	1.81444 ± 0.00071	0.70960 ± 0.00021
6.0	0.08061 ± 0.00014	1.81130 ± 0.00069	0.74868 ± 0.00020
6.5	0.09362 ± 0.00015	1.80845 ± 0.00067	0.78441 ± 0.00020
7.0	0.10772 ± 0.00017	1.80584 ± 0.00066	0.81733 ± 0.00020
7.5	0.12296 ± 0.00020	1.80380 ± 0.00065	0.84781 ± 0.00019
8.0	0.13933 ± 0.00022	1.80168 ± 0.00064	0.87635 ± 0.00019
8.5	0.15687 ± 0.00024	1.80026 ± 0.00064	0.90313 ± 0.00019
9.0	0.17562 ± 0.00026	1.79871 ± 0.00064	0.92836 ± 0.00019
9.5	0.19569 ± 0.00029	1.79776 ± 0.00063	0.95195 ± 0.00019
10.0	0.21701 ± 0.00031	1.79691 ± 0.00063	0.97442 ± 0.00019
10.5	0.23960 ± 0.00034	1.79628 ± 0.00063	0.99579 ± 0.00019
11.0	0.26361 ± 0.00036	1.79589 ± 0.00063	1.01605 ± 0.00019
11.5	0.28894 ± 0.00039	1.79532 ± 0.00063	1.03544 ± 0.00019
12.0	0.31570 ± 0.00042	1.79489 ± 0.00063	1.05399 ± 0.00019
12.5	0.34386 ± 0.00045	1.79432 ± 0.00062	1.07188 ± 0.00019
13.0	0.37349 ± 0.00048	1.79405 ± 0.00062	1.08902 ± 0.00019
13.5	0.40461 ± 0.00052	1.79343 ± 0.00062	1.10557 ± 0.00019
14.0	0.43722 ± 0.00054	1.79316 ± 0.00062	1.12149 ± 0.00019
14.5	0.47134 ± 0.00058	1.79241 ± 0.00062	1.13694 ± 0.00019
15.0	0.50704 ± 0.00061	1.79162 ± 0.00061	1.15192 ± 0.00019
15.5	0.54431 ± 0.00066	1.79053 ± 0.00061	1.16651 ± 0.00019
16.0	0.58324 ± 0.00070	1.78988 ± 0.00060	1.18054 ± 0.00020
16.5	0.62381 ± 0.00074	1.78933 ± 0.00060	1.19420 ± 0.00019
17.0	0.66613 ± 0.00078	1.78922 ± 0.00060	1.20734 ± 0.00019
17.5	0.71013 ± 0.00081	1.78864 ± 0.00059	1.22017 ± 0.00019
18.0	0.75590 ± 0.00085	1.78805 ± 0.00059	1.23280 ± 0.00019
18.5	0.80337 ± 0.00090	1.78734 ± 0.00058	1.24516 ± 0.00019
19.0	0.85257 ± 0.00094	1.78699 ± 0.00058	1.25721 ± 0.00019
19.5	0.90367 ± 0.00099	1.78674 ± 0.00058	1.26879 ± 0.00019
20.0	0.9565 ± 0.0010	1.78563 ± 0.00058	1.28029 ± 0.00019

$$\tilde{c} = \frac{\lambda^2}{12\pi N_C}, \qquad \tilde{a} = \frac{\lambda^2 \zeta(3)}{\pi^3 N_C}. \qquad (86)$$

This leaves only three fit parameters: The constant $\tilde{b}$ encodes the linear shift in the large $\Lambda_\perp/T$ region, while $\tilde{d}$ and $\tilde{e}$ describe the width and position of the switching between the two limiting cases in (83). We first fit the coefficient $\tilde{b}$, such that it correctly reproduces $\hat{q} \simeq \tilde{a} \ln \Lambda_\perp/T + \tilde{b}$ in the large $\Lambda_\perp/T$ region. We then determine the coefficients $\tilde{d}$ and $\tilde{e}$ by fitting them to our numerical data.

Our results for the remaining fit parameters in Eq. (85) are listed in Table III for the couplings $\lambda = 0.5$–20. The resulting $\hat{q}$ are shown in Fig. 6 as continuous lines. For comparison, we have included the numerically evaluated values as crosses, and the limiting expressions for hard and soft cutoffs, Eqs. (71) and (81a), respectively, as dashed and dotted lines. Consistently with the construction of the fit formula, its values are seen to agree well with our numerically evaluated $\hat{q}$ in the left panel of Fig. 6 and in the inset
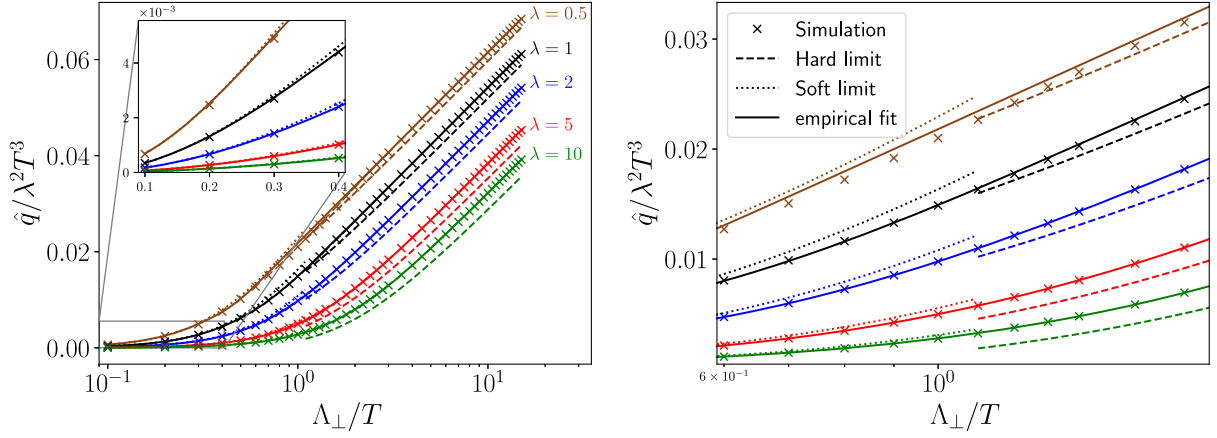
FIG. 6. Left: the interpolation formula (85) for $\hat{q}$ with the fitted coefficients listed in Table III is shown as continuous lines for different couplings λ. The numerical results from (26) are shown as crosses, the limiting expressions for soft (71) and hard cutoffs (81a) as dotted and dashed curves. The inset shows the behavior at small momentum cutoffs. Right: focus on the interpolation region $\Lambda_\perp \sim T$. For $\lambda \geq 1$ we see very good agreement with the numerical results.

showing the small cutoff behavior at $\Lambda_\perp \ll T$. The right panel of Fig. 6 shows the interpolation region $\Lambda_\perp \sim T$. We find a very good agreement with our numerics for $\lambda \geq 1$, while for smaller couplings $\lambda \lesssim 0.5$ deviations grow in this region. Note that our fit formula provides a smooth interpolating expression for $\hat{q}$ with improved accuracy in this region as compared to the previous limiting forms.

Our expression (85) together with the coefficients in Table III can thus be used to obtain $\hat{q}$ in thermal equilibrium for any transverse momentum cutoff $\Lambda_\perp$ and the listed couplings λ in the weak coupling leading-order pQCD limit.

B. Toy models for bottom-up thermalization

Our current weak coupling understanding of how the nonequilibrium quark-gluon plasma created in heavy-ion collisions reaches local thermal equilibrium is based on the bottom-up thermalization scenario of Ref. [1]. Strictly speaking, it is only valid in the extremely weak coupling limit, where soft gluon radiation and the LPM effect play an important role and need to be included in the analysis. However, we believe that this picture can also shed light on what happens at intermediate couplings at least at a qualitative level. It consists of several stages. The first stage is characterized by a large anisotropy in momentum space as well as an overoccupation of hard gluon modes. Due to the longitudinal expansion along the beam axis, the anisotropy further increases. As the occupancy of these hard gluons drops below unity, we enter the second stage, in which the momentum anisotropy remains roughly constant, while producing soft gluons through branching, which form a thermal bath. A significant amount of the total energy is still carried by the remaining small number of hard gluons, which, in the third stage, lose energy through multiple hard branchings, until equilibrium is reached.

As toy models for this thermalization process, we consider first an effectively two-dimensional distribution in Sec. IV B 1. We then compute $\hat{q}$ analytically in Sec. IV B 2 using an isotropic scaled thermal distribution, which can be understood as modeling key features of the over- and underoccupied bottom-up stages.

1. Effectively two-dimensional distribution

As a model for the large anisotropies encountered at early times in the bottom-up thermalization scenario, let us calculate $\hat{q}$ in a system brought to its extreme anisotropic limit with vanishing k_z momentum,

$$f(\mathbf{k}) = B(k_x, k_y)\delta(k_z/Q), \tag{87}$$

where B is an arbitrary function of k_x and k_y, and Q is an energy scale. Due to its vanishing momentum in beam direction $k_z = 0$, such a state is similar in spirit to the glasma, which is often studied within classical-statistical simulations due to its large field values [14–17].

Let us focus on the *Bose-enhanced* part $\hat{q}_{\text{ff}}$ in kinetic theory, which agrees with $\hat{q}$ in a classical-statistical framework since there is no $\hat{q}_{\text{f}}$ contribution in the classical field limit. By inserting the extremely anisotropic distribution (87) into the $\hat{q}$ integral (26) with the measure (52a), one immediately finds

$$\hat{q}_{\text{ff}}^{zz} = 0, \tag{88}$$

due to its proportionality to $\int (q^z)^2 \delta(k_z)\delta(k_z')$. Note that this is true regardless of the precise form of the matrix element or screening prescription. Thus, a purely two-dimensional momentum distribution remains two dimensional in the classical field limit of kinetic theory, if only elastic processes are considered.

We can also consider a special case of (87) that we can solve analytically: if additionally all particles have a specific momentum $\tilde{k}$,

$$f(\mathbf{k}) = A\delta\left(\frac{k_x^2 + k_y^2 - \tilde{k}^2}{Q^2}\right)\delta(k_z/Q). \qquad (89)$$

With a jet perpendicular to the beam direction and using the approximated gluonic matrix element (56), one obtains (see Appendix E 1 for details)

$$\hat{q}_{\text{ff}}^{zz} = 0 \qquad (90)$$

$$\hat{q}_{\text{ff}}^{yy} = \frac{d_A C_A^2 A^2 g^4}{2^7 \pi^5 d_R \tilde{k}^3} Q^6 \left\{ 4\tilde{k}^2\left(\frac{2}{\xi^2 m_D^2} - \frac{1}{4\tilde{k}^2 + \xi^2 m_D^2}\right) \right.$$
$$\left. + \ln\frac{\xi^2 m_D^2}{4\tilde{k}^2 + \xi^2 m_D^2}\right\}, \qquad (91)$$

where $m_D^2 = A\frac{g^2 Q^3}{\pi^2 \tilde{k}}$ according to (8).

Indeed we have observed in Ref. [20] that in the overoccupied and anisotropic earliest stage of bottom-up thermalization one has $\hat{q}^{zz} < \hat{q}^{yy}$ and that this is due to $\hat{q}_{\text{ff}}^{zz} < \hat{q}_{\text{ff}}^{yy}$, which is consistent with the simple toy model presented here. In Ref. [20], we then showed that $\hat{q}_{\text{ff}}^{yy}$ quickly becomes similar to $\hat{q}_{\text{ff}}^{zz}$ and that both become much smaller than $\hat{q}_{\text{f}}$.

2. Scaled thermal distribution

Let us now study another aspect encountered during bottom-up thermalization: over- and underoccupied systems. For simplicity, we use an isotropic toy model and consider a scaled thermal distribution, i.e., we scale the amplitude of the thermal distribution (63) with $N_\pm$. Here N_+ denotes the scaling parameter of the Bose–Einstein distribution and N_- the scaling parameter of the Fermi–Dirac distribution,

$$f_\pm(k; T) = \frac{N_\pm}{\exp(k/T) \mp 1}. \qquad (92)$$

This allows us to easily generalize the results obtained in Sec. IV A for $\hat{q}$ in a thermal medium, and we start with $\hat{q}$ given by Eq. (68). Splitting the f and ff contributions and using the integrals (69) over thermal distributions, we obtain for small cutoff

$$\hat{q}(\Lambda_\perp \ll T, N_\pm) = \frac{g^4 T^3 C_R}{24\pi^3} \ln\left(1 + \frac{\Lambda_\perp^2}{m_D^2}\right)$$
$$\times (\pi^2(2N_C(N_+)^2 + n_f(N_-)^2)$$
$$+ \zeta(3)[9n_f N_-(1 - N_-)$$
$$- 12N_C N_+(N_+ - 1)]), \qquad (93)$$

which generalizes the equilibrium ($N_\pm = 1$) result in Eq. (71). Similarly, we can generalize the large cutoff formula (81a) to

$$\hat{q}(\Lambda_\perp \gg T, N_\pm) = C_R \frac{g^4 T^3}{\pi^2} \sum_\pm \Xi_\pm \mathcal{I}_\pm(\Lambda_\perp, N_\pm) \quad (94a)$$

$$\mathcal{I}_\pm(\Lambda_\perp, N_\pm) = \frac{N_\pm \zeta_\pm(3)}{2\pi} \ln\left(\frac{\Lambda_\perp}{m_D}\right) + (N_\pm)^2 \Delta\mathcal{I}_\pm, \quad (94b)$$

with $\Delta\mathcal{I}_\pm$ given by Eq. (81c), which is entirely determining $\hat{q}_{\text{ff}}$,

$$\hat{q}_{\text{ff}}(\Lambda_\perp \gg T, N_\pm) = C_R \frac{g^4 T^3}{\pi^2} \sum_\pm (N_\pm)^2 \Xi_\pm \Delta\mathcal{I}_\pm. \qquad (94c)$$

Furthermore, similarly to our discussion for the thermal result in Sec. IV A 2, by replacing $2\ln(\Lambda_\perp/m_D) \to \ln(1 + (\Lambda_\perp/m_D)^2)$ in (94b), we obtain an "improved" formula valid for large cutoffs that is finite even at small $\Lambda_\perp$ and generalizes Eq. (82a). Then we can again split off the Bose-enhanced contribution as in (62), $\hat{q} = \hat{q}_{\text{f}} + \hat{q}_{\text{ff}}$, and realize that $\hat{q}_{\text{f}}(\Lambda_\perp)$ has the same form for small and large cutoffs,

$$\hat{q}_{\text{f}}(\Lambda_\perp, N_\pm) = \zeta(3)(12N_+ N_C + 9n_f N_-)C_L(\Lambda_\perp), \qquad (95a)$$

with, as before, $C_L(\Lambda_\perp) = \frac{g^4 T^3 C_R}{24\pi^3}\ln\left(1 + \frac{\Lambda_\perp^2}{m_D^2}\right)$. In contrast, the Bose-enhanced terms differ

$$\hat{q}_{\text{ff}}(\Lambda_\perp \ll T, N_\pm) = [2N_C(N_+)^2(\pi^2 - 6\zeta(3))$$
$$+ n_f(N_-)^2(\pi^2 - 9\zeta(3))]C_L(\Lambda_\perp) \quad (95b)$$

$$\hat{q}_{\text{ff,im}}(\Lambda_\perp \gg T, N_\pm) = C_R g^4 T^3 \sum_\pm \Xi_\pm (N_\pm)^2$$
$$\times \left\{\frac{\zeta_\pm(2) - \zeta_\pm(3)}{4\pi^3}\left[\ln\left(1 + \frac{T^2}{m_D^2}\right)\right.\right.$$
$$\left.\left. + 1 - 2\gamma_E + 2\ln 2\right] - \frac{\sigma_\pm}{2\pi^3}\right\}. \quad (95c)$$

The Debye mass entering these expressions for the scaled thermal distributions is given by [see Eq. (8)]

$$m_D^2 = \frac{g^2 T^2}{3}\left(N_+ N_C + \frac{N_- n_f}{2}\right). \qquad (96)$$

Thus, m_D scales with $\sqrt{\lambda N_\pm}$. For large occupancies N_+, this may pose a problem for the validity of perturbation theory that assumes $m_D \ll T$ and that our arguments and the derivations in [30] were based on. The occupation of fermions N_- cannot become large due to Pauli blocking. We can estimate the breakdown scale by requiring $m_D \ll T$, which leads to
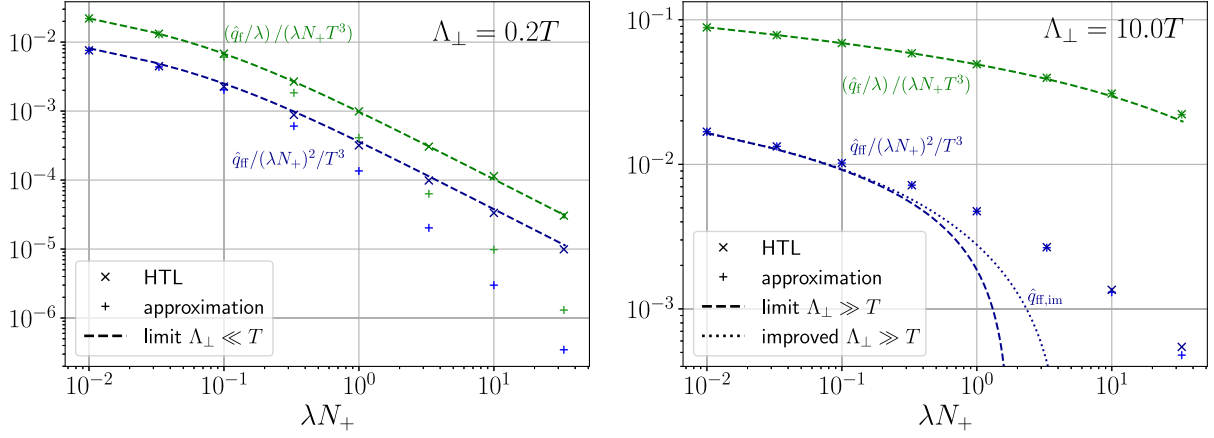
FIG. 7.   The individual components $\hat{q}_\text{f}$ (green) and $\hat{q}_\text{ff}$ (blue) as defined in (62) and rescaled according to their parametric estimates in (99) as functions of their only argument λN_+ for $\Lambda_\perp/T = 0.2$ (left) and $\Lambda_\perp/T = 10$ (right). The numerical HTL values from our calculation are shown with ×-symbols, and the numerical values using the ξ-approximated matrix element (45) are labeled "approximation" and shown by +-symbols. Our analytic estimate for $\hat{q}_\text{f}$, Eq. (95a), and for $\hat{q}_\text{ff}$, Eq. (95b) for $\Lambda_\perp \ll T$, and (94c) for $\Lambda_\perp \gg T$. In the left panel, we show the small cutoff form (95b) for $\hat{q}_\text{ff}$ and Eq. (95a) for $\hat{q}_\text{f}$ labeled as "$\Lambda_\perp \ll T$." In the right panel, we show both high-cutoff expressions (95a) for $\hat{q}_\text{f}$ and (94c) for $\hat{q}_\text{ff}$ labeled "limit $\Lambda_\perp \gg T$" and its improved version (95c) labeled as "improved $\Lambda_\perp \gg T$."

$$N_+ \ll \frac{1}{N_\text{C}}\left(\frac{3}{g^2} - \frac{N_- n_\text{f}}{2}\right). \tag{97}$$

This is consistent with the usual limitations of perturbation theory, which breaks down at nonperturbatively large occupation numbers $f \gtrsim 1/g^2$.

Let us now assess the expressions derived above by comparing them to the numerical evaluation of $\hat{q}$ using Eq. (26), before applying the formulae to initial stages in heavy-ion collisions. We start with $\hat{q}_\text{f}/\lambda$ and $\hat{q}_\text{ff}$ in Eq. (95), which are functions of the combination λN_+ (we refer to Appendix E 2 for details), i.e.,

$$\hat{q}(\Lambda_\perp, N_+, \lambda) = \lambda\left(\frac{\hat{q}_\text{f}}{\lambda}\right)(\Lambda_\perp, \lambda N_+) + \hat{q}_\text{ff}(\Lambda_\perp, \lambda N_+). \tag{98}$$

These contributions are plotted in Fig. 7 for small (left) and large (right) cutoffs $\Lambda_\perp = 0.2T$ and $10T$, respectively, divided by the prefactor

$$\hat{q}_\text{f} \sim \lambda(\lambda N_+)T^3, \qquad \hat{q}_\text{ff} \sim (\lambda N_+)^2 T^3. \tag{99}$$

We observe that their values deviate significantly from the simple estimates in Eq. (99). This is a consequence of screening effects and the scaling of the Debye mass. In particular, one finds for sufficiently small cutoffs $\Lambda_\perp \lesssim m_D, T$ and large occupancies that

$$\frac{\hat{q}_\text{f}}{\lambda^2 N_+ T^3} \sim \frac{\hat{q}_\text{ff}}{\lambda^2 N_+^2 T^3} \sim \frac{\Lambda_\perp^2}{m_D^2} \sim (\lambda N_+)^{-1}, \tag{100}$$

which is visible in the left panel of Fig. 7 for sufficiently large λN_+. Note that for a sufficiently large $\lambda N_+ \gg 1$ the

effective kinetic theory description used here ceases to be valid. Similarly to the equilibrium case discussed in Sec. IV A and particularly in Fig. 5, the expression for small cutoffs (93) nicely agrees with the numerical values in the small cutoff asymptotic region, plotted in the left panel of Fig. 7. In the right panel, for large cutoffs, we observe that our analytical form for $\hat{q}_\text{f}$ in Eq. (95a) remains a very good description coinciding with our numerical values, whereas the analytical estimate for $\hat{q}_\text{ff}$ in Eq. (94c) [and its improvement Eq. (95c)] ceases to describe the data for nonperturbatively large occupancies $\lambda N_+ \gtrsim 1$. This is expected from the condition (97), and we see sizable deviations already at $\lambda N_+ \gtrsim 0.1$.

The full HTL screening and the approximation with a constant ξm_D regulator (56) nicely agree with each other at large cutoffs for the whole λN_+ range despite the aforementioned limitations concerning $\hat{q}_\text{ff}$. On the other hand, for small cutoffs (left panel), the ξm_D screening approximation shows large deviations from the full HTL screening, albeit in the large λN_+ region that should be taken with caution, as discussed above. The resemblance to the thermal case here is of course no coincidence since by setting $N_+ = 1$ we recover the thermal results.

Recombining the contributions from $\hat{q}_\text{f}$ and $\hat{q}_\text{ff}$, we show $\hat{q}$ in Fig. 8 for the couplings $\lambda = 0.5$, 1, 2, 5, and 10 as functions of the occupancy N_+, for the small cutoff $\Lambda_\perp/T = 0.2$ in the left panel and the large cutoff $\Lambda_\perp/T = 10$ in the right panel. The values are shown scaled by the effective temperature T_ε that represents the temperature of a thermal system with the same energy density, $\varepsilon = \nu_g \pi^2 T_\varepsilon^4/30$ [cf., (9a)], and thus
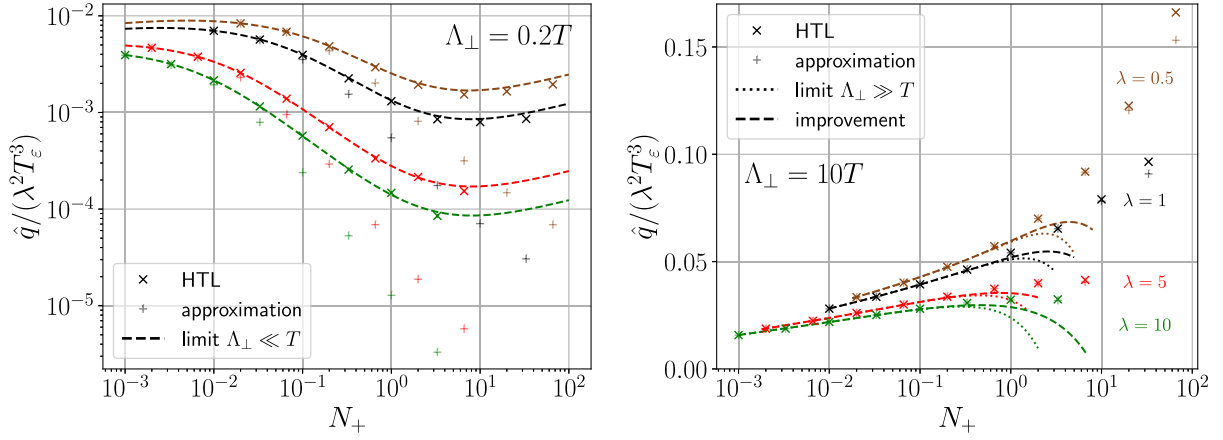
$$T_\varepsilon = (N_+)^{1/4} T. \tag{101}$$

FIG. 8. The momentum broadening coefficient $\hat{q}$ for a scaled thermal distribution (92) as a function of N_+ for different values of λ for $\Lambda_\perp/T = 0.2$ (left) and $\Lambda_\perp/T = 10$ (right). As in Fig. 7, the numerical HTL values from our calculation are shown with ×-symbols, and the values using the ξ-approximated matrix element (45) are shown as +-symbols. In the left panel, we show the small cutoff form (93) labeled as "$\Lambda_\perp \ll T$." In the right panel, we show both the high-cutoff expression Eq. (94a) labeled as "limit $\Lambda_\perp \gg T$" and the improved version obtained by summing Eqs. (95a) and (95c) labeled as "improvement."

For comparison, we plot the analytic predictions for small (93) and large cutoffs (94) as well as their improved expression (95). Similarly as for $\hat{q}_f$ and $\hat{q}_{ff}$, we observe for $\hat{q}$ in Fig. 8 that the small cutoff expression agrees well with our (HTL-)screened data points while the large cutoff expressions describe the data points until $N_+ \lesssim 1/\lambda$. Moreover, the improved formula for large cutoffs increases the validity of the analytic result only to slightly larger occupancy N_+. This plot emphasizes the importance of screening effects that prevent the naïve scaling with N_+ or N_+^2. We therefore have to be cautious when we want to use such analytic expressions to describe overoccupied systems with typical occupancies $N_+ \sim 1/\lambda$. Instead, transport coefficients in such systems can be studied using classical statistical lattice simulations [14,15,18,58]. In particular, it has been shown [58] that nonperturbative corrections can be substantial. Interestingly, as visible in Fig. 8, increasing the occupancy N_+ does not appear as drastically increasing the value of the jet quenching parameter $\hat{q}$. In particular, for small cutoff $\Lambda_\perp/T = 0.2$ visible in the left panel, we observe that the scaled $\hat{q}$ in fact decreases with increasing occupancy. Even for large cutoffs (right panel), increasing the occupancy by several orders of magnitude only leads to a slight increase in the jet quenching parameter. This behavior is due to a combination of two effects. The first effect is that the increasing occupation number also increases the Debye mass m_D. Thus one conclusion of our analysis is that a detailed understanding of screening effects is particularly important for a quantitative analysis of $\hat{q}$. The second effect is that we are dividing the value of $\hat{q}$ with the third power of the effective temperature, which increases with the occupancy $T_\varepsilon \sim N_+^{1/4}$ when the hard momentum scale T is kept fixed.

In Fig. 9 we provide an overview of the numerical values of $\hat{q}$ for the phenomenologically relevant coupling $\lambda = 10$

in heavy-ion collisions. Different values of the cutoff $\Lambda_\perp$ are color coded and written in the circle markers in the figure. We observe the same behavior at small and large cutoffs that we have found in Fig. 8. This involves a fast (power-law) decrease with growing occupancy N_+ at small cutoffs as $\hat{q}/(\lambda^2 T_\varepsilon^3) \sim N_+^{-3/4}$, and a slow growth at high cutoffs. We additionally see how $\hat{q}$ interpolates smoothly between these two behaviors at small and large cutoffs. From a physical point of view, this confirms the observation that for small cutoffs, jet quenching in an overoccupied (isotropic) system similar to a scaled thermal distribution may be strongly suppressed. However, we repeat our note of caution below (100) that these parameters may lie
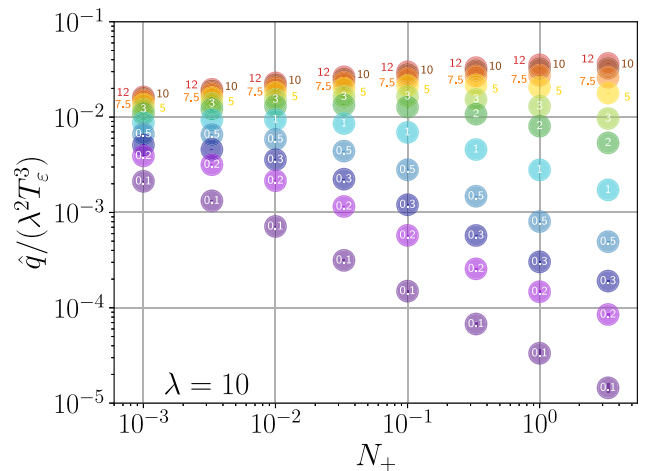

FIG. 9. Numerical values of $\hat{q}$ for a scaled Bose–Einstein distribution (92) as a function of its amplitude N_+ for different momentum cutoffs $\Lambda_\perp$ (numbers in circle markers) and coupling $\lambda = 10$.
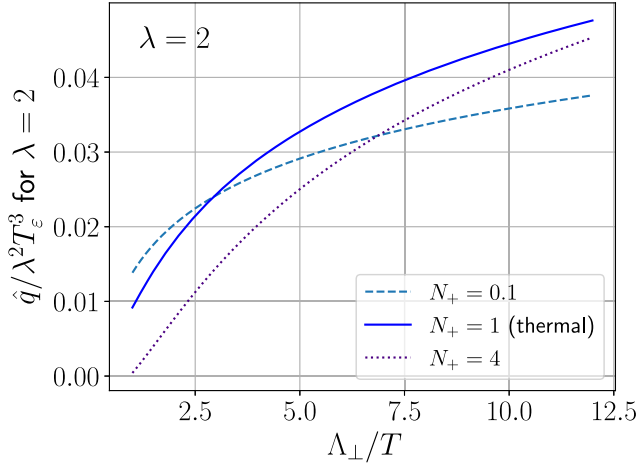
FIG. 10. Jet momentum broadening parameter $\hat{q}$ for a scaled thermal distribution with various scaling coefficients N_+ and coupling $\lambda = 2$ as a function of the transverse momentum cutoff $\Lambda_\perp$.

beyond the range of applicability of our original integral formula for $\hat{q}$ (26).

Let us finally apply our analytical results and conclusions of this section to the initial stages in heavy-ion collisions, and in particular to the bottom-up thermalization scenario, whose over- and underoccupied stages we wish to qualitatively understand using the scaled thermal distribution as a toy model. Although we have reported recently in Refs. [20,60] about numerical kinetic theory simulations during bottom-up thermalization where we have studied transport coefficients including the jet quenching parameter $\hat{q}$, in the present work, we are able to provide more insight into its preequilibrium features by using our analytical expressions.

In Fig. 10 we compare $\hat{q}/(\lambda^2 T_\varepsilon^3)$ for scaled thermal distributions representing an underoccupied system ($N_+ = 0.1$), thermal equilibrium ($N_+ = 1$) and overoccupancy ($N_+ = 4$), and plot its value as a function of the momentum cutoff $\Lambda_\perp$ in the large $\Lambda_\perp$ region [Eq. (95)]. We find that for underoccupied systems and small cutoff, $\hat{q}$ is larger than its thermal value, whereas for large cutoffs this is reversed. This confirms our numerical simulation results of bottom-up thermalization in Ref. [20]. One implication is that for relatively small cutoffs $\Lambda_\perp \gtrsim T$, which are comparable to the momentum carried by gluons in the plasma, collisional momentum broadening is more efficient in underoccupied plasmas than in thermal equilibrium at the same energy density. While our analytical result for large cutoffs but small occupancies agrees with the numerical evaluation of $\hat{q}$ in (26), this does not imply that jets experience less broadening than in thermal equilibrium. In fact, as explained in Ref. [20] and discussed in Sec. III J, the momentum cutoff should be rather taken as a function of the jet energy and plasma temperature. It turns out that for realistic models of the momentum cutoff like (60) and (61),

$\hat{q}$ exceeds the thermal value for the same energy density even in the underoccupied phases of bottom up.

The main difference between the scaled thermal distributions and Ref. [20] is that in the latter the system is characterized by a large momentum anisotropy, while our scaled thermal distribution is isotropic. For overoccupied systems similar to those encountered initially in the bottom-up scenario, our analytical study using the scaled thermal distribution suggests that $\hat{q}$ is always smaller than its thermal value. However, in [20] we do not find this specific ordering during the early overoccupied stage in our numerical simulations. We take this as a numerical indication that a scaled thermal distribution does not describe this stage accurately.

In the underoccupied phase, on the other hand, we see an enhancement of $\hat{q}$ for small $\Lambda_\perp$ and a suppression at large $\Lambda_\perp$, compared to a thermal system at the same energy density. This is consistent with our observation in Ref. [20] and indicates that using a scaled thermal distribution as a model of the underoccupied stage of bottom up is a better approximation.

V. SUMMARY AND CONCLUSIONS

In this paper we have generalized the calculation of the jet quenching parameter $\hat{q}$ to an anisotropic nonequilibrium plasma, using QCD effective kinetic theory. We describe in detail the treatment of the phase space needed for the calculation and implement the integration numerically in a kinetic theory simulation. This generalizes the usual form of $\hat{q}$ to a tensor that encodes momentum broadening in different directions relative to the jet, which is important for nonequilibrium systems. In Ref. [20] we used the expressions obtained here to study $\hat{q}$ during the initial stages of heavy-ion collisions.

We use an isotropic hard thermal loop (HTL) screening prescription as well as a simple approximation thereof and provide a formula for finite jet energy and arbitrary jet angle with respect to the beam axis. Additionally, we provide expressions in the limit of infinite jet momentum, in which a transverse momentum cutoff needs to be introduced to render $\hat{q}$ finite. As a part of the derivation, we have investigated different screening prescriptions for t-channel gluon exchange. We give an explicit expression for the HTL form of the matrix element entering $\hat{q}$ and compare this full HTL matrix element to a simple screening prescription that is typically employed in EKT simulations. In particular, we find that matching the simple screening prescription to HTL in the case of transverse momentum broadening requires regulating the gluon propagator by a scale $(\xi m_D)^2$ with $\xi = e^{1/3}/2$. This value is different than the value used in previous studies for the elastic scattering kernel. Even with this matching value of ξ, for small momentum cutoffs $\Lambda_\perp$ there are in some cases sizeable deviations up to 30% in the values of $\hat{q}$ in thermal systems.

We also study in detail the leading logarithmic behavior of the scattering term in the Boltzmann equation in the forward scattering limit. We show explicitly how a logarithmic divergence in p arises from the integral of the scattering matrix element at large p. Due to this divergence, in eikonal limit $p \to \infty$ a momentum transfer cutoff $\Lambda_\perp > q_\perp$ must be introduced. We show how, conversely, $\hat{q}$ at $p \to \infty$ depends logarithmically on the cutoff, $\hat{q} = a \ln \Lambda_\perp + b$, and we find a simple expression for the coefficient a.

We then move to study the value of $\hat{q}$ in specific cases. We first recover known results in limiting values for the cutoff $\Lambda_\perp$ in a thermal distribution. By evaluating $\hat{q}$ numerically in a thermal distribution for arbitrary values of $\Lambda_\perp$, we provide an explicit interpolation formula in Eq. (85) with fitted coefficients listed in (86) and Table III, that smoothly interpolates between analytical results at small and large momentum cutoffs. Our formula provides an accurate approximation of $\hat{q}$ in thermal equilibrium for all cutoffs $\Lambda_\perp$ and various couplings $0.5 \le \lambda \le 20$.

As a background for our study of bottom-up thermalization in Ref. [20], we then study toy models for aspects of the thermalization process. We first confirm that for a maximally anisotropic plasma with no longitudinal momentum, only terms linear in the distribution function can contribute to $\hat{q}^{zz}$. This feature is clearly visible in the simulation of Ref. [20], where $\hat{q}^{zz}$ becomes larger than $\hat{q}^{yy}$ when the system transitions from the overoccupied to the underoccupied regime. We then calculate $\hat{q}$ analytically for a scaled thermal distribution to obtain improved insight into the under- and overoccupied plasma dynamics during the initial stages. Generalizing previous results in thermal equilibrium, we derive and discuss analytic formulas of the components entering $\hat{q}$ as functions of the bosonic and fermionic scaling occupancies $N_\pm$. We discuss their range of validity and compare to our numerically computed $\hat{q}$. We observe that at large cutoffs, the ratio $\hat{q}/(\lambda^2 T_\varepsilon^2)$, with a Landau-matched temperature T_ε, grows slowly with N_+. At small cutoffs, the ratio $\hat{q}/(\lambda^2 T_\varepsilon^2)$ decreases rapidly with N_+. This implies that for underoccupied systems $N_+ \ll 1$ the value of $\hat{q}$ exceeds the value of a thermal system with the same energy density at small cutoffs, and is smaller at large cutoffs. This provides further insight into the calculation during bottom-up thermalization in Ref. [20].

Our computation of $\hat{q}$ with full isotropic HTL self-energies goes beyond typical screening approximations with a constant mass regulator ξm_D usually employed in EKT simulations and is leading-order accurate for isotropic systems. However, we note that our screening formulation does not capture the dynamics of plasma instabilities consistently, since these have not been incorporated into the EKT implementations yet. There have been recent efforts to tackle the problem of anisotropic screening [49,89,90], and we leave the task of including it into $\hat{q}$ to future studies.

Although this paper focuses on transverse momentum broadening, the integral expression (26) can also be used to describe longitudinal momentum broadening, $\hat{q}^L = \hat{q}^{33}$ and collisional energy loss, which we plan to study. In future work, we also want to investigate the differences between the finite p expressions of $\hat{q}$ and the $p \to \infty$ limit with cutoff $\Lambda_\perp$. Our expressions have already been used in [20] to study the initial stages in heavy-ion collisions. Together with the present work, this paves the way for further kinetic theory studies of jet quenching in anisotropic and preequilibrium systems.

APPENDIX A: BOUNDARIES OF THE PHASE-SPACE INTEGRATION

Here we give a detailed derivation of the boundaries for the phase-space integrals of $\hat{q}$. We start with (14), which we can rewrite using four-dimensional integrals,

$$
\hat{q}^{ij} = \frac{1}{2p\nu_a} \sum_{bcd} \int \frac{\mathrm{d}^4K \mathrm{d}^4P' \mathrm{d}^4K'}{(2\pi)^5} q_\perp^i q_\perp^j \delta^{(4)}(P + K - P' - K')|\mathcal{M}^{ab}_{cd}(\mathbf{p},\mathbf{k};\mathbf{p}',\mathbf{k}')|^2
$$

$$
\times \delta(K^2)\delta(P'^2)\delta(K'^2)\theta(K^0)\theta(P'^0)\theta(K'^0)f^b(\mathbf{k})[1 \pm f^d(\mathbf{k}')]\theta(p' - k'). \tag{A1}
$$

We eliminate the K' integration using the energy-momentum conserving delta function, but will still write K' or $\mathbf{k}'$ as a short notation for $P + K - P'$ or $\mathbf{p} + \mathbf{k} - \mathbf{p}'$. We will proceed similarly as in [79]. We introduce $Q^\mu = (\omega, \mathbf{q})^\mu$ as in (16) via

$$Q = P' - P \Leftrightarrow \mathbf{q} = \mathbf{p}' - \mathbf{p} = \mathbf{k} - \mathbf{k}'$$
$$\omega = p' - p = k - k'. \tag{A2}$$

Note that unlike the external momenta P, P', K, K', the momentum transfer Q is not lightlike, i.e., $Q^2 = \mathbf{q}^2 - \omega^2 \geq 0$. Then we have $\mathrm{d}^4 K \mathrm{d}^4 P' = \mathrm{d}^4 K \mathrm{d}^4 Q$ and thus

$$\hat{q}^{ij} = \frac{1}{2p\nu_a} \sum_{bcd} \int \frac{\mathrm{d}^4 K \mathrm{d}^4 Q}{(2\pi)^5} q_\perp^i q_\perp^j |\mathcal{M}_{cd}^{ab}(\mathbf{p}, \mathbf{k}; \mathbf{p}', \mathbf{k}')|^2$$
$$\times \theta(p' - k')\theta(K^0)\theta(P^0 + \omega)\theta(K^0 - \omega)$$
$$\times \delta(K^2)\delta((P + Q)^2)\delta((K - Q)^2)$$
$$\times f^b(\mathbf{k})[1 \pm f^d(\mathbf{k}')]. \tag{A3}$$

Using $P^2 = K^2 = 0$, $P \cdot Q = -p\omega + pq\cos\theta_{pq}$, and $K \cdot Q = -k\omega + kq\cos\theta_{kq}$, we can rewrite the last two delta functions as

$$\delta((P + Q)^2)\delta((K - Q)^2)$$
$$= \frac{1}{4pkq^2}\delta\left(\cos\theta_{pq} - \frac{\omega}{q} - \frac{\omega^2 - q^2}{2pq}\right)$$
$$\times \delta\left(\cos\theta_{kq} - \frac{\omega}{q} + \frac{\omega^2 - q^2}{2kq}\right). \tag{A4}$$

Because of this expression, it is beneficial to perform the $\mathbf{q}$ integral in a coordinate frame in which θ_{pq} is its polar angle and the $\mathbf{k}$ integral in a frame in which θ_{kq} is its polar angle. This is one of the reasons for introducing the different coordinate systems in Sec. III B. The delta function only contributes if its argument becomes zero, which restricts the integration region to the one indicated in Eq. (15),

$$|\omega| < q, \qquad p > \frac{q - \omega}{2}, \qquad k > \frac{q + \omega}{2}. \tag{A5}$$

Subsequently performing the K^0 integral yields

$$\hat{q}^{ij} = \frac{1}{16p^2\nu_a} \sum_{bcd} \int \frac{\mathrm{d}^3\mathbf{k}\mathrm{d}^3\mathbf{q}\mathrm{d}\omega}{(2\pi)^5 q^2 k^2} q_\perp^i q_\perp^j |\mathcal{M}_{cd}^{ab}(\mathbf{p}, \mathbf{k}; \mathbf{p}', \mathbf{k}')|^2$$
$$\times \theta(p' - k')\theta\left(p - \frac{q - \omega}{2}\right)\theta\left(k - \frac{q + \omega}{2}\right)\theta(q - |\omega|)$$
$$\times \delta\left(\cos\theta_{pq} - \frac{\omega}{q} - \frac{\omega^2 - q^2}{2pq}\right)\delta\left(\cos\theta_{kq} - \frac{\omega}{q} + \frac{\omega^2 - q^2}{2kq}\right)$$
$$\times f^b(\mathbf{k})[1 \pm f^d(\mathbf{k} - \mathbf{q})]. \tag{A6}$$

The $\mathbf{k}$ and $\mathbf{q}$ integrals are now performed in spherical coordinates, where the polar angle integral is performed using the delta function and the azimuthal and radial integrals remain. For the radial integrals there are different equivalent possibilities that implement the required conditions:

$$\int_0^\infty \mathrm{d}q \int_{\max(-q, q-2p, \frac{1}{3}(q-2p))}^q \mathrm{d}\omega \int_{\frac{q+\omega}{2}}^{p+2\omega} \mathrm{d}k, \tag{A7}$$

$$\int_0^\infty \mathrm{d}k \int_{-\frac{p-k}{2}}^k \mathrm{d}\omega \int_{|\omega|}^{\min(p+p', k+k')} \mathrm{d}q, \tag{A8}$$

$$\int_0^\infty \mathrm{d}k \int_0^{\frac{p-k}{2}} \mathrm{d}k' \int_{|k-k'|}^{\min(p+p', k+k')} \mathrm{d}q. \tag{A9}$$

APPENDIX B: ISOTROPIC HTL MATRIX ELEMENT

Here we derive explicitly the expression for the full isotropic HTL matrix element (54), which is needed for infrared-sensitive contributions in the matrix elements arising from soft gluon exchange. We start with Eq. (36),

$$M_{\mathrm{HTL}} = |G_R(P - P')_{\mu\nu}(P + P')^\mu (K + K')^\nu|^2, \tag{B1}$$

where we insert the HTL retarded propagator in strict Coulomb gauge[12] [92]

$$G_R^{00}(Q) = \frac{i}{q^2 + \Pi_R^{00}(\omega/q)}, \tag{B2}$$

$$G_R^{ij}(Q) = \left(\delta^{ij} - \frac{q^i q^j}{q^2}\right)G_R^T(Q) = \frac{-i\left(\delta^{ij} - \frac{q^i q^j}{q^2}\right)}{q^2 - \omega^2 + \Pi_R^T(\omega/q)} \tag{B3}$$

with $x = \omega/q$ and the self-energies

$$\mathrm{Re}\Pi_R^{00}(x) = m_D^2\left(1 - \frac{x}{2}\ln\left|\frac{x+1}{x-1}\right|\right) \tag{B4}$$

---

[12]By Coulomb gauge we mean using $\partial_i A^i$ as the gauge function and by strict we mean enforcing it strictly, i.e., $\partial_i A^i = 0$, which amounts to setting $\xi = 0$ in the Faddeev-Popov procedure [91].

$$\text{Im}\Pi_R^{00}(x) = \frac{x m_D^2 \pi}{2} \theta(1 - |x|) \tag{B5}$$

$$\text{Re}\Pi_R^T(x) = \frac{m_D^2}{2} - \frac{1}{2}(1 - x^2)\text{Re}\Pi_R^{00} \tag{B6}$$

$$\text{Im}\Pi_R^T(x) = -\frac{1}{2}(1 - x^2)\text{Im}\Pi_R^{00}. \tag{B7}$$

Due to $|x| = |\omega|/q < 1$ in our case [cf., (15)], their imaginary parts are always nonzero. Note that $G_R(-Q)$ corresponds to the advanced propagator, which has a different imaginary part in the self-energy, $\text{Im}\Pi_R(-Q) = -\text{Im}\Pi_R(Q)$. Let us further abbreviate

$$G_R^{00}(-Q) =: z_L = \frac{i}{A + Bi}, \qquad G_R^T(-Q) =: z_T = \frac{-i}{C + Di}, \tag{B8}$$

$$A = q^2 + \text{Re}\Pi_R^{00}(x), \qquad B = \text{Im}\Pi_R^{00}(-x), \tag{B9}$$

$$C = q^2 - \omega^2 + \text{Re}\Pi_R^T(x), \qquad D = \text{Im}\Pi_R^T(-x). \tag{B10}$$

It will turn out that B and D only appear quadratically or as a product. Thus we do not need to distinguish them from $\text{Im}\Pi_R(x)$. We can now split the retarded propagator in (B1) into its temporal and spatial parts and use the expressions for $\mathbf{p}$, $\mathbf{q}$, and $\mathbf{k}$ in the q-frame, i.e., using their parametrizations (19a)–(19c), to obtain

$$M_{\text{HTL}} = |c_1 z_L + c_2 z_T|^2$$
$$= c_1^2 |z_L|^2 + c_2^2 |z_T|^2 + c_1 c_2 (z_L \bar{z}_T + \bar{z}_L z_T), \tag{B11}$$

where $\bar{z}$ means taking the complex conjugate of z and $c_1 = (2p + \omega)(2k - \omega)$ and $c_2 = 4pk \sin\theta_{pq} \sin\theta_{kq} \cos\phi_{kq}$.

This leads to $|z_L|^2 = |G_R^{00}(Q)|^2 = (A^2 + B^2)^{-1}$, $|z_T|^2 = |G_R^T(Q)|^2 = (C^2 + D^2)^{-1}$, and

$$\bar{z}_L z_T + z_L \bar{z}_T = -2(AC + BD)|z_L|^2 |z_T|^2, \tag{B12}$$

eventually yielding

$$M_{\text{HTL}} = c_1^2 |z_L|^2 + c_2^2 |z_T|^2 - 2c_1 c_2 |z_L|^2 |z_T|^2 (AC + BD). \tag{B13}$$

For isotropic distributions $f(k)$ the last term is proportional to $\cos\phi_{kq}$ and may therefore be dropped.

We also need the rescaled matrix element $\tilde{M} = \lim_{p \to \infty} M_{\text{HTL}}/p^2$ in the limit $p \to \infty$. We obtain it by scaling out p [see Eq. (55)]

$$\tilde{c}_1 = \lim_{p \to \infty} c_1/p = 2(2k - \omega), \tag{B14}$$

$$\tilde{c}_2 = \lim_{p \to \infty} c_2/p = 4k \sin\theta_{pq} \sin\theta_{kq} \cos\phi_{kq}, \tag{B15}$$

which yields

$$\tilde{M}_{\text{HTL}} = \tilde{c}_1^2 |z_L|^2 + \tilde{c}_2^2 |z_T|^2 - 2\tilde{c}_1 \tilde{c}_2 |z_L|^2 |z_T|^2 (AC + BD). \tag{B16}$$

Similarly as before, for isotropic distributions $f(k)$ the last term does not contribute.

1. Sum rule

In this appendix, we show that one can analytically perform the ω integral over the HTL matrix element (B16),

$$\int_{-\infty}^{\infty} \frac{d\omega}{q} \tilde{M}_{\text{HTL}}, \tag{B17}$$

using the sum rule from Ref. [32]. The latter allows us to evaluate the integral over a spectral function

$$\int_0^1 \frac{d\omega}{x} \frac{2\text{Im}\Pi(x)}{(z + \text{Re}\Pi(x))^2 + (\text{Im}\Pi(x))^2}$$
$$= \pi \left[\frac{1}{z + \text{Re}\Pi(\infty)} - \frac{1}{z + \text{Re}\Pi(0)} \right], \tag{B18}$$

provided that the function $\Pi(x)$ fulfills the conditions $\text{Im}\Pi(0) = 0$, $\text{Im}\Pi(x) = 0$ for $x \geq 1$, and $\text{Re}\Pi(x) \geq 0$ for $x \geq 1$.

Our analysis applies to the small $\Lambda_\perp$ limit, i.e., we assume only soft momentum transfer $q_\perp \ll k$, with $k \sim T$. Additionally, we take $p \to \infty$, which means $q^2 = q_\perp^2 + \omega^2$, and consider isotropic distributions, for which we may neglect the term in the matrix element $\sim \cos\phi_{kq}$. The matrix element then reads

$$\tilde{M}_{\text{HTL}} = 16k^2 \left(|G_R^{00}|^2 + \left(1 - \frac{\omega^2}{q^2}\right)^2 \cos^2\phi_{kq} |G_R^T|^2 \right), \tag{B19}$$

where, as compared to (54) we have neglected the term linear in $\cos\phi_{kq}$ and odd powers of ω, and also used $\omega^2/k^2 \ll 1$ and $q_\perp^2/(2kq) \ll \omega/q$. Note that only the condition $|\omega| \ll k$ allows us to perform the ω integral without taking the distribution functions into account since otherwise ω also appears in the Bose-enhancement factor, even in the isotropic case where $k' = k - \omega$ [see Eq. (26)]. We have checked numerically that including ω^2/k^2 leads to only little changes. This is because although $|\omega|$ can become arbitrarily large in the integral, these regions are suppressed by the large denominators appearing in the propagators.

To use the sum rule (B18), we write $|G_R|^2$ in terms of the self-energy Π_R, and expand the fraction with the imaginary part of the self-energy,

$$|G_R^{00}|^2 = \frac{2q}{\omega m_D^2 \pi} \frac{\mathrm{Im}\Pi_R^{00}(x)}{(q^2 + \mathrm{Re}\Pi_R^{00})^2 + (\mathrm{Im}\Pi_R^{00})^2} \tag{B20a}$$

$$|G_R^T|^2 = \frac{4q}{\omega m_D^2 \pi (1-x^2)} \frac{\mathrm{Im}\Pi_R^T(x)}{(q_\perp^2 + \mathrm{Re}\Pi_R^T)^2 + (\mathrm{Im}\Pi_R^T)^2}. \tag{B20b}$$

A similar trick is used in [41] to rewrite $|G_R|^2$ in terms of the spectral function ρ. Together with the substitution $\frac{d\omega}{\omega} = \frac{dx}{x(1-x^2)}$, this results in

$$\int_{-\infty}^{\infty} \frac{d\tilde{\omega}}{q} \tilde{M}_{\mathrm{HTL}} = \frac{32k^2}{m_D^2} \left[\frac{1 - 2\cos^2\phi_{kq}}{q_\perp^2 + \frac{m_D^2}{3}} - \frac{1}{q_\perp^2 + m_D^2} + \frac{2\cos^2\phi_{kq}}{q_\perp^2} \right]. \tag{B21}$$

For the longitudinal propagator $|G_R^{00}|^2$ the factor $(1-x^2)$ from the coordinate transformation needs to be absorbed into the self-energy $\tilde{\Pi}_R^{00}(x) = (1-x^2)\Pi_R^{00}(x)$. The relevant limits read

$$\mathrm{Re}\Pi_R^T(0) = 0, \qquad \mathrm{Re}\tilde{\Pi}_R^{00}(0) = m_D^2, \tag{B22a}$$

$$\mathrm{Re}\Pi_R^T(\infty) = \frac{m_D^2}{3}, \qquad \mathrm{Re}\tilde{\Pi}_R^{00}(\infty) = \frac{m_D^2}{3}. \tag{B22b}$$

Integrating over ϕ_{kq} and $q_\perp$ leads to the cancellation of the terms involving the plasmon mass and the familiar result

$$\int_0^{\Lambda_\perp} dq_\perp \, q_\perp^3 \int_0^{2\pi} d\phi_{kq} \int_{-\infty}^{\infty} \frac{d\omega}{q} M_{\mathrm{HTL}}$$
$$= \frac{32k^2}{m_D^2} \int_0^{\Lambda_\perp} dq_\perp \, q_\perp^3 \frac{m_D^2}{q_\perp^2 (q_\perp^2 + m_D^2)} \tag{B23}$$

$$= 16k^2 \ln\left(1 + \frac{\Lambda_\perp^2}{m_D^2}\right). \tag{B24}$$

A similar result is obtained in [31,32] in thermal equilibrium, where also the integral over the distribution functions $f(k)(1+f(k))$ is automatically included. Here, we have shown explicitly that the matrix element itself gives rise to the form (B24). In the soft limit, this enables us to perform the integral over the distribution function separately, allowing a straightforward generalization to nonequilibrium systems. Finally, we note that we use this sum rule in Sec. III F to set the ξ parameter in the approximate ξ-screening prescription.

APPENDIX C: BEHAVIOR OF $\hat{q}$ FOR LARGE JET MOMENTA

In this appendix, we study the behavior of the jet quenching parameter $\hat{q}$ for large jet momentum p and in particular, how to correctly perform the limit $p \to \infty$. We

will show that taking the term at a naïve leading order in $1/p$ in the integrand of $\hat{q}^{ij}$ is indeed sufficient to obtain the correct leading-order contribution. This is not trivial since p also appears in the integration boundaries and this analysis requires caution. Thus, there are two possible sources for large-p contributions to $\hat{q}$: the integrand and the integral boundaries. Our strategy here will be to expand the integrand in orders of $1/p$ and then perform the integrals.

We will illustrate the large p behavior of $\hat{q}$ using the gluonic matrix element,

$$\hat{q} \sim \int_0^\infty dk \int_{-\frac{p-k}{2}}^k d\omega \int_{|\omega|}^{\min(p+p',k+k')} dq$$
$$\times q^2(1-v_{pq}^2) \frac{|\mathcal{M}_{gg}^{gg}|^2}{p^2} f_b(\mathbf{k})(1 \pm f_d(\mathbf{k}')). \tag{C1}$$

The distribution function $f(\mathbf{k})$ provides an upper limit for the momentum of the plasma constituent k, which we assume to be much smaller than the jet momentum p, thus $k \ll p$. Thus the minimum of $(p+p', k+k') = (2p + \omega, 2k - \omega)$ is always $2k - \omega$, because $2k - \omega < 2p + \omega$ for $\omega > k - p$, which is always fulfilled due to the lower boundary of the ω-integral, $\omega > \frac{k-p}{2}$. Then the only p dependence in the integration boundaries of Eq. (C1) comes from the lower limit of the ω integral.

Therefore, we will be interested in the region $\omega < 0$, where $|\omega|$ is very large. In particular, we will assume $|\omega| > \Lambda_\omega \gg k$ with a new scale Λ_ω, which will lead to simplifications in the matrix element. Additionally, the *Bose-enhanced* term $\hat{q}_{\mathrm{ff}}$ that includes $f(\mathbf{k})f(\mathbf{k}')$ does not contribute in this limit, since $f(\mathbf{k}') \approx 0$. Focusing only on relevant terms, i.e., disregarding the k-integral since it cannot contribute to any large p behavior, we analyze

$$\hat{q} \sim \int_{-\frac{p-k}{2}}^{-\Lambda_\omega} d\omega \int_{|\omega|}^{2k-\omega} dq \, q^2(1-v_{pq}^2) \frac{|\mathcal{M}_{gg}^{gg}|^2}{p^2}. \tag{C2}$$

1. The integrand of $\hat{q}$ for large p

Now let us expand the integrand in (C2) for large p explicitly.

a. The limit of v_{pq}

First, we consider $v_{pq} = \cos\theta_{pq}$ in the limit $p \to \infty$. Our starting point is Eq. (30a),

$$v_{pq} = \frac{1}{q}\left(\omega + \frac{\omega^2 - q^2}{2p}\right). \tag{C3}$$

Using Eq. (15), i.e., $q < 2k - \omega$, one has

$$\frac{q^2 - \omega^2}{2p} < \frac{4k(k-\omega)}{2p} \ll |\omega|, \tag{C4}$$

which leads for $p \to \infty$ to

$$v_{pq} = \frac{\omega}{q}. \tag{C5}$$

However, considering the term $1 - v_{pq}^2$ that appears in (C2) is more subtle, because the seemingly leading term in a $1/p$ expansion, ω/q, is close to unity. This leads to the corrections

$$
\begin{aligned}
1 - v_{pq}^2 &= 1 - \frac{\omega^2}{q^2} + \frac{\omega(q^2 - \omega^2)}{pq^2} + \dots \\
&= \left(1 - \frac{\omega^2}{q^2}\right)\left(1 + \frac{\omega}{p} + \dots\right),
\end{aligned} \tag{C6}
$$

where the correction term ω/p can in principle become large at the lower boundary of the ω integral, $\omega > -(p-k)/2$.

b. Matrix element for large $|\omega|$

For large $|\omega|$, and therefore also large q, we do not need to take into account screening effects $\mathcal{O}(m_D)$ in the matrix element, such that (38) reduces to $M_{\text{screen}} \approx M_0 = (s-u)^2/t^2$. The contribution from the transverse propagator in the sum in (38) is negligible for large $|\omega|$, and we are left with

$$\frac{|\mathcal{M}_{gg}^{gg}|^2}{g^4 p^2} = 16 d_A C_A^2 \frac{\omega^2}{q^4}\left(1 + \frac{\omega}{p} + \dots\right). \tag{C7}$$

Collecting the pieces, we can rewrite the relevant integrand in (C2) as

$$
\begin{aligned}
&q^2(1 - v_{pq}^2)\frac{|\mathcal{M}_{gg}^{gg}|^2}{g^4 p^2} \\
&= 16 d_A C_A^2 \frac{(q^2 - \omega^2)\omega^2}{q^4}\left(1 + \frac{2\omega}{p} + \dots\right).
\end{aligned} \tag{C8}
$$

2. Integral over a more generic integrand

The integrand relevant for determining the large p dominant behavior for $\hat{q}$ is a sum of terms $q^n \omega^m$, as can be seen from (C8). Let us therefore analyze a general integrand of this form and define the integral I_{nm},

$$I_{nm}(p) = \int_{-\frac{p-k}{2}}^{-\Lambda_\omega} d\omega \int_{-\omega}^{2k-\omega} dq \, q^n \omega^m. \tag{C9}$$

Although $|\omega| \gg 2k$, we cannot neglect $2k$ in the upper integration boundary of the q integral, which additionally complicates our analysis. With $\tilde{\omega} = -\omega > 0$ we get rid of

additional minus signs and obtain for $n \neq -1$

$$I_{nm}(p) = (-1)^m \int_{\Lambda_\omega}^{\frac{p-k}{2}} d\tilde{\omega} \int_{\tilde{\omega}}^{2k+\tilde{\omega}} dq \, q^n x^m, \tag{C10}$$

$$= \frac{(-1)^m}{n+1}\int_{\Lambda_\omega}^{\frac{p-k}{2}} d\tilde{\omega}\, x^m[(2k+\tilde{\omega})^{n+1} - \tilde{\omega}^{n+1}]. \tag{C11}$$

We expand the first term in a power series using the Binomial series

$$(x+y)^r = \sum_{k=0}^{\infty}\binom{r}{k}x^{r-k}y^k, \qquad x, y \in \mathbb{R}, \tag{C12}$$

with $|x| > |y|$ and $r \in \mathbb{C}$. We thus obtain

$$
\begin{aligned}
I_{nm} = &\frac{(-1)^m}{n+1}\int_{\Lambda_\omega}^{\frac{p-k}{2}} d\tilde{\omega} \\
&\times \tilde{\omega}^m\left[\sum_{j=0}^{\infty}\binom{n+1}{j}\tilde{\omega}^{n+1-j}(2k)^j - \tilde{\omega}^{n+1}\right]
\end{aligned} \tag{C13}
$$

$$= \frac{(-1)^m}{n+1}\int_{\Lambda_\omega}^{\frac{p-k}{2}} d\tilde{\omega}\sum_{j=1}^{\infty}\binom{n+1}{j}\tilde{\omega}^{n+m+1-j}(2k)^j \tag{C14}$$

$$
\begin{aligned}
= \frac{(-1)^m}{n+1}&\left(\sum_{\substack{j=1\\j\neq n+m+2}}^{\infty}\binom{n+1}{j}\frac{\tilde{\omega}^{n+m+2-j}}{n+m+2-j}\bigg|_{\tilde{\omega}=\Lambda_\omega}^{\frac{p-k}{2}}(2k)^j\right. \\
&\left.+ \binom{n+1}{n+m+2}\ln\left(\frac{p-k}{2\Lambda_\omega}\right)(2k)^{n+m+2}\right).
\end{aligned} \tag{C15}
$$

Since we are interested in the behavior at large p, we drop the lower boundary $\tilde{\omega} = \Lambda_\omega$ and take only the leading-order (LO) terms with the largest powers of p into account. Those are obtained for $j = 1$, for which the (generalized) binomial coefficient yields $n+1$. It will be useful to also consider the next-to-leading order (NLO) terms in p. We obtain, up to an additive constant,

$$I_{nm}^{\text{LO}} \simeq \begin{cases} \frac{(-1)^m(2k)}{n+m+1}\left(\frac{p-k}{2}\right)^{n+m+1}, & n+m+1 \neq 0 \\ (-1)^m(2k)\ln(p), & n+m+1 = 0 \end{cases} \tag{C16a}$$

$$I_{nm}^{\text{NLO}} \simeq \begin{cases} \frac{(-1)^m(2k)^2}{(n+1)(n+m)}\binom{n+1}{2}\left(\frac{p-k}{2}\right)^{n+m}, & n+m \neq 0 \\ \frac{(-1)^m}{n+1}\binom{n+1}{2}(2k)^2\ln(p), & n+m = 0. \end{cases} \tag{C16b}$$

Note that the inclusion of k in $(p-k)^{n+m+1}$ in the LO term is because it will contribute at NLO.

3. Behavior of $\hat{q}$ for large p

Gathering the results of the previous sections and applying them to the integral of $\hat{q}$ in (C2) with the integrand (C8), we obtain

$$\hat{q}^{\text{LO}} \sim I_{-2,2} - I_{-4,4} = (2k)^2 \ln p + \text{const}, \qquad \text{(C17a)}$$

$$\hat{q}^{\text{NLO}} \sim \frac{1}{p}(I_{-2,3} - I_{-4,5}) = \text{const} + \mathcal{O}\left(\frac{1}{p}\right). \qquad \text{(C17b)}$$

Note that here with NLO we denote the terms proportional to $1/p$ in the integrand. For both cases, $n + m$ is constant, thus the leading terms (C16a) cancel and we need the next-to-leading terms (16b). Indeed we observe that, due to the logarithmic enhancement of the leading-order contributions $\hat{q}^{\text{LO}}$, the next-to-leading order contributions $\hat{q}^{\text{NLO}}$ become negligible[13] for sufficiently large p, and $\hat{q}$ can be written in the form of Eq. (48),

$$\hat{q}(p \gg Q) \simeq a_p \ln p + b_p. \qquad \text{(C18)}$$

Therefore, for sufficiently large jet momenta p, it is in principle enough to expand the matrix element and the integrand for large p and take only the leading-order contribution in p. Note, however, that to obtain the constant term it is not enough to use the leading large p behavior, but one must use the full matrix element.

Let us now see how we can obtain the coefficient of the logarithm, a_p. Until now, we have not considered the exact form of the distribution function $f(\mathbf{k})$ and merely used that it provides an upper cutoff for the k integral. The numerical value of the coefficient a_p will depend on the exact form of $f(\mathbf{k})$.

Let us consider a gluon jet scattering off a gluon in the plasma and start with Eq. (26),

$$\hat{q} \simeq \frac{16g^4 C_A^2}{2^{10}\pi^5} \int_0^{2\pi} d\phi_{pq} \int_0^{2\pi} d\phi_{kq} \int_0^\infty dk$$
$$\times \int_{-\frac{p-k}{2}}^k d\omega \int_{|\omega|}^{2k-\omega} dq\, f(\mathbf{k}) \frac{\omega^2(q^2 - \omega^2)}{q^4}, \qquad \text{(C19)}$$

where we have taken the leading term in the large p integrand (C8) that leads to the logarithmic behavior. Additionally, as explained below Eq. (C1), it is sufficient to use $2k - \omega$ as the upper boundary of the q integral.

---

[13]This is not a trivial statement: for an integrand $q^n \omega^m (1 + \omega/p)$ with $n + m > 0$, we would obtain $\frac{\hat{q}^{\text{NLO}}}{\hat{q}^{\text{LO}}} = \frac{\frac{1}{p}(ap^{n+m+2}+b)}{cp^{n+m+1}+e} \sim \frac{a}{c} + \mathcal{O}(\frac{1}{p})$, thus the ratio NLO/LO does not necessarily become 0 for $p \to \infty$. This implies that multiplying the LO term with ω/p and integrating over it yields a term of the same order as the LO term.

In comparison to the general integrand we analyzed in Eq. (C9), there appears also the distribution function $f(\mathbf{k}) = f(k, v_k)$, and the angle $v_k = \cos\theta_k$ depends on $v_{kq} = \cos\theta_{kq}$ and $v_{pq} = \cos\theta_{pq}$ as well, which are functions of ω and q, as in Eq. (30d). For the large p behavior, we are interested in the region $|\omega| \gg k$ and $q \sim |\omega|$, which renders $v_{pq} \to -1$. For v_{kq}, however, we cannot make a definite statement, since it changes from -1 to 1 when q varies between its integration boundaries $|\omega| < q < 2k - \omega$. Therefore, for anisotropic systems, without knowing the explicit form of $f(\mathbf{k})$, we cannot calculate the coefficient a_p. We will thus restrict ourselves to isotropic distributions $f(k)$ here that only depend on the magnitude of $\mathbf{k}$. Then, the ω and q integrations in Eq. (C19) are given by Eq. (C17a).

For an isotropic plasma consisting of quarks and gluons with distributions f_q and f_g, the coefficient a_p is then given by Eq. (49),

$$a_p/C_R = \frac{C_A g^4}{4\pi^3} \int_0^\infty dk\, k^2 f_g(k)$$
$$+ \sum_f \frac{d_F C_F g^4}{4\pi^3 d_A} \int_0^\infty dk\, k^2 f_q(k). \qquad \text{(C20)}$$

In thermal equilibrium, this reduces to

$$\frac{a_p^{\text{eq}}}{C_R} = \frac{g^4 \zeta(3) T^3}{2\pi^3}\left(N_C + \frac{3}{4}n_f\right). \qquad \text{(C21)}$$

This logarithmic behavior of $\hat{q}^{\text{LO}}$ implies that the limit $p \to \infty$ requires a UV cutoff to render $\hat{q}$ finite. This is typically done by restricting the transverse momentum transfer, $q_\perp < \Lambda_\perp$. We will show in the next section that in this limit $\hat{q}$ is finite and we only need to consider the leading-order term in p in the integrand.

4. Large p behavior combined with a momentum cutoff $q_\perp < \Lambda_\perp$

Using a transverse momentum cutoff, $q_\perp < \Lambda_\perp \ll p$, we can retrace the steps in the previous sections. For large p, apart from factors $\mathcal{O}(1/p)$, this amounts to $q_\perp^2 = q^2 - \omega^2 < \Lambda_\perp^2$ [cf., (50)], and thus we modify I_{nm} to

$$I_{nm}(p) = \int_{-\frac{p-k}{2}}^{-\Lambda_\omega} d\omega \int_{-\omega}^{\sqrt{\omega^2+\Lambda_\perp^2}} dq\, q^n \omega^m. \qquad \text{(C22)}$$

The upper limit in the q integral replaces $2k - \omega$ in Eq. (C9) for sufficiently large Λ_ω because $\sqrt{\omega^2 + \Lambda_\perp^2} < 2k - \omega$ for $-\omega > \frac{\Lambda_\perp^2}{4k} - k$, which, since $-\omega > \Lambda_\omega$, can always be fulfilled by choosing

$$\Lambda_\omega > \frac{\Lambda_\perp^2}{4k} - k. \tag{C23}$$

Similarly as before, with $\tilde{\omega} = -\omega$ and for $n \neq -1$, we obtain

$$I_{nm}(p) = \frac{(-1)^m}{n+1} \int_{\Lambda_\omega}^{\frac{p-k}{2}} d\tilde{\omega} \, \tilde{\omega}^m [(\tilde{\omega}^2 + \Lambda_\perp^2)^{\frac{n+1}{2}} - \tilde{\omega}^{n+1}]. \tag{C24}$$

For the convergence of the Binomial series (C12), we need to check that $\Lambda_\perp^2 < \tilde{\omega}^2$, which follows from (C23),[14] and thus,

$$I_{nm} = \frac{(-1)^m}{n+1} \int_{\Lambda_\omega}^{\frac{p-k}{2}} d\tilde{\omega} \sum_{j=1}^{\infty} \binom{(n+1)/2}{j} \tilde{\omega}^{n+m+1-2j}(\Lambda_\perp)^{2j} \tag{C25}$$

$$= \frac{(-1)^m}{n+1} \left[\sum_{\substack{j=1 \\ j \neq (n+m+2)/2}}^{\infty} \binom{(n+1)/2}{j} \frac{\tilde{\omega}^{n+m+2-2j}}{n+m+2-2j} \bigg|_{\tilde{\omega}=\Lambda_\omega}^{\frac{p-k}{2}} \Lambda_\perp^{2j} + \binom{(n+1)/2}{(n+m+2)/2} \ln\left(\frac{p-k}{2\Lambda_\omega}\right) \Lambda_\perp^{n+m+2} \right]. \tag{C26}$$

We now obtain, up to an additive constant (in p),

$$I_{nm}^{\text{LO}} = \begin{cases} \frac{(-1)^m \Lambda_\perp^2}{2(n+m)} \left(\frac{p-k}{2}\right)^{n+m}, & n+m \neq 0 \\ (-1)^m \Lambda_\perp^2 \ln(p), & n+m = 0 \end{cases} \tag{C27}$$

$$I_{nm}^{\text{NLO}} = \begin{cases} \frac{(-1)^m \Lambda_\perp^4 B}{(n+1)(n+m-2)} \left(\frac{p-k}{2}\right)^{n+m-2}, & n+m-2 \neq 0 \\ \frac{(-1)^m}{n+1} B \Lambda_\perp^4 \ln(p), & n+m-2 = 0, \end{cases} \tag{C28}$$

where $B = \binom{(n+1)/2}{2}$. In this case, denoting again with NLO the terms proportional to $1/p$ in the integrand, we obtain

$$\hat{q}^{\text{LO}} \sim I_{-2,2} - I_{-4,4} \sim \text{const} + \mathcal{O}\left(\frac{1}{p^2}\right), \tag{C29a}$$

$$\hat{q}^{\text{NLO}} \sim \frac{1}{p}(I_{-2,3} - I_{-4,5}) \sim \frac{\text{const}}{p} + \mathcal{O}\left(\frac{1}{p^2}\right). \tag{C29b}$$

Thus, with a transverse momentum cutoff $\Lambda_\perp$ in place, we can explicitly take the limit of infinite jet momentum, $p \to \infty$, and obtain a finite jet quenching parameter $\hat{q}$. Moreover, it is then sufficient to take the leading-order

---

[14]We know that $\Lambda_\perp^2 < 4k\Lambda_\omega(1 + \frac{k}{\Lambda_\omega}) \approx 4k\Lambda_\omega$ and thus $\Lambda_\perp^2/\Lambda_\omega^2 < \frac{4k}{\Lambda_\omega} \ll 1$, which makes $\Lambda_\perp < \Lambda_\omega$ and thus $\Lambda_\perp < \tilde{\omega}$.

terms in the integrand (in particular the matrix elements) in an expansion in $1/p$.

5. Large momentum cutoff $\Lambda_\perp$ behavior

Removing the momentum cutoff, i.e., taking $\Lambda_\perp \to \infty$, leads to a divergent jet quenching parameter $\hat{q}$. It is reasonable to assume that this divergence will be logarithmic, as it is for finite but large jet momentum. We will now show this explicitly and calculate the coefficient of the logarithm.

We continue working in the limit $p \to \infty$, and thus take only the leading-order terms in p in the integrand into account. For that we start with Eq. (A6) with explicit step functions and perform the coordinate transformation in Eq. (65) to integrate over $\mathbf{q}_\perp$,

$$\hat{q} \sim \int_0^\infty dk \int_{q_\perp < \Lambda_\perp} d^2 \mathbf{q}_\perp \int_{-\infty}^{k-\frac{q_\perp^2}{4k}} d\omega$$
$$\times q_\perp^2 f(\mathbf{k})(1 \pm f(\mathbf{k}')) \frac{|\mathcal{M}_{gg}^{gg}|^2}{p^2 \sqrt{q_\perp^2 + \omega^2}}, \tag{C30}$$

where we have not included the angular integrals.

The behavior for large $\Lambda_\perp$ is of course dominated by the upper integration boundary of the $q_\perp$ integral. For large $\Lambda_\perp$, we now split the integral into a part $0 < q_\perp < \Lambda_\omega$ and $\Lambda_\omega < q_\perp < \Lambda_\perp$. We can choose the scale $\Lambda_\omega \gg k$, such that $q_\perp \gg k$, since the momentum k has a natural upper cutoff coming from the distribution function $f(\mathbf{k})$. Then, also $|\omega| > \frac{q_\perp^2}{4k} - k$ must be very large and thus $f(\mathbf{k}') \approx 0$. Hence we arrive at the scale separation

$$|\omega| \gg q_\perp \gg k. \tag{C31}$$

Using this for the integrand (C8), we obtain

$$\hat{q} \sim \int_{\Lambda_\omega}^{\Lambda_\perp} dq_\perp \, q_\perp \int_{-\infty}^{k-\frac{q_\perp^2}{4k}} d\omega \, q_\perp^2 \frac{1}{|\omega|^3}$$
$$\approx 8k^2 \int_{\Lambda_\omega}^{\Lambda_\perp} dq_\perp \frac{q_\perp^3}{q_\perp^4} = 8k^2 \ln \Lambda_\perp + \text{const.} \tag{C32}$$

We have thus shown that we can write $\hat{q}$ in that limit as in Eq. (57),

$$\hat{q}(\Lambda_\perp \gg Q) \simeq a_{\Lambda_\perp} \ln \Lambda_\perp + b_{\Lambda_\perp}. \tag{C33}$$

It is also possible to determine the coefficient of $\ln \Lambda_\perp$, similarly as in Appendix C 3. For anisotropic systems, the distribution function depends implicitly on ω and $q_\perp$ via the angle $\cos \theta_k = v_k$; see Eq. (30d). With the scale separation (C31), we find $v_{pq} \to -1$, similarly as in Appendix C 3. Additionally, v_{kq} changes from $v_{kq} \to -1$ for $|\omega| \to \infty$ to $v_{kq} \to 1$ for $|\omega| \to q_\perp^2/4k - k$, and similarly for $v_{k'q} \to -1$.

Note that v_{kq} decreases rather quickly for increasing $|\omega|$, thus we cannot make predictions for arbitrary anisotropic systems, and assume an isotropic distribution for calculating $a_{\Lambda_\perp}$. With this approximation, we can now perform the integral in Eq. (C32).

For a plasma consisting of quarks and gluons with distributions f_q and f_g, we then obtain the coefficient

$$
\frac{a_{\Lambda_\perp}}{C_R} = \frac{C_A g^4}{2\pi^3} \int_0^\infty dk\, k^2 f_g(k)
$$
$$
+ \sum_f \frac{d_F C_F g^4}{2\pi^3 d_A} \int_0^\infty dk\, k^2 f_f(k), \quad (C34)
$$

which reduces for thermal distributions to

$$
\frac{a_{\Lambda_\perp}^{eq}}{C_R} = \frac{g^4 \zeta(3) T^3}{\pi^3} \left(N_C + \frac{3}{4} n_f \right). \quad (C35)
$$

This nicely agrees with Eq. (81a) that stems from [30].

APPENDIX D: MONTE-CARLO SAMPLING

In this appendix, we describe the implementation of the Monte-Carlo integration. Our implementation can be found in [93].

We evaluate the five-dimensional integral in (26) with the measures (52a)–(52c) using Monte-Carlo integration with importance sampling. For the angular parts, we sample uniformly from 0 to 2π.

The other three integrals can be summarized into three categories. The first one corresponds to (52b) and is given by

$$
I_1 = \int_{k_{min}}^{k_{max}} dk \int_{k_{min}}^\infty dk' \int_{|k-k'|}^{\min(k+k', \sqrt{(k-k')^2 + \Lambda_\perp^2})} dq, \quad (D1)
$$

where we have implemented the boundaries $k_{min} < k < k_{max}$ coming for the finite discretization of the distribution function $f(\mathbf{k})$, and similarly $k_{min} < k'$, and also used the $q_\perp$ cutoff, $q^2 - \omega^2 < \Lambda_\perp^2$. We can rewrite this equivalently as

$$
I_1 = \int_{k_{min}}^{k_{max}} dk \int_{-\infty}^{k-k_{min}} d\omega \int_{|\omega|}^{\min(2k-\omega, \sqrt{\omega^2 + \Lambda_\perp^2})} dq, \quad (D2)
$$

which corresponds to (52a).

For the different order of integration as in (52c) the conditions $k_{min} < k$ and $k_{min} < k'$ amount to

$$
I_2 = \int_0^\infty dq \int_{-q}^{\min(q, 2k_{max}-q, k_{max}-k_{min})} d\omega \int_{\max(\frac{q+\omega}{2}, k_{min}, k_{min}+\omega)}^{k_{max}} dk, \quad (D3)
$$

where due to the $q_\perp$ cutoff, for $q > \Lambda_\perp$ we cut the following region $(-\sqrt{q^2 - \Lambda_\perp^2}, \sqrt{q^2 - \Lambda_\perp^2})$ out of the integration region of the ω integral.

For the q integral we sample q from a probability distribution $\sim (q+m)^{-2}$, where m is the gluon asymptotic mass $m = m_D/\sqrt{2}$. Thus we perform the integral according to

$$
\int_{q_{min}}^{q_{max}} dq\, f(q) \approx \frac{q_{max} - q_{min}}{N(q_{max} + m)(q_{min} + m)}
$$
$$
\times \sum_{i=1}^N (q_i + m)^2 f(q_i), \quad (D4)
$$

where $q_i = (1/(q_{min} + m) - y_i)^{-1} - m$ and y_i is sampled uniformly in $(0, (q_{max} - q_{min})(q_{max} + m)^{-1}(q_{min} + m)^{-1})$.

We sample ω uniformly and k from a $1/k$ distribution,

$$
\int_{k_{min}}^{k_{max}} dk\, f(k) \approx \ln\left(\frac{k_{max}}{k_{min}}\right) \frac{1}{N} \sum_{i=1}^N k_i f(k_i), \quad (D5)
$$

where $k_i = k_{min} e^{r_i}$ and r_i is sampled uniformly in $(0, \ln k_{max}/k_{min})$.

APPENDIX E: DETAILS ON $\hat{q}$ CALCULATIONS IN TOY MODELS

1. Extremely anisotropic distribution

We now calculate $\hat{q}_{ff}^{ij}$ for a jet going in the x direction and the distribution (89), which we rewrite as

$$
f(\mathbf{k}) = AQ^3 \delta(k_z) \delta(k_x^2 + k_y^2 - \tilde{k}^2). \quad (E1)
$$

We do not need to enforce a momentum cutoff $q_\perp < \Lambda_\perp$, since $\hat{q}_{ff}$ is finite even for $p \to \infty$. Hence, we can assume that the transverse momentum cutoff $\Lambda_\perp$ is sufficiently large, at least $\Lambda_\perp > 2\tilde{k}$, as we will see later.

We first note that the expression for $\hat{q}_{ff}^{zz}$ is proportional to $\int (q^z)^2 \delta(k_z) \delta(k_z')$. The delta functions enforce $k_z = k_z' = 0$ and thus also $q_z = k_z - k_z' = 0$ and $\hat{q}_{ff}^{zz} = 0$. Note that we have obtained this result without using a specific form of the matrix element.

For $\hat{q}_{ff}^{yy}$ we use (A6) and insert $f(\mathbf{k})$ in (E1), obtaining

$$
\hat{q}_{ff}^{yy} = \frac{A^2 Q^6}{16 p^2 \nu} \int \frac{d^3\mathbf{k} d^3\mathbf{q} d\omega}{(2\pi)^5 q^2 k^2} q^y q^y |\mathcal{M}(\mathbf{p}, \mathbf{k}; \mathbf{p}', \mathbf{k}')|^2
$$
$$
\times \delta\left(\cos\theta_{pq} - \frac{\omega}{q} - \frac{\omega^2 - q^2}{2pq} \right)
$$
$$
\times \delta\left(\cos\theta_{kq} - \frac{\omega}{q} + \frac{\omega^2 - q^2}{2kq} \right)
$$
$$
\times \theta(p' - k')\theta\left(p - \frac{q - \omega}{2} \right)\theta\left(k - \frac{q + \omega}{2} \right)\theta(q - |\omega|)
$$
$$
\times \delta(k_z)\delta(q_z)\delta(k^2 - \tilde{k}^2)\delta((\mathbf{k} - \mathbf{q})^2 - \tilde{k}^2). \quad (E2)
$$

The delta functions can be rewritten as $\delta((\mathbf{k} - \mathbf{q})^2 - \tilde{k}^2) = \delta(\omega^2 - 2\omega\tilde{k}) = \frac{1}{2\tilde{k}}(\delta(\omega) + \delta(\omega - 2\tilde{k}))$ and $\delta(k^2 - \tilde{k}^2) = \frac{1}{2\tilde{k}}\delta(k - \tilde{k})$. We can thus integrate out k_z and q_z and rewrite the remaining integrations as a two-dimensional integral. For $p \to \infty$ the theta functions containing p and p' do not need to be written explicitly. The $\delta(\omega - 2k)$ term vanishes because then the third Heaviside function becomes $\theta(-q/2) = 0$. Integrating over ω enforces $\omega = 0$. Due to the considered large-p limit, the first delta function becomes $\delta(\cos\theta_{pq}) = q\delta(q_x)$, and integrating out q_x as well, we arrive at

$$\hat{q}_{\text{ff}}^{yy} = \frac{A^2 Q^6}{16 p^2 \nu} \int \frac{\mathrm{d}k_x \mathrm{d}k_y \mathrm{d}q_y}{(2\pi)^5 q_y k^2} (q_y)^2 |\mathcal{M}(\mathbf{p}, \mathbf{k}; \mathbf{p}', \mathbf{k}')|^2$$

$$\times \delta\left(\cos\theta_{kq} - \frac{|q_y|}{2\tilde{k}}\right)\theta\left(\tilde{k} - \frac{|q_y|}{2}\right)\frac{1}{4\tilde{k}^2}\delta(k - \tilde{k}). \quad \text{(E3)}$$

Effectively, $\mathbf{q}$ is parallel to the y–axis and $\mathbf{k}$ lies in the x–y plane with length $\tilde{k}$ and $k_y = |q_y|/2$. For the matrix element we need $q = |q_y|$, $k = \tilde{k}$, and ϕ_{kq}, which is the polar angle of $\mathbf{k}$ in a frame, in which $\mathbf{q}$ points in the z direction and $\mathbf{p}$ lies in the x–z plane; see Sec. III B. In our case, $\mathbf{q}$ is orthogonal to $\mathbf{p}$, thus we perform the $\mathbf{k}$ integration in a frame, in which $\mathbf{q} = q\mathbf{e}_{z^3}$, $\mathbf{p} = -p\mathbf{e}_{x^3}$. Since $\mathbf{k}$ must lie in the $\mathbf{p} - \mathbf{q}$ plane, we obtain

$$\phi_{kq} \in \{0, \pi\}. \quad \text{(E4)}$$

We get a factor 2 from the symmetry $q_y \leftrightarrow -q_y$ and insert the gluonic matrix element from Table II with the approximation (56), and sum over the possible values of $\cos\phi_{kq}$, 1 and -1. Thus we obtain, for a momentum cutoff $\Lambda_\perp > 2\tilde{k}$,

$$\hat{q}_{\text{ff}}^{yy} = \frac{d_A C_A^2 A^2 g^4 Q^6}{2^6 \pi^5 \nu \tilde{k}^3} \int_0^{2\tilde{k}} \mathrm{d}q\, q \quad \text{(E5)}$$

$$\times \frac{(2\tilde{k} - \sqrt{4\tilde{k}^2 - q^2})^2 + (2\tilde{k} + \sqrt{4\tilde{k}^2 - q^2})^2}{(q^2 + \xi^2 m_D^2)^2}$$

$$= \frac{d_A C_A^2 A^2 g^4 Q^6}{(2\pi)^5 \nu \tilde{k}^3} \int_0^{2\tilde{k}} \mathrm{d}q\, q \frac{8\tilde{k}^2 - q^2}{(q^2 + \xi^2 m_D^2)^2}. \quad \text{(E6)}$$

The integral over q can be performed analytically, which yields Eq. (91).

2. Evaluating $\hat{q}$ for the scaled thermal distribution

Here we describe briefly a few technical details used in the evaluation of (26) with (52c) for the scaled thermal distribution (92) in Sec. IV B 2. As independent parameters we have

  (i) the coupling $\lambda = g^2 N_C$,
  (ii) the temperature T, and
  (iii) the occupancy N_+ (and N_-, but here we consider a purely gluonic plasma).

All dimensionful quantities are given in terms of the temperature T. Then we have two independent parameters left, on which $\hat{q}$ will depend. Every matrix element comes with a factor $g^4 \sim \lambda^2$, which we can factor out. Since the Debye mass scales with $N_+\lambda$, the scaled matrix element then depends only on this combination,

$$|\mathcal{M}_{cd}^{ab}(N_+, \lambda)|^2 = \lambda^2 |\tilde{M}_{cd}^{ab}(N_+\lambda)|^2. \quad \text{(E7)}$$

Then Eq. (26) becomes

$$\hat{q} = \sum_{bcd} \int \mathrm{d}\tilde{\Gamma}\, q^2 \sin^2\theta_{pq} \frac{|\tilde{M}_{cd}^{ab}(N_+\lambda)|^2}{p^2}$$

$$\times \lambda^2 f_b(k)(1 \pm f_d(k - \omega)), \quad \text{(E8)}$$

where $\mathrm{d}\tilde{\Gamma}$ denotes the integration measure and constant factors present in (26).

In a purely gluonic plasma, we can now consider $\hat{q}_{\text{f}}/\lambda$ and $\hat{q}_{\text{ff}}$ separately as functions of $N_+\lambda$ as in Eq. (98),

$$\hat{q} = \lambda\left(\frac{\hat{q}_{\text{f}}}{\lambda}\right)(N_+\lambda) + \hat{q}_{\text{ff}}(N_+\lambda), \quad \text{(E9)}$$

with

$$\lambda\left(\frac{\hat{q}_{\text{f}}}{\lambda}\right) = \lambda \int \mathrm{d}\Gamma\, q^2 \sin^2\theta_{pq} \frac{|\tilde{M}_{gg}^{gg}(N_+\lambda)|^2}{p^2} \lambda f_g(k), \quad \text{(E10)}$$

$$\hat{q}_{\text{ff}} = \int \mathrm{d}\Gamma\, q^2 \sin^2\theta_{pq} \frac{|\tilde{M}_{gg}^{gg}(N_+\lambda)|^2}{p^2} \lambda^2 f_g(k) f_g(k - \omega). \quad \text{(E11)}$$

Note that f also contains a factor N_+, which, together with λ combines to the $N_+\lambda$ behavior in (98). Thus we can obtain $\hat{q}_{\text{f}}$ and $\hat{q}_{\text{ff}}$ numerically with one independent parameter, $N_+\lambda$, and then add the second independent parameter later.

[1] R. Baier, Alfred H. Mueller, D. Schiff, and D. T. Son, "Bottom up" thermalization in heavy ion collisions, Phys. Lett. B **502,** 51 (2001).

[2] Francois Gelis, Edmond Iancu, Jamal Jalilian-Marian, and Raju Venugopalan, The color glass condensate, Annu. Rev. Nucl. Part. Sci. **60,** 463 (2010).

[3] Aleksi Kurkela, Tuomas Lappi, and Jarkko Peuron, Time evolution of linearized gauge field fluctuations on a real-time lattice, Eur. Phys. J. C **76,** 688 (2016).

[4] K. Boguslavski, A. Kurkela, T. Lappi, and J. Peuron, Spectral function for overoccupied gluodynamics from real-time lattice simulations, Phys. Rev. D **98,** 014006 (2018).

[5] K. Boguslavski, A. Kurkela, T. Lappi, and J. Peuron, Broad excitations in a 2 + 1D overoccupied gluon plasma, J. High Energy Phys. 05 (2021) 225.

[6] Kirill Boguslavski, Tuomas Lappi, Mark Mace, and Sören Schlichting, Spectral function of fermions in a highly occupied non-Abelian plasma, Phys. Lett. B **827,** 136963 (2022).

[7] Peter Brockway Arnold, Guy D. Moore, and Laurence G. Yaffe, Effective kinetic theory for high temperature gauge theories, J. High Energy Phys. 01 (2003) 030.

[8] Aleksi Kurkela and Yan Zhu, Isotropization and hydrodynamization in weakly coupled heavy-ion collisions, Phys. Rev. Lett. **115,** 182301 (2015).

[9] Paul Romatschke and Ulrike Romatschke, *Relativistic Fluid Dynamics In and Out of Equilibrium*, Cambridge Monographs on Mathematical Physics (Cambridge University Press, Cambridge, England, 2019).

[10] G. S. Denicol, H. Niemi, E. Molnar, and D. H. Rischke, Derivation of transient relativistic fluid dynamics from the Boltzmann equation, Phys. Rev. D **85,** 114047 (2012); **91,** 039902(E) (2015).

[11] Luciano Rezzolla and Olindo Zanotti, *Relativistic Hydrodynamics* (Oxford University Press, New York, 2013).

[12] Victor E. Ambrus, S. Schlichting, and C. Werthmann, Establishing the range of applicability of hydrodynamics in high-energy collisions, Phys. Rev. Lett. **130,** 152301 (2023).

[13] Z. Citron *et al.*, Report from Working Group 5: Future physics opportunities for high-density QCD at the LHC with heavy-ion and proton beams, CERN Yellow Rep. Monogr. **7,** 1159 (2019).

[14] Andreas Ipp, David I. Müller, and Daniel Schuh, Anisotropic momentum broadening in the 2 + 1D glasma: Analytic weak field approximation and lattice simulations, Phys. Rev. D **102,** 074001 (2020).

[15] Andreas Ipp, David I. Müller, and Daniel Schuh, Jet momentum broadening in the pre-equilibrium glasma, Phys. Lett. B **810,** 135810 (2020).

[16] Margaret E. Carrington, Alina Czajka, and Stanislaw Mrowczynski, Jet quenching in glasma, Phys. Lett. B **834,** 137464 (2022).

[17] Margaret E. Carrington, Alina Czajka, and Stanislaw Mrowczynski, Transport of hard probes through glasma, Phys. Rev. C **105,** 064910 (2022).

[18] Dana Avramescu, Virgil Băran, Vincenzo Greco, Andreas Ipp, David. I. Müller, and Marco Ruggieri, Simulating jets and heavy quarks in the glasma using the colored particle-in-cell method, Phys. Rev. D **107,** 114021 (2023).

[19] Carlota Andres, Liliana Apolinário, Fabio Dominguez, Marcos Gonzalez Martinez, and Carlos A. Salgado, Medium-induced radiation with vacuum propagation in the pre-hydrodynamics phase, J. High Energy Phys. 03 (2023) 189.

[20] Kirill Boguslavski, Aleksi Kurkela, Tuomas Lappi, Florian Lindenbauer, and Jarkko Peuron, Jet momentum broadening during initial stages in heavy-ion collisions, Phys. Lett. B **850,** 138525 (2024).

[21] Sigtryggur Hauksson and Edmond Iancu, Jet polarisation in an anisotropic medium, J. High Energy Phys. 08 (2023) 027.

[22] R. Baier, Yuri L. Dokshitzer, Alfred H. Mueller, and D. Schiff, Medium induced radiative energy loss: Equivalence between the BDMPS and Zakharov formalisms, Nucl. Phys. **B531,** 403 (1998).

[23] R. Baier, Yuri L. Dokshitzer, Alfred H. Mueller, and D. Schiff, Radiative energy loss of high-energy partons traversing an expanding QCD plasma, Phys. Rev. C **58,** 1706 (1998).

[24] B. G. Zakharov, On the energy loss of high-energy quarks in a finite size quark—gluon plasma, JETP Lett. **73,** 49 (2001).

[25] Peter Brockway Arnold, Simple formula for high-energy gluon bremsstrahlung in a finite, expanding medium, Phys. Rev. D **79,** 065025 (2009).

[26] Carlota Andres, Néstor Armesto, Harri Niemi, Risto Paatelainen, and Carlos A. Salgado, Jet quenching as a probe of the initial stages in heavy-ion collisions, Phys. Lett. B **803,** 135318 (2020).

[27] Souvik Priyam Adhya, Carlos A. Salgado, Martin Spousta, and Konrad Tywoniuk, Medium-induced cascade in expanding media, J. High Energy Phys. 07 (2020) 150.

[28] Alexander Huss, Aleksi Kurkela, Aleksas Mazeliauskas, Risto Paatelainen, Wilke van der Schee, and Urs Achim Wiedemann, Discovering partonic rescattering in light nucleus collisions, Phys. Rev. Lett. **126,** 192301 (2021).

[29] Alexander Huss, Aleksi Kurkela, Aleksas Mazeliauskas, Risto Paatelainen, Wilke van der Schee, and Urs Achim Wiedemann, Predicting parton energy loss in small collision systems, Phys. Rev. C **103,** 054903 (2021).

[30] Peter Brockway Arnold and Wei Xiao, High-energy jet quenching in weakly-coupled quark-gluon plasmas, Phys. Rev. D **78,** 125008 (2008).

[31] Simon Caron-Huot, O(g) plasma effects in jet quenching, Phys. Rev. D **79,** 065039 (2009).

[32] P. Aurenche, F. Gelis, and H. Zaraket, A simple sum rule for the thermal gluon spectral function and applications, J. High Energy Phys. 05 (2002) 043.

[33] Juan Martin Maldacena, The large N limit of superconformal field theories and supergravity, Adv. Theor. Math. Phys. **2,** 231 (1998).

[34] Edward Witten, Anti-de Sitter space and holography, Adv. Theor. Math. Phys. **2,** 253 (1998).

[35] Hong Liu, Krishna Rajagopal, and Urs Achim Wiedemann, Calculating the jet quenching parameter from AdS/CFT, Phys. Rev. Lett. **97,** 182301 (2006).

[36] Zi-qiang Zhang, De-fu Hou, and Hai-cang Ren, The finite 't Hooft coupling correction on jet quenching parameter in a $\mathcal{N} = 4$ super Yang-Mills plasma, J. High Energy Phys. 01 (2013) 032.

[37] Amit Kumar, Abhijit Majumder, and Johannes Heinrich Weber, Jet transport coefficient $\hat{q}$ in lattice QCD, Phys. Rev. D **106**, 034505 (2022).

[38] Guy D. Moore, Soeren Schlichting, Niels Schlusser, and Ismail Soudi, Non-perturbative determination of collisional broadening and medium induced radiation in QCD plasmas, J. High Energy Phys. 10 (2021) 059.

[39] Taesoo Song, Ilia Grishmanovskii, and Olga Soloveva, Soft gluon emission from heavy quark scattering in strongly interacting quark-gluon plasma, Phys. Rev. D **107**, 036009 (2023).

[40] Ilia Grishmanovskii, Taesoo Song, Olga Soloveva, Carsten Greiner, and Elena Bratkovskaya, Exploring jet transport coefficients by elastic scattering in the strongly interacting quark-gluon plasma, Phys. Rev. C **106**, 014903 (2022).

[41] Jacopo Ghiglieri, Guy D. Moore, and Derek Teaney, Jet-medium interactions at NLO in a weakly-coupled quark-gluon plasma, J. High Energy Phys. 03 (2016) 095.

[42] Soeren Schlichting and Ismail Soudi, Medium-induced fragmentation and equilibration of highly energetic partons, J. High Energy Phys. 07 (2021) 077.

[43] Y. Mehtar-Tani, S. Schlichting, and I. Soudi, Jet thermalization in QCD kinetic theory, J. High Energy Phys. 05 (2023) 091.

[44] Karen M. Burke et al. (JET Collaboration), Extracting the jet transport coefficient from jet quenching in high-energy heavy-ion collisions, Phys. Rev. C **90**, 014909 (2014).

[45] S. Cao et al. (JETSCAPE Collaboration), Determining the jet transport coefficient $\hat{q}$ from inclusive hadron suppression measurements using Bayesian parameter estimation, Phys. Rev. C **104**, 024905 (2021).

[46] Paul Romatschke and Michael Strickland, Collisional energy loss of a heavy quark in an anisotropic quark-gluon plasma, Phys. Rev. D **71**, 125008 (2005).

[47] Paul Romatschke, Momentum broadening in an anisotropic plasma, Phys. Rev. C **75**, 014901 (2007).

[48] Adrian Dumitru, Yasushi Nara, Bjoern Schenke, and Michael Strickland, Jet broadening in unstable non-Abelian plasmas, Phys. Rev. C **78**, 024909 (2008).

[49] Sigtryggur Hauksson, Sangyong Jeon, and Charles Gale, Momentum broadening of energetic partons in an anisotropic plasma, Phys. Rev. C **105**, 014914 (2022).

[50] Carlota Andres, Fabio Dominguez, Andrey V. Sadofyev, and Carlos A. Salgado, Jet broadening in flowing matter: Resummation, Phys. Rev. D **106**, 074023 (2022).

[51] João Barata, Andrey V. Sadofyev, and Carlos A. Salgado, Jet broadening in dense inhomogeneous matter, Phys. Rev. D **105**, 114010 (2022).

[52] João Barata, Andrey V. Sadofyev, and Xin-Nian Wang, Quantum partonic transport in QCD matter, Phys. Rev. D **107**, L051503 (2023).

[53] João Barata, Xoán Mayo López, Andrey V. Sadofyev, and Carlos A. Salgado, Medium induced gluon spectrum in dense inhomogeneous matter, Phys. Rev. D **108**, 034018 (2023).

[54] Matvey V. Kuzmin, Xoán Mayo López, Jared Reiten, and Andrey V. Sadofyev, Jet quenching in anisotropic flowing matter, Phys. Rev. D **109**, 014036 (2024).

[55] Santosh K. Das, Marco Ruggieri, Surasree Mazumder, Vincenzo Greco, and Jan-e Alam, Heavy quark diffusion in the pre-equilibrium stage of heavy ion collisions, J. Phys. G **42**, 095108 (2015).

[56] Stanislaw Mrowczynski, Heavy quarks in turbulent QCD plasmas, Eur. Phys. J. A **54**, 43 (2018).

[57] Yifeng Sun, Gabriele Coci, Santosh Kumar Das, Salvatore Plumari, Marco Ruggieri, and Vincenzo Greco, Impact of glasma on heavy quark observables in nucleus-nucleus collisions at LHC, Phys. Lett. B **798**, 134933 (2019).

[58] K. Boguslavski, A. Kurkela, T. Lappi, and J. Peuron, Heavy quark diffusion in an overoccupied gluon plasma, J. High Energy Phys. 09 (2020) 077.

[59] Marco Ruggieri, Pooja, Jai Prakash, and Santosh K. Das, Memory effects on energy loss and diffusion of heavy quarks in the quark-gluon plasma, Phys. Rev. D **106**, 034032 (2022).

[60] Kirill Boguslavski, Aleksi Kurkela, Tuomas Lappi, Florian Lindenbauer, and Jarkko Peuron, Heavy quark diffusion coefficient in heavy-ion collisions via kinetic theory, Phys. Rev. D **109**, 014025 (2024).

[61] Aleksi Kurkela and Guy D. Moore, Thermalization in weakly coupled non-Abelian plasmas, J. High Energy Phys. 12 (2011) 044.

[62] Aleksi Kurkela and Guy D. Moore, Bjorken flow, plasma instabilities, and thermalization, J. High Energy Phys. 11 (2011) 120.

[63] J. Berges, K. Boguslavski, S. Schlichting, and R. Venugopalan, Turbulent thermalization process in heavy-ion collisions at ultrarelativistic energies, Phys. Rev. D **89**, 074011 (2014).

[64] Juergen Berges, Kirill Boguslavski, Soeren Schlichting, and Raju Venugopalan, Universal attractor in a highly occupied non-Abelian plasma, Phys. Rev. D **89**, 114007 (2014).

[65] Shanshan Cao, Chathuranga Sirimanna, and Abhijit Majumder, The medium modification of high-virtuality partons, arXiv:2101.03681.

[66] Y. Tachibana et al. (JETSCAPE Collaboration), Hard jet substructure in a multi-stage approach, arXiv:2301.02485.

[67] Alfred H. Mueller, The Boltzmann equation for gluons at early times after a heavy ion collision, Phys. Lett. B **475**, 220 (2000).

[68] Liam Keegan, Aleksi Kurkela, Aleksas Mazeliauskas, and Derek Teaney, Initial conditions for hydrodynamics from weakly coupled pre-equilibrium evolution, J. High Energy Phys. 08 (2016) 171.

[69] Aleksi Kurkela, Aleksas Mazeliauskas, Jean-François Paquet, Sören Schlichting, and Derek Teaney, Effective kinetic description of event-by-event pre-equilibrium dynamics in high-energy heavy-ion collisions, Phys. Rev. C **99**, 034910 (2019).

[70] Aleksi Kurkela, Aleksas Mazeliauskas, and Robin Törnkvist, Collective flow in single-hit QCD kinetic theory, J. High Energy Phys. 11 (2021) 216.

[71] Mark C. Abraao York, Aleksi Kurkela, Egang Lu, and Guy D. Moore, UV cascade in classical Yang-Mills theory via kinetic theory, Phys. Rev. D **89**, 074036 (2014).

[72] Aleksi Kurkela and Aleksas Mazeliauskas, Chemical equilibration in weakly coupled QCD, Phys. Rev. D **99**, 054018 (2019).

[73] Xiaojian Du and Sören Schlichting, Equilibration of weakly coupled QCD plasmas, Phys. Rev. D **104**, 054011 (2021).

[74] Xiaojian Du and Sören Schlichting, Equilibration of the quark-gluon plasma at finite net-baryon density in QCD kinetic theory, Phys. Rev. Lett. **127**, 122301 (2021).

[75] Mikko Laine and Aleksi Vuorinen, *Basics of Thermal Field Theory*, Lecture Notes in Physics Vol. 925 (Springer, Cham, 2016).

[76] Peter Brockway Arnold and Laurence G. Yaffe, Effective theories for real time correlations in hot plasmas, Phys. Rev. D **57**, 1178 (1998).

[77] Yayun He, Tan Luo, Xin-Nian Wang, and Yan Zhu, Linear Boltzmann transport for jet propagation in the quark-gluon plasma: Elastic processes and medium recoil, Phys. Rev. C **91**, 054908 (2015); **97**, 019902(E) (2018).

[78] Aleksi Kurkela and Aleksas Mazeliauskas, Chemical equilibration in hadronic collisions, Phys. Rev. Lett. **122**, 142301 (2019).

[79] Peter Brockway Arnold, Guy D Moore, and Laurence G. Yaffe, Transport coefficients in high temperature gauge theories. 2. Beyond leading log, J. High Energy Phys. 05 (2003) 051.

[80] Stanislaw Mrowczynski, Stream instabilities of the quark—gluon plasma, Phys. Lett. B **214**, 587 (1988); **656**, 273(E) (2007).

[81] Paul Romatschke and Michael Strickland, Collective modes of an anisotropic quark gluon plasma, Phys. Rev. D **68**, 036004 (2003).

[82] Edmond Iancu, Pieter Taels, and Bin Wu, Jet quenching parameter in an expanding QCD plasma, Phys. Lett. B **786**, 288 (2018).

[83] Guang-You Qin and Abhijit Majumder, A pQCD-based description of heavy and light flavor jet quenching, Phys. Rev. Lett. **105**, 262301 (2010).

[84] Jiechen Xu, Alessandro Buzzatti, and Miklos Gyulassy, Azimuthal jet flavor tomography with CUJET2.0 of nuclear collisions at RHIC and LHC, J. High Energy Phys. 08 (2014) 063.

[85] A. Kumar *et al.* (JETSCAPE Collaboration), Inclusive jet and hadron suppression in a multistage approach, Phys. Rev. C **107**, 034911 (2023).

[86] Peter Brockway Arnold and Caglar Dogan, QCD splitting/joining functions at finite temperature in the deep LPM regime, Phys. Rev. D **78**, 065008 (2008).

[87] Florian Lindenbauer, Data and analysis code for arXiv: 2312.00447, 10.5281/zenodo.10419945 (2023).

[88] Pauli Virtanen *et al.*, SciPy 1.0–Fundamental algorithms for scientific computing in Python, Nat. Methods **17**, 261 (2020).

[89] Sigtryggur Hauksson and Charles Gale, Polarized photons from the early stages of relativistic heavy-ion collisions, Phys. Rev. C **109**, 034902 (2024).

[90] Ruizhe Zhao, Luhua Qiu, Yun Guo, and Michael Strickland, Collective modes of a collisional anisotropic quark-gluon plasma, Phys. Rev. D **108**, 034023 (2023).

[91] Michel Le Bellac, *Thermal Field Theory*, Cambridge Monographs on Mathematical Physics (Cambridge University Press, Cambridge, England, 2011).

[92] Jacopo Ghiglieri, Aleksi Kurkela, Michael Strickland, and Aleksi Vuorinen, Perturbative thermal QCD: Formalism and applications, Phys. Rep. **880**, 1 (2020).

[93] Aleksi Kurkela and Florian Lindenbauer, EKTqhat—Effective kinetic theory solver with jet quenching parameter, 10.5281/zenodo.10409474 (2023).